UCRL-17785

cy. 2

University of California

RECEIVED
LAWRENCE
RADIATION LABORATORY
NOV 6 1968
LIBRARY AND
DOCUMENTS SECTION

Ernest O. Lawrence Radiation Laboratory

HARDENING AND RECOVERY OF QUENCHED GOLD

Michael Junichi Yokota

(Ph.D. Thesis)

August 1968

TWO-WEEK LOAN COPY

This is a Library Circulating Copy which may be borrowed for two weeks. For a personal retention copy, call Tech. Info. Division, Ext. 5545

UCRL-17785 cy. 2

DISCLAIMER

This document was prepared as an account of work sponsored by the United States Government. While this document is believed to contain correct information, neither the United States Government nor any agency thereof, nor the Regents of the University of California, nor any of their employees, makes any warranty, express or implied, or assumes any legal responsibility for the accuracy, completeness, or usefulness of any information, apparatus, product, or process disclosed, or represents that its use would not infringe privately owned rights. Reference herein to any specific commercial product, process, or service by its trade name, trademark, manufacturer, or otherwise, does not necessarily constitute or imply its endorsement, recommendation, or favoring by the United States Government or any agency thereof, or the Regents of the University of California. The views and opinions of authors expressed herein do not necessarily state or reflect those of the United States Government or any agency thereof or the Regents of the University of California.

UCRL-17785

UNIVERSITY OF CALIFORNIA

Lawrence Radiation Laboratory
Berkeley, California

AEC Contract No. W-7405-eng-48

HARDENING AND RECOVERY OF QUENCHED GOLD

Michael Junichi Yokota

(Ph.D. Thesis)

August 1968

TABLE OF CONTENTS

ABSTRACT iii
PREFACE vi

PART I

I. INTRODUCTION 1
II. EXPERIMENTAL PROCEDURE 5
A. Specimen Preparation 5
B. Thin Foil Preparation 7
C. Electron Microscope Technique 11
D. Initiation of Slip 11
E. Foil Orientation 11
F. Formation of Stacking Fault Loops in Gold 12
III. RESULTS AND DISCUSSION 17
A. Stacking Fault Tetrahedron-Dislocation Interactions . . 17
B. Stacking Fault Loop-Dislocation Interactions 43
IV. CONCLUSIONS 59
APPENDIX 60
REFERENCES 64

PART II

I. INTRODUCTION 65
II. EXPERIMENTAL PROCEDURE 68
A. Specimen Preparation 68
B. Thin Foil Preparation 68
C. Electron Microscope Technique 69
III. RESULTS AND DISCUSSION 72
A. Annealing of Stacking Fault Tetrahedra 72
B. Annealing of Stacking Fault Loops 95
C. Stacking Fault Tetrahedra Annealing Kinetics 127
IV. CONCLUSIONS 132
APPENDIX 134
REFERENCES 136
RECOMMENDATIONS FOR FUTURE RESEARCH 137
ACKNOWLEDGEMENTS 140

HARDENING AND RECOVERY OF QUENCHED GOLD

Michael Junichi Yokota

Inorganic Materials Research Division, Lawrence Radiation Laboratory,
Department of Mineral Technology, College of Engineering,
University of California, Berkeley, California

ABSTRACT

Direct observations of interactions between stacking fault tetrahedra and loops with moving dislocations in 99.99% purity gold were made by transmission electron microscopy. The wide range of sizes and densities of tetrahedra and loops studied were produced in polycrystalline specimens 75 microns thick by quenching from near the melting point and aging near room temperature.

Direct contact of a moving dislocation with a stacking fault tetrahedron produced one of two reaction products depending on the Burgers vectors and spatial relationship between the quenching defect and the interacting dislocations. In the first case contact interaction resulted in the collapse of the stacking fault tetrahedron and the production of large jogs in the interacting dislocation. In the second case, interaction resulted in the collapse of the stacking fault tetrahedron into a segment of a Frank sessile dislocation loop formed from one of the faces of the stacking fault tetrahedron. Two-thirds of the tetrahedra interactions observed resulted in the products of case one.

Interactions of dislocations with stacking fault tetrahedra without direct contact resulted in the collapse of the stacking fault tetrahedra into triangular Frank sessile dislocation loops.

Direct contact of a moving dislocation with a stacking fault loop

PREFACE

This study is divided into two parts. In Part I, the processes responsible for quench-hardening of gold containing stacking fault tetrahedra and loops are investigated. The several mechanisms proposed follow from direct transmission electron microscope observations of the interaction of dislocations with these defects.

In Part II, the processes responsible for the recovery of quenched-hardened gold are studied. From direct electron microscope observations of the annealing of stacking fault tetrahedra and loops, the recovery mechanisms by which these defects anneal out in thin foils of gold are determined. An expression is derived for the kinetics of the annealing process based on the proposed mechanisms.

PART I

I. INTRODUCTION

The dislocation substructure produced in quenched and aged gold has been shown by Hirsch and Silcox (1959) to consist of tetrahedra of stacking faults on {111} planes with $\frac{1}{6}$ ⟨110⟩ type stair-rod dislocations along the edges of the tetrahedra. These stacking fault tetrahedra are expected to interact with glissile dislocations and to present obstacles to their movement. Their effectiveness in hindering movement of dislocations has been found to be considerable by Meshii and Kaufmann (1959) who have observed as much as a six-fold increase in the yield stress for polycrystalline wire specimens. The exact nature of dislocation-stacking fault tetrahedron interaction including the reasons for the apparently high stresses needed to move dislocations in the presence of tetrahedra, can be studied by transmission electron microscopy.

The single previous example of a direct observation of an interaction between a moving dislocation and a stacking fault tetrahedron in gold was made by Hirsch and Silcox (1959). Their study was only of an exploratory nature however and no detailed picture of the interaction was given. In an analysis of the interactions to be expected there are many different kinds possible, depending on the Burgers vectors and spatial relationships between the interacting dislocations and the stacking fault tetrahedra. Kimura and Maddin (1965) have recently considered this problem and have proposed several possible mechanisms of dislocation-stacking fault tetrahedron contact interaction. From geometrical considerations however, their mechanisms should apply for only two among an almost infinite number of cases. In the majority of cases, the interacting

can then provide further direct evidence for the above mechanisms.

The subject of the present study is concerned with the phenomenon of quench-hardening in gold. This hardening is thought to result from the interaction of dislocations with the defects (i.e. stacking faults tetrahedra and loops) produced by the quenching and aging treatment. The purpose of this investigation is to give direct experimental evidence through transmission electron microscopy of these interactions. This evidence will then be used to present theoretical models for the interaction processes.

II. EXPERIMENTAL PROCEDURE

A. Specimen Preparation

Polycrystalline gold specimens suitable for quenching were prepared from 75 micron thick sheet material obtained from Cominco Products Inc. of Spokane, Washington. The manufacturer produced this sheet material from one-half inch thick slabs of chemical reduction refined 99.999% purity gold by cold rolling at room temperature approximately twenty times without any intermediate annealing. The impurity content as given by the manufacturer is listed in Table I. Specimens 25 mm long and 7 mm wide were prepared from this material and annealed in alumina boats at 900°C and 1000°C for 24 and 48 hours in air and then allowed to cool slowly within the furnace. The resulting specimens had a ⟨001⟩ preferred orientation which is convenient because it allows easy differentiation between triangular Frank sessile loops and stacking fault tetrahedra. Triangular Frank sessile dislocation loops appear in this projection as triangles, while stacking fault tetrahedra appear as squares.

The specimens were next placed in quartz specimen holders and suspended in a vertical tube furnace open to the atmosphere. Specimens were quenched from a temperature of 1000°C. Quenching was performed by releasing the weighted specimen holder into an ice-water bath fixed a few centimeters below the specimen. The specimens were then aged for 1, 2, 3, and 4 hours at one of the following temperatures: 0, 50, 100 or 150°C ± 2°C. The time spent in transferring the specimen from the quenching bath to the aging bath was kept constant at 30 seconds. Both silicon oil and water were used as heat transfer mediums for the aging

Table I

Impurities	ppm
Platinum	2.0
Lead	1.0
Silver	0.5
Copper	0.3
Silicon	0.2
Iron	0.1
Magnesium	0.1

bath. After completion of the aging treatment, the specimens were stored in absolute ethyl alcohol at 0°C. The different sizes and densities of tetrahedra that could be obtained by varying the aging temperature are shown in Fig. 1.

B. Thin Foil Preparation

Thin foil samples suitable for observation under the electron microscope were prepared by electropolishing utilizing a modification of the standard window technique. The specimens were mounted in noncorrosive holders so as to minimize plastic deformation of the specimens due to handling during the electrothinning step. A controlled rate of flow of the polishing solution past the two faces of the specimen was achieved by the use of a pair of parallel plate stainless steel cathodes of adjustable width and a magnetic stirrer. The temperature of the cell was controlled by a constant temperature bath. The experimental set up used is schematically illustrated in Fig. 2.

A two step electrothinning procedure was used. The compositions of the two polishing solutions as well as the temperatures and current densities used are listed in Table II. The more reactive hydrochloric acid-solution was used to thin the specimens down to approximately a micron while the less reactive, more controllable chromic-oxide acetic acid solution was used to produce the final thin foils. At no time during the entire thinning process was the specimen subjected to temperatures higher than room temperature. Near the final stages of the thinning process the current was switched on and off repeatedly. This caused small flakes to separate at the edges of the specimen which were then recovered from the solution, rinsed and stored in ethyl alcohol at 0°C.

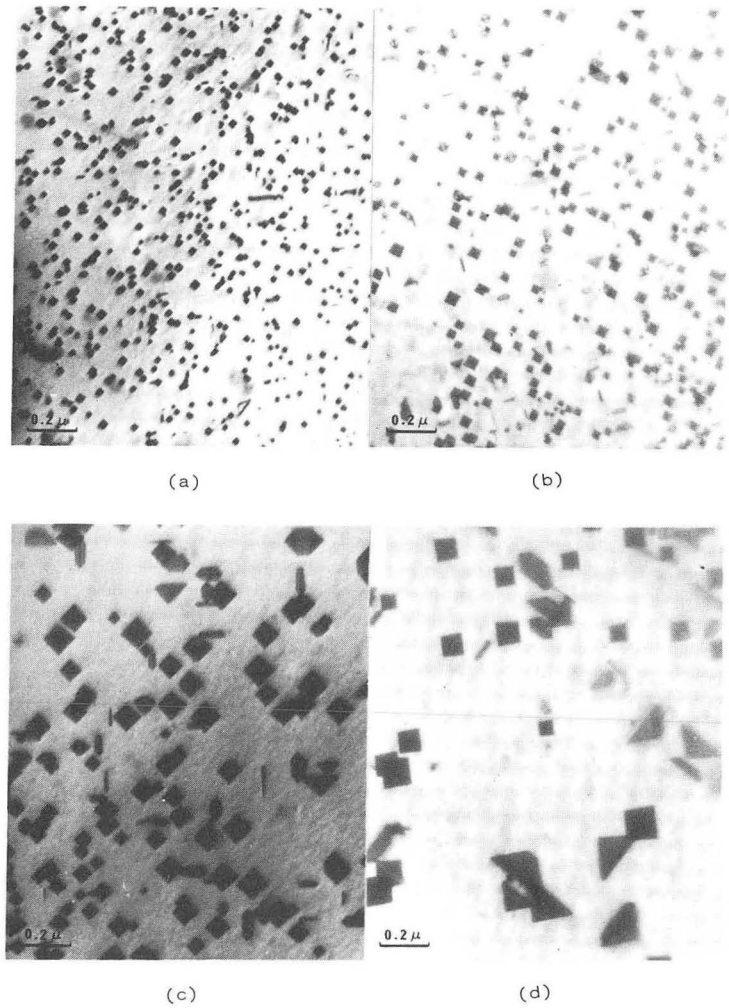

IM 2329

Fig. 1 Stacking fault tetrahedra size distributions and densities obtained for several aging conditions a) 0°C; b) 50°C; c) 100°C; d) 150°C for two hours

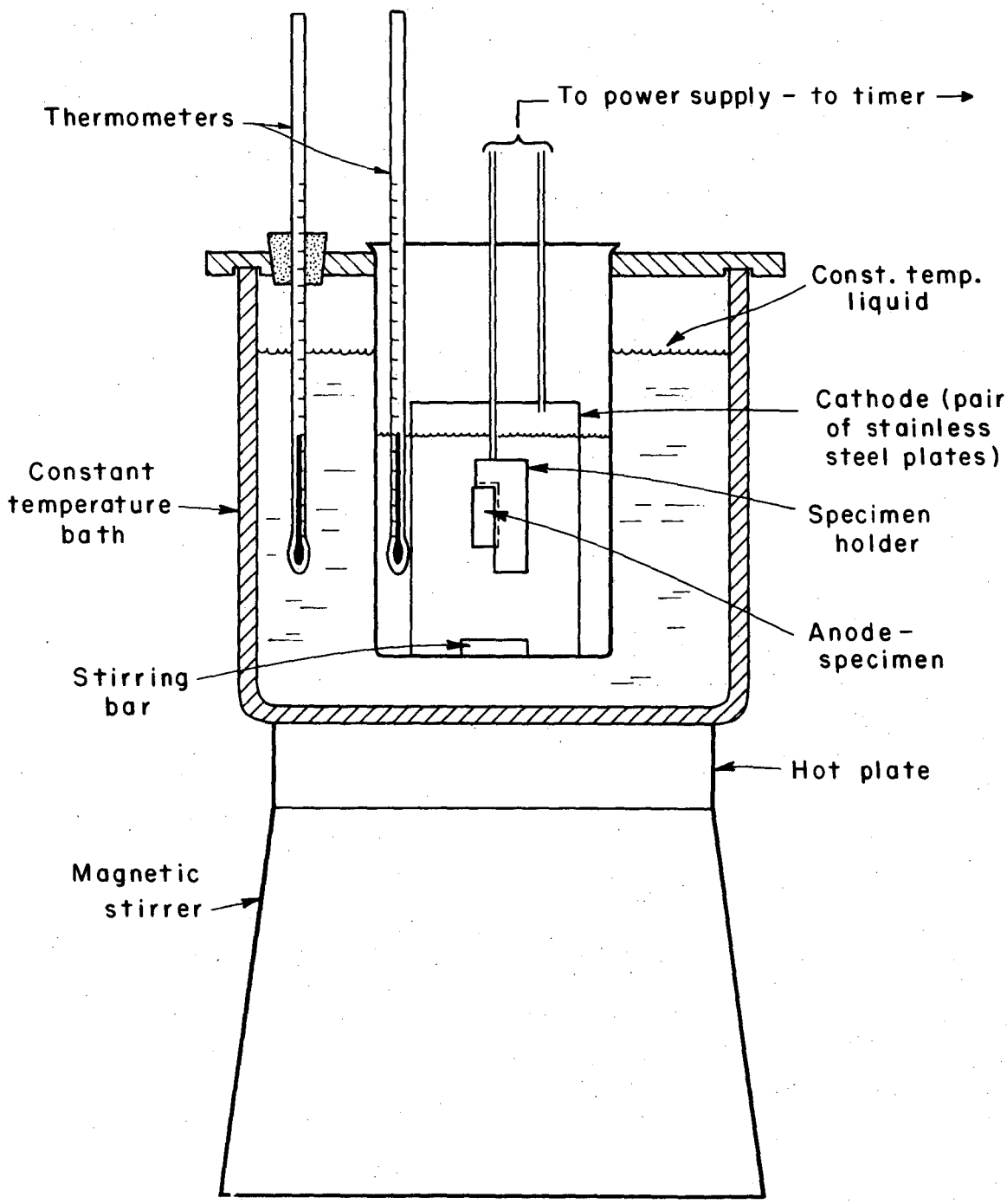

XBL678-5172

Fig. 2 Electropolishing set up

Table II

<u>Electrolytic Solution No. 1</u>	
Hydrochloric acid - HCl (37.5%)	200 cc
Ethyl alcohol - $C_2H_5(OH)$ (200 p)	175 cc
Glycerin - $C_3H_5(OH)_3$ (95.0%)	125 cc
Temperature: -30°C	
Current Density: 0.7 cm/cm^2	
<u>Electrolytic Solution No. 2</u>	
Glacial Acetic Acid - CH_3COOH (99.8%)	465 cc
Chromium Trioxide CrO_3	87.5 gms
Water H_2O	25 cc
Temperature: 10°C	
Current Density 0.25 cmpa/cm^2	

C. Electron Microscope Technique

A Siemens 1 electron microscope operated at 100 kV with a beam current less than 20 μamp was used to make all of the microscope observations. Tilting experiments were facilitated by the use of a Valdré-type double tilting stage. Observations were made at a working magnification of 20,000× and recorded on Kodak Projector Slide Plates.

D. Initiation of Slip

In order to initiate slip in the thin foil samples while under observation in the electron microscope, the foils were first firmly attached to copper microscope grids with a solution of polybutene. The specimen-grid assembly was then slightly heated by the electron beam producing differential expansion of the copper-gold assembly. The resulting stresses developed are believed to be responsible in large part for the movement of the great numbers of dislocations produced during observation..

The dislocations were found to originate either at the edges of the foils or at tilt or grain boundaries. From the curvature of the dislocation images between pinning points the stresses needed to move the dislocations were estimated to be about G/1000 where G is the elastic shear modulus.

E. Foil Orientation

As mentioned earlier, polycrystalline sheet specimens having a ⟨001⟩ preferred orientation were found to be very suitable for the needs of the present experiment. The ⟨001⟩ orientation allows easy identification of both the triangular Frank sessile loop and the stacking fault tetrahedron

as shown in Fig. 3. In this orientation the triangular Frank sessile dislocation loop appears as a triangle (A) while the complete stacking fault tetrahedron appears as a square (B). A stacking fault tetrahedron which is cut by the surface of the foil appears as an elongated hexagon (C). Where possible, orientations slightly off the ⟨001⟩ orientation were chosen to facilitate the determination of the orientations and Burgers vectors of the stacking fault tetrahedron and loop, and the interacting dislocation. This is accomplished by tilting off the exact ⟨001⟩ orientation a few degrees along one of the {002} Kikuchi pairs. Figures 4 and 5 illustrate how the stacking fault tetrahedron and loop and the dislocation slip traces appear in such an orientation. In order to determine exactly the Burgers vector of the moving dislocation, a cross slip trace of the moving dislocation needed to be observed before or after the interaction.

F. Formation of Stacking Fault Loops in Gold

Mori and Meshii (1965) found that the size distribution and density of stacking fault tetrahedra in quenched and aged gold were very sensitive to the preaging and aging times and temperatures. They found that the higher aging temperature conditions produced the larger average sizes and lower densities of stacking fault tetrahedra. In the present investigations this trend was also observed. Figures 1a, b, c, and d are micrographs of representative areas showing the stacking fault tetrahedra size distributions and densities obtained for several aging conditions. Note that for the 150°C aging condition that a good percentage of the stacking fault tetrahedra have collapsed to form stacking fault loops.

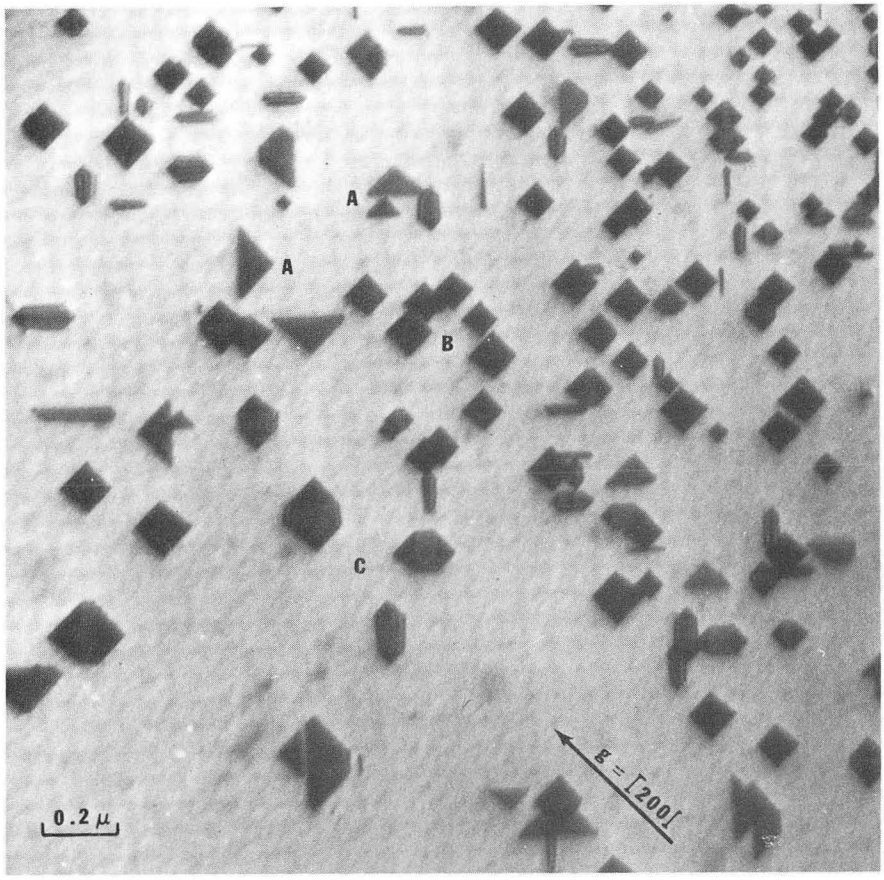

IM 2328

Fig. 3 Stacking fault tetrahedra and Frank sessile dislocation loops as they appear in the ⟨001⟩ orientation: A-triangular Frank sessile loops; B-complete stacking fault tetrahedra; C-stacking fault tetrahedra truncated by the foil surface.

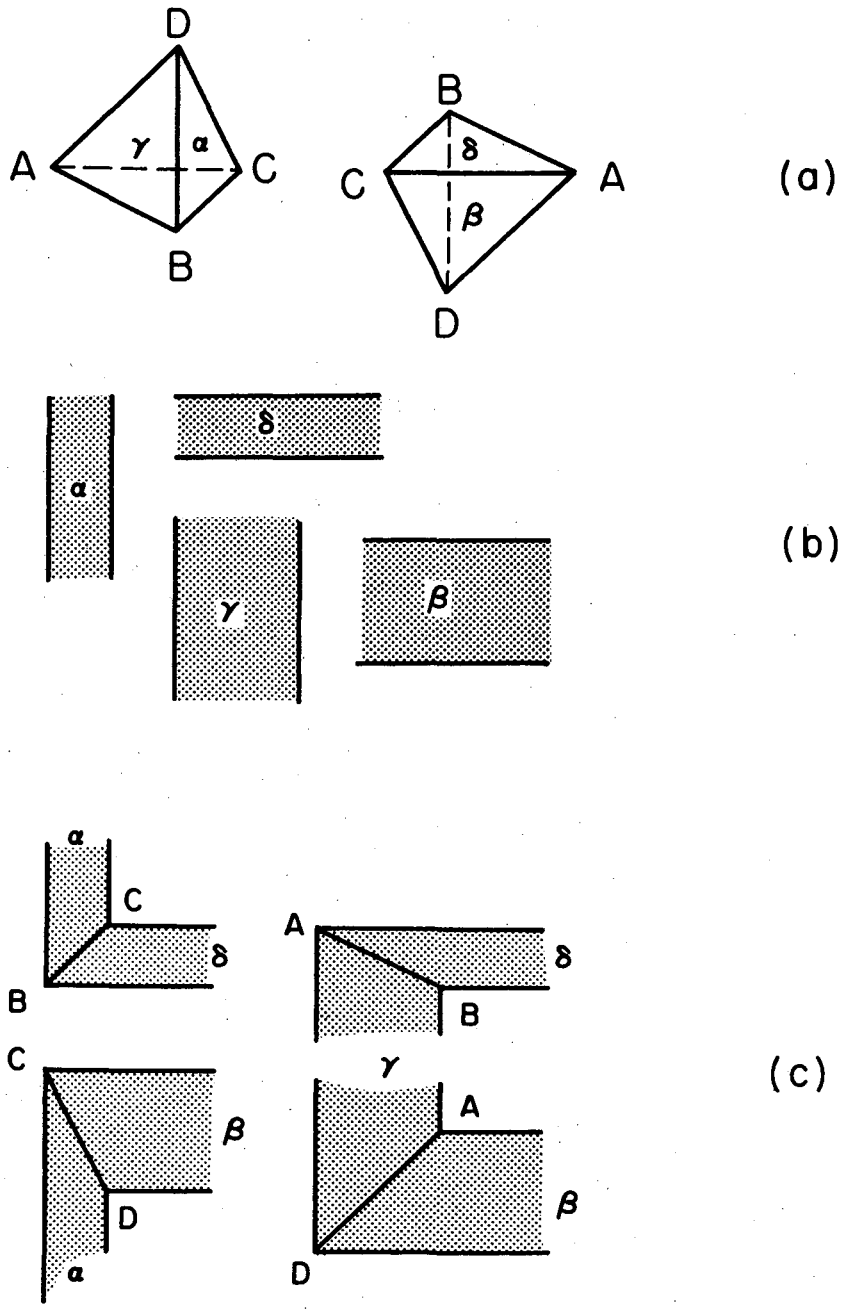

MUB-12141

Fig. 4a The two possible orientations of stacking fault tetrahedra as they appear in nearly ⟨001⟩ orientation.

4b Widths of slip traces for the α, β, γ, and δ planes as they appear in nearly ⟨001⟩ orientation.

4c Cross-slip traces for the dislocations of Burgers vectors BC, CD, BA and AD as they appear in nearly ⟨001⟩ orientation.

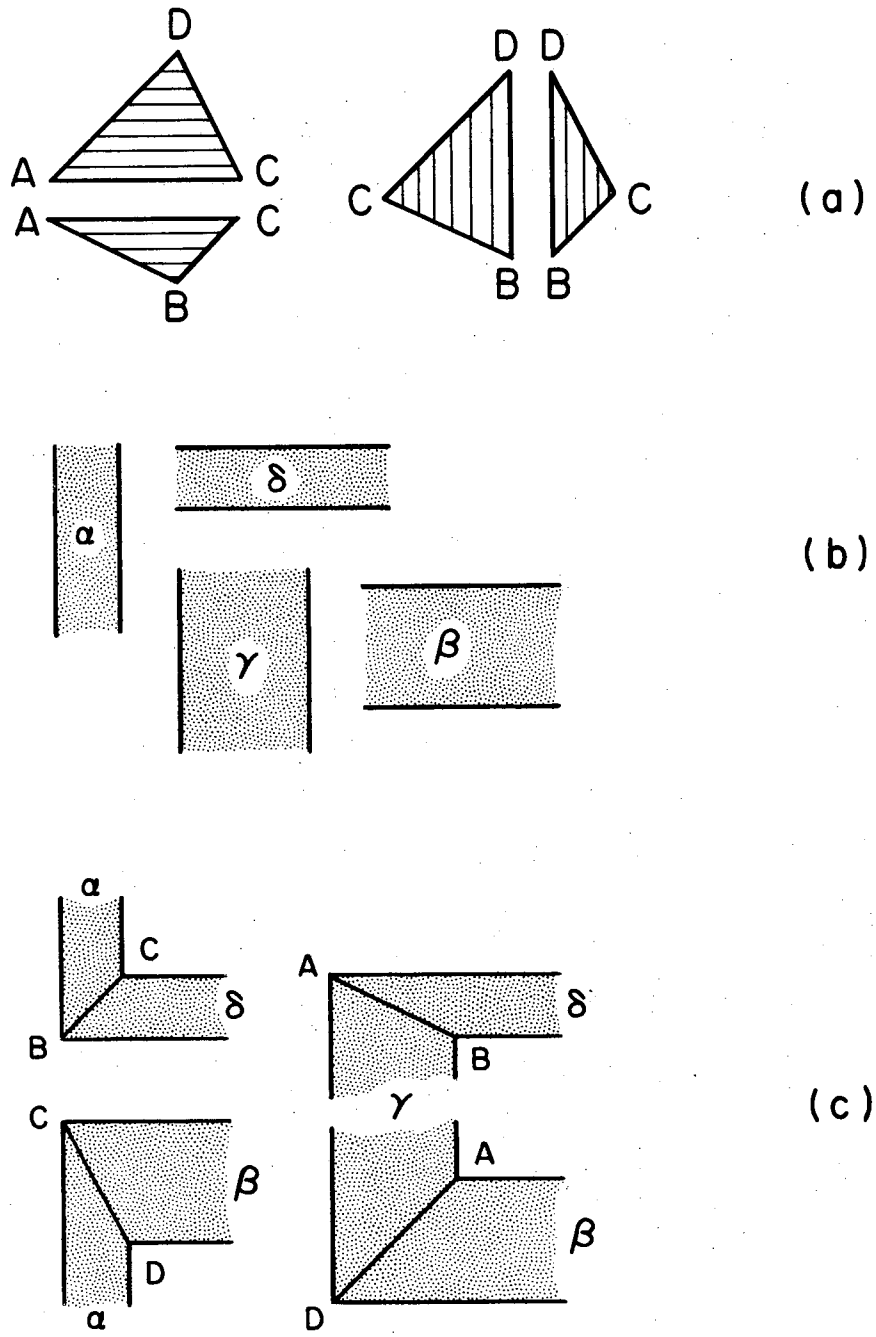

MUB-12803

Fig. 5a The four possible orientations of the stacking fault loops as they appear in nearly ⟨001⟩ orientation

5b Widths of slip traces for the α, β, γ, and δ planes as they appear in nearly ⟨001⟩ orientation.

5c Cross slip traces for the dislocations of Burgers vector BC, CD, BA, and AD, as they appear in nearly ⟨001⟩ orientation

The collapse of stacking fault tetrahedra to triangular Frank sessile dislocation loops has been recently confirmed in a study by Washburn and Yokota (1967) in which they performed annealing experiments both inside and outside the microscope on thin foils of quenched and aged gold.

III. RESULTS AND DISCUSSION

A. Stacking Fault Tetrahedron-Dislocation Interactions

1. Interpretation of the Observed Interactions

a. Experimental Parameters. A number of parameters must be considered in the analysis of the dislocation-stacking fault tetrahedron interaction. Figure 6 illustrates the geometrical situation where the top and front views of a stacking fault tetrahedron, lying on one of its faces, are presented. Consider the primary slip plane to be parallel to the face ABC of the stacking fault tetrahedron. Thomson's notation will be used to designate the Burgers vectors of the various dislocations.

From Fig. 6 we can see that the approach of the interacting dislocation toward the stacking fault tetrahedron can vary over a range of 120 degrees. It should also be noted that in all but two cases where the approaching dislocation is parallel to AB and BC, the interacting dislocation would first contact the stair rod DB and not the faces of the stacking fault tetrahedron ADB or BDC.

Second, the glissile dislocation can have any of the three possible Burgers vectors AB, BC, and CA. Note that dislocations having Burgers vectors AB and BC can cross slip in the planes associated with the stair rod $\gamma\alpha$ along DB while dislocations having the third Burgers vector CA cannot. The significance of the preceding statement will become clear when the two cases of stacking fault tetrahedron-dislocation contact interaction are discussed in Section 2.

A third important factor is the size of the stacking fault tetrahedron, ℓ, especially with regard to its stability in relation to the

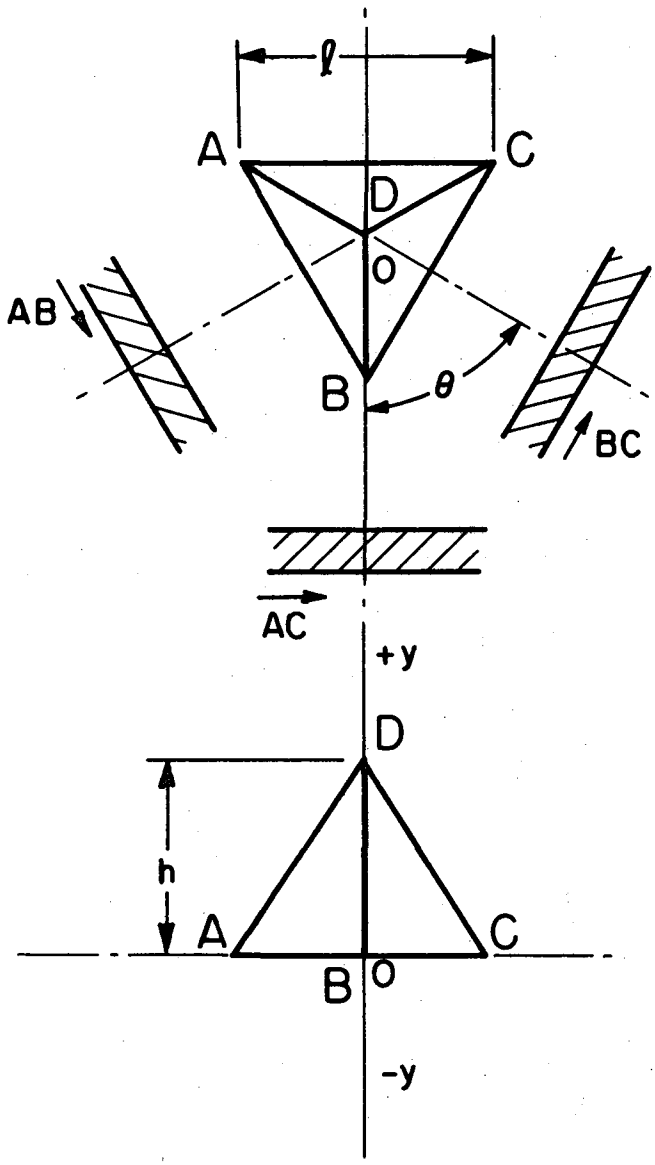

MUB-12142

Fig. 6 Top and front views of stacking fault tetrahedron showing geometrical relationships between stacking fault tetrahedron and the parameters: θ - angle of approach of the glissile dislocation toward stacking fault tetrahedron; $b_1 b_2$ and b_3 - Burgers vectors of the glissile dislocation; y - location of the slip plane of the glissile dislocation from face of stacking fault tetrahedron that is parallel to it.

other possible vacancy defects (i.e., Frank sessile dislocation loop, perfect prismatic dislocation loop).

A fourth factor results from the fact that the primary slip plane of the moving dislocation can intersect the stacking fault tetrahedron anywhere along a distance $\sqrt{2}/3\ell$. This parameter is introduced in Fig. 6 as y with the origin at the base of the stacking fault tetrahedron.

The speed of the interacting dislocation is a fifth factor which may be important.

And finally, the temperature must be included as a sixth parameter in that it affects the exponential factor included in the various expressions for the activation energy for reaction.

b. Experimental Approach. Because of the nature of the experimental technique and of the phenomenon being studied only several of the parameters listed in the preceding section can by systematically studied in any way. The temperature for example can be controlled in the microscope to about ±20°C. The size of the stacking fault tetrahedron can be varied by a factor of 10 through use of varying aging temperatures. Third, the spatial relationship of the Burgers vectors between the glissile dislocation and the stacking fault tetrahedron can be determined by selecting suitable roeintations of the foil and/or by a number of tilting experiments. The speed of approach of the interacting dislocation and the exact geometry of interaction between the glissile dislocation and the stacking fault tetrahedron however cannot be easily controlled and therefore studied.

In all, approximately 100 interactions between glissile dislocations and stacking fault tetrahedra were observed. Edge lengths of stacking fault tetrahedra observed to interact with glissile dislocations varied from 150Å to 1500Å; in this size range a tetrahedron can lower its energy by transforming to a triangular Frank loop. For those interactions observed, only one parameter, the geometrical relationship of the Burgers vector of the interacting dislocation and the stair rod of the stacking fault tetrahedron appeared to influence the results of the dislocation reaction. This observation will be elaborated further in Sec. III.2, together with the proposed mechanisms of interactions.

c. General Features of Slip Traces. The analysis of dislocation-stacking fault tetrahedron interactions by transmission electron microscopy is made possible by the fact that moving dislocations in gold leave behind contrast effects marking the path taken by the dislocation in its slip plane. Figure 7 illustrates the two types of slip trace contrast effects that have been consistently observed. Immediately after passage of a dislocation and lasting several minutes the entire projection of the slip plane either becomes darker or lighter than the background with the greatest contrast exhibited near the intersection of the glide surface with the top and bottom surfaces of the foil. As can be seen in Fig. 7 both types of contrast effects can be produced in different parts of the same slip trace by reversal of g. Here g is reversed as a result of a bend contour. These contrast effects are thought to result from a layer of surface contamination which prevents the slip step caused by the moving dislocation from reaching as a whole and immediately the surface of the foil (Hirsch et al. 1965). What results then is in

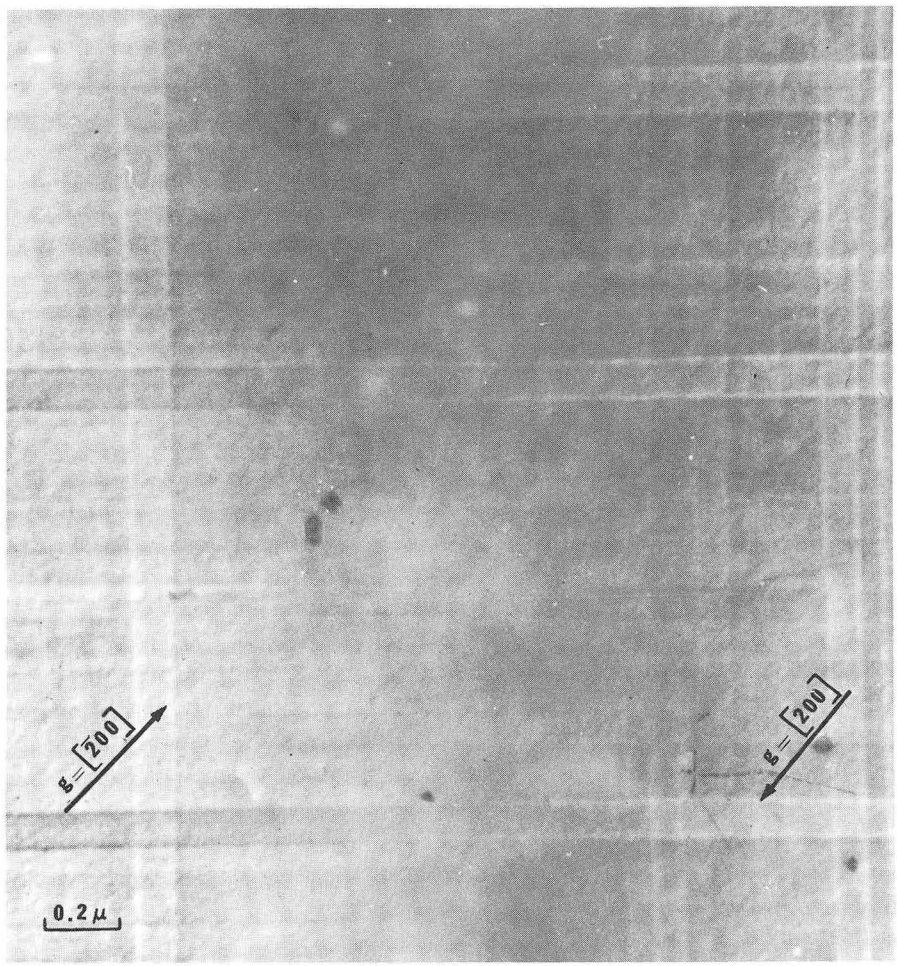

IM 2252

Fig. 7 Micrograph in ⟨001⟩ orientation showing slip traces crossing a bend contour where the operating reflection vector g changes sign resulting in reversal of contrast of the slip traces.

effect a long dislocation dipole of mainly edge orientation which is left behind the moving dislocation front. Contrast effects expected from such a dipole agree with that observed in slip traces.

d. Types of Interactions Expected Between a Stacking Fault Tetrahedron and the Moving Dislocation. The interaction between a stacking fault tetrahedron and a moving dislocation can take place in a number of ways. The first type of interaction can occur through direct contact of the tetrahedron with the interacting dislocation. In Section 2, four mechanisms result in two types of reaction products.

The second type of interaction can occur without direct contact of the tetrahedron with the moving dislocation. In this type of interaction the stress field of the moving dislocation aids in the nucleation of one or more Shockley partial dislocations in a part of the stacking fault tetrahedron which then interacts with the rest of the stacking fault tetrahedron. In Sec. 3, the three mechanisms of stress induced collapse of stacking fault tetrahedra to Frank sessile dislocation loops are described. After collapse of the stacking fault tetrahedron, further reaction can occur between the triangular Frank loop and the intersecting dislocation.

Three other types of interactions are possible but were not observed. They are:

i. cross-slipping of dislocations around the stacking fault tetrahedra,

ii. bowing out of dislocations around the stacking fault tetrahedra leaving dislocation loops around the tetrahedra, and

iii. cutting of the stacking fault tetrahedra by the moving dislocations leaving ledges in two faces of the tetrahedra.

2. Contact Interaction Between a Moving Dislocation and a Stacking Fault Tetrahedron

Direct contact interaction of a moving dislocation with a stacking fault tetrahedron results in one of two reaction products depending on the Burgers vectors and spatial relationships between the tetrahedron and the moving dislocation. In the first case contact interaction results in the collapse of the stacking fault tetrahedron and the formation of a pair of jogs on the interacting dislocation. In the second case, the interaction results in the collapse of the stacking fault tetrahedron. These two results can be seen in Figs. 8 and 9 where two dislocations of the same Burgers vector have interacted with two stacking fault tetrahedra having orientations rotated 180° from each other. Figures 10 and 11 are more examples illustrating the two types of reactions observed.

Each of the reaction products, the jogs in the interacting dislocation and the Frank sessile loop, can be formed by two different mechanisms depending on whether the moving dislocation first contacts a face or an edge (i.e., stair rod) of the stacking fault tetrahedron. These mechanisms are discussed with the aid of Figs. 12 through 15.

a. Face Interaction. Figure 12 illustrates the sequence of dislocation reactions that probably occurs when the moving dislocation first contacts a face of the stacking fault tetrahedron that lies in the cross slip plane of the moving dislocation.

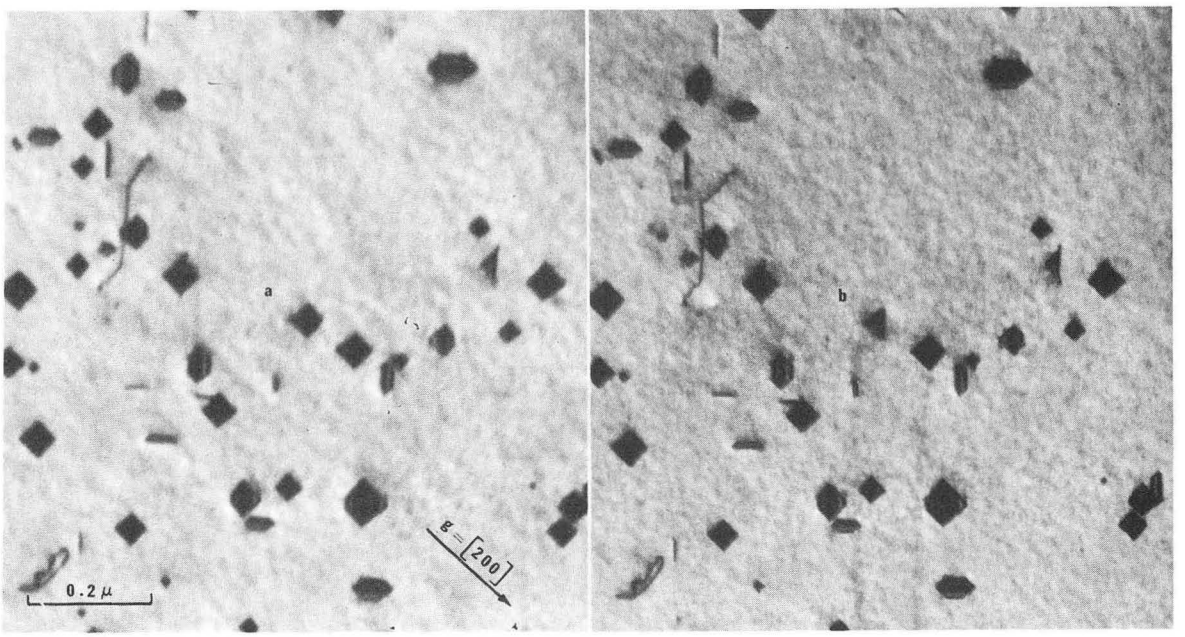

(a) (b)

IM 2334

Fig. 8a-b Interaction between a moving dislocation and a stacking fault tetrahedra resulting in the formation of a Frank sessile dislocation loop.

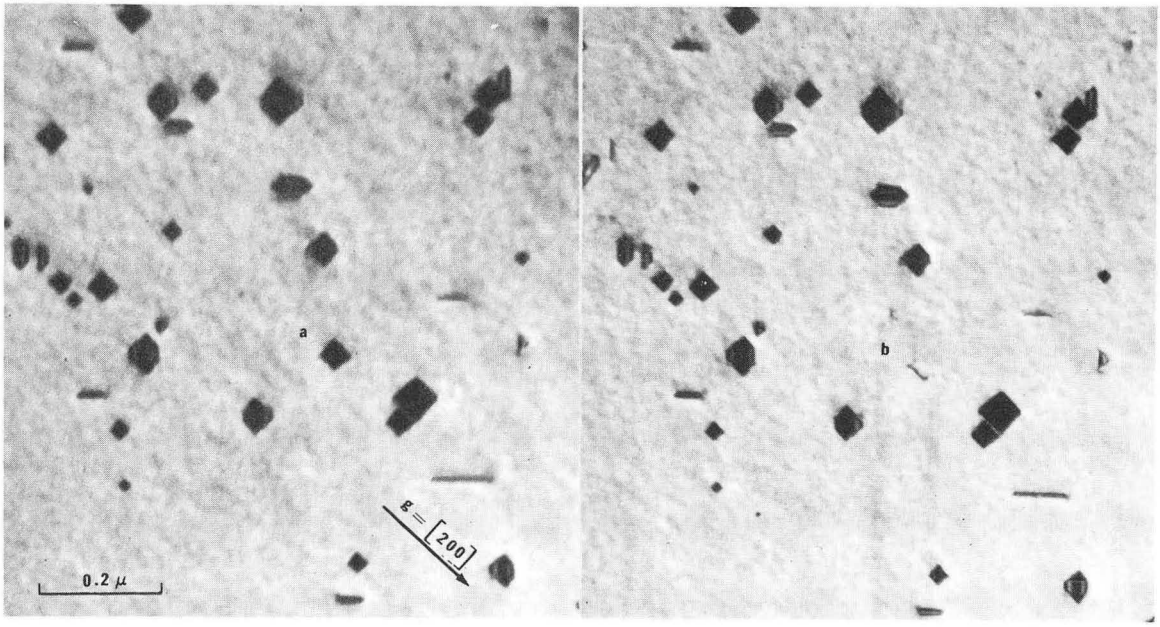

(a) (b) IM 2333

Fig. 9a,b Interactions between moving dislocations and stacking fault tetrahedra resulting in the collapse of the tetrahedra and the formation of jogs in the interacting dislocations.

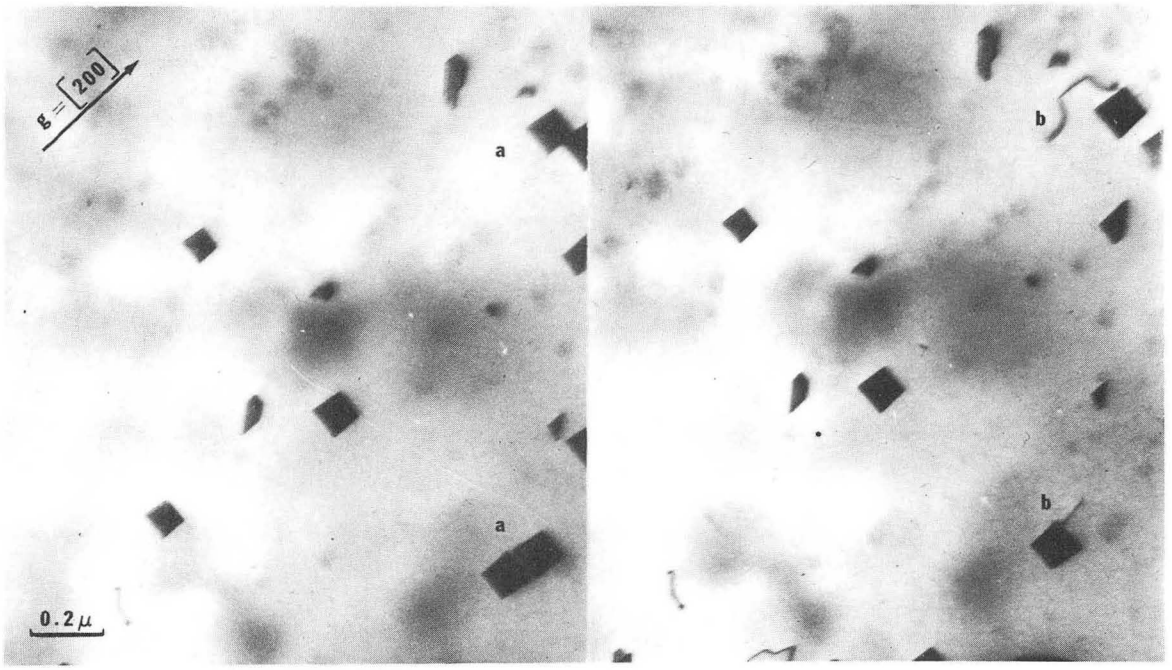

(a) (b)

IM 2335

Fig. 10a,b Interaction between a moving dislocation and a stacking fault tetrahedron resulting in the collapse of the stacking fault tetrahedron and the formation of jogs in the interacting dislocation.

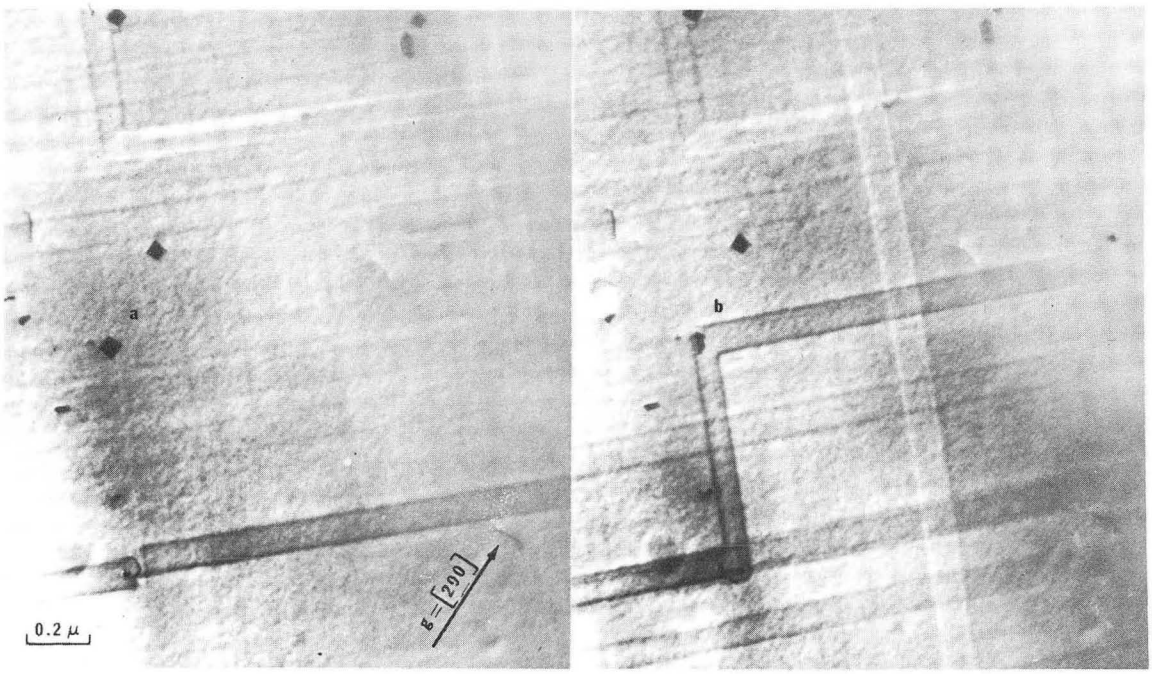

(a) (b)

IM 2332

Fig. 11a,b Interaction between a moving dislocation and a stacking fault tetrahedron resulting in the formation of a Frank sessile dislocation loop.

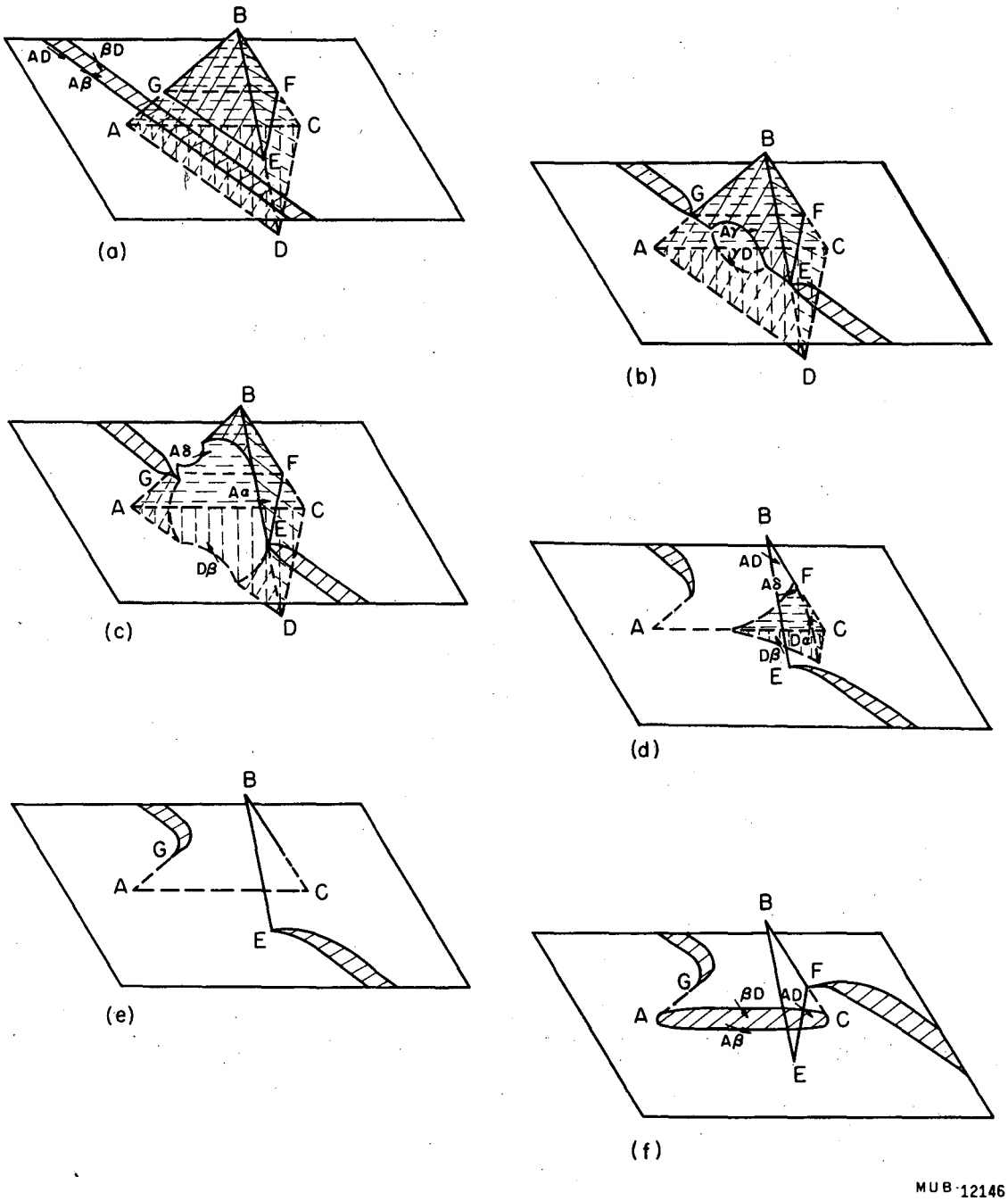

Fig. 12 a-f The sequence of dislocation reactions that take place when the moving dislocation first contacts a face of the stacking fault tetrahedron that lies in the cross-slip plane of the moving dislocation.

i. The moving dislocation first must constrict from the extended form $A\beta + \beta D$ in the plane of the stacking fault (Fig. 12b)

$$A\beta + \beta D = AD \tag{1}$$

ii. The constricted segment of the interacting dislocation can then dissociate into two Shockley partial dislocations $A\gamma$ and γD. Two constriction points are needed.

$$AD = A\gamma + \gamma D \tag{2}$$

iii. The stacking fault is swept away by the glide of the Shockley partials in the face ABD. The Shockley partials next react with the stair rods to form Shockley partials on the faces ABC and DAC (Fig. 12c).

$$A\gamma + \gamma\delta = A\delta \tag{3}$$

$$D\gamma + \gamma\beta = D\beta, \text{ etc.} \tag{4}$$

iv. The Shockley partials on adjacent faces of the tetrahedron interact with the common stair rod to form a perfect dislocation of the Burgers vector AD (Fig. 12d).

$$A\delta + \delta\beta + \beta D = AD, \text{ etc.} \tag{5}$$

v. The final result is one turn of a helical dislocation (Fig. 12e) or a jogged dislocation and a perfect prismatic dislocation loop (Fig. 12f) if the right side of the interacting dislocation continues in its slip plane.

If the moving dislocation first contacts a face of the stacking fault tetrahedron that does not lie in the cross slip plane of the moving dislocation, a part of a triangular Frank sessile dislocation loop is left instead. Figure 13 illustrates the sequence of the dislocation reactions that might occur when this case is realized.

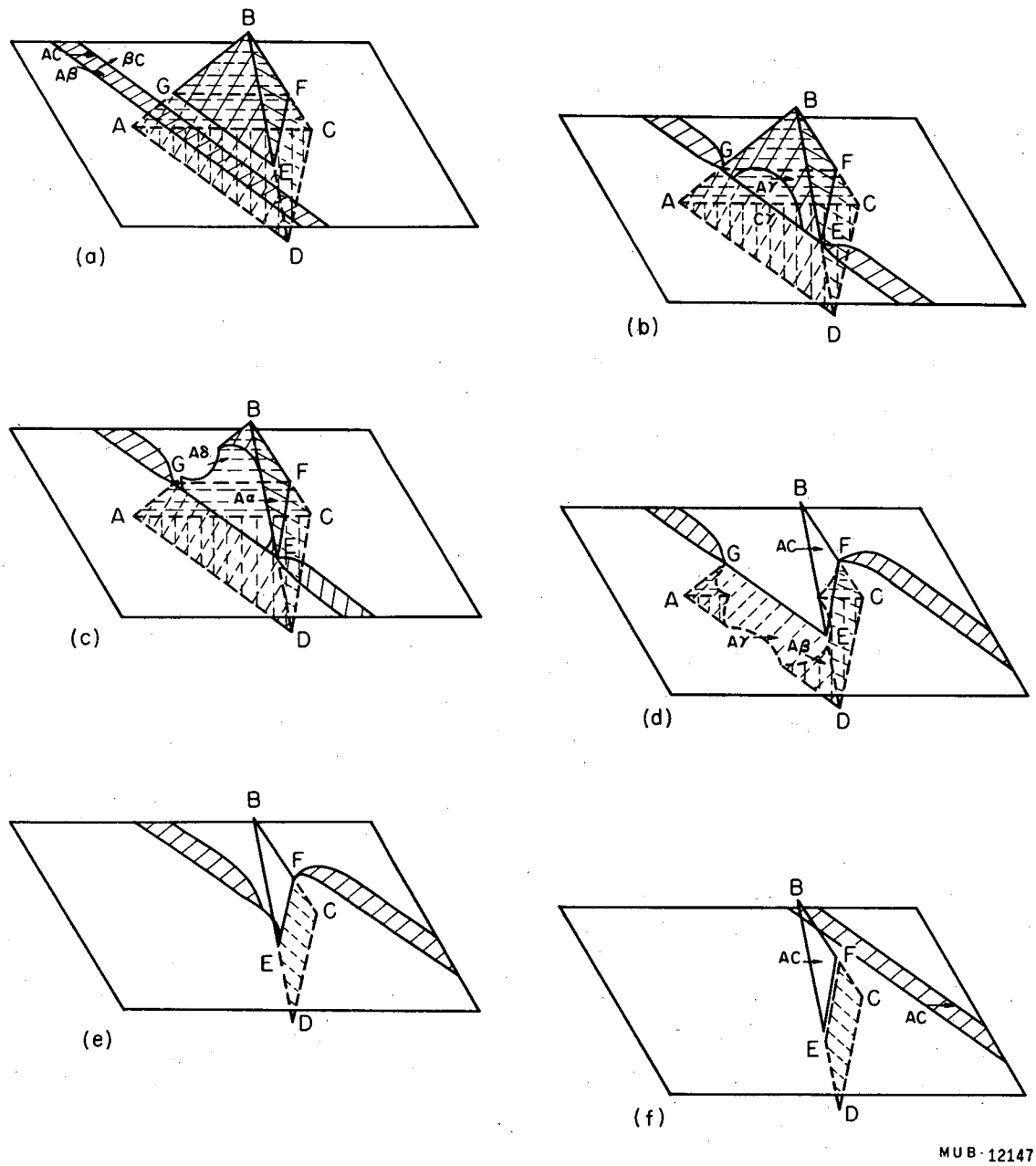

Fig. 13 a-f The sequence of dislocation reactions that take place when the moving dislocation first contacts a face of the stacking fault tetrahedron that does not lie in the cross-slip plane of the moving dislocation.

i. The moving dislocation must first constrict from the extended form $A\beta + \beta C$ in the face ABD of the stacking fault tetrahedron (Fig. 13 b).

$$A\beta + \beta C = AC \tag{6}$$

ii. The constricted segment of the interacting dislocation can then dissociate into Frank sessile and Shockley partial dislocations $C\gamma$ and $A\gamma$ respectively (Fig. 13b). Two constriction points are needed

$$AC = A\gamma + \gamma C \tag{7}$$

iii. The Shockley partial, $A\gamma$, reacts with the stair rods $\gamma\delta$ and $\gamma\alpha$ to form Shockley and Frank sessile partials in the faces ABC and DBC respectively (Fig. 13c)

$$A\gamma + \gamma\delta = A\delta \tag{8}$$

$$A\gamma + \gamma\alpha = A\alpha \tag{9}$$

iv. The Shockley partial, $A\delta$, next reacts with the stair rod $\delta\beta$ to form the Shockley partial $A\beta$ in the face ACD and with the stair rod $\delta\alpha$ to form the Frank partial $A\alpha$. The interacting dislocation AC reacts with $A\alpha$ to form the prismatic loop AC and the Frank sessile loop $A\alpha$.

The above reactions can be viewed as a two-step process which occurs first by the collapse of the tetrahedron into a Frank sessile loop and second by the interaction of the glissile dislocation with part of the Frank loop to form the perfect prismatic loop. From a purely geometrical argument, 1/3 of the interactions should result in the jogged dislocation while 2/3 of them should result in the Frank sessile loop.

However, of the 100 interactions observed, approximately 2/3 resulted in jogged dislocations and 1/3 in the Frank sessile loop.

b. Edge Interactions. Figure 14 illustrates the sequence of dislocation reactions that occurs when the moving dislocation first contacts a stair rod dislocation of the stacking fault tetrahedron that lies in the cross slip plane of the moving dislocation.

i. The interacting dislocation as in the two preceding cases must again constrict from the extended form $A\beta + \beta D$ but only at a single point at the edge of the tetrahedron

$$A\beta + \beta D = AD \tag{10}$$

ii. The constricted segment, AD, can then dissociate into the Shockley partials $A\gamma$ and γD in face DAB and into the Frank sessile and Shockley partials, $A\alpha$ and αD respectively in face DBC.

$$AD = A\gamma + \gamma D \tag{11}$$

$$AD = A\alpha + \alpha D \tag{12}$$

iii. The reaction then follows a course similar to that of the previously described mechanism. The end result is again a jogged dislocation and a triangular perfect prismatic loop which usually escapes to the surface of the foil.

The second reaction product, the Frank sessile dislocation loop results if the moving dislocation first contacts a stair rod of the stacking fault tetrahedron that does not lie in the cross slip plane of the moving dislocation. Figure 15 illustrates the sequence of dislocation reactions that occurs when this situation is realized.

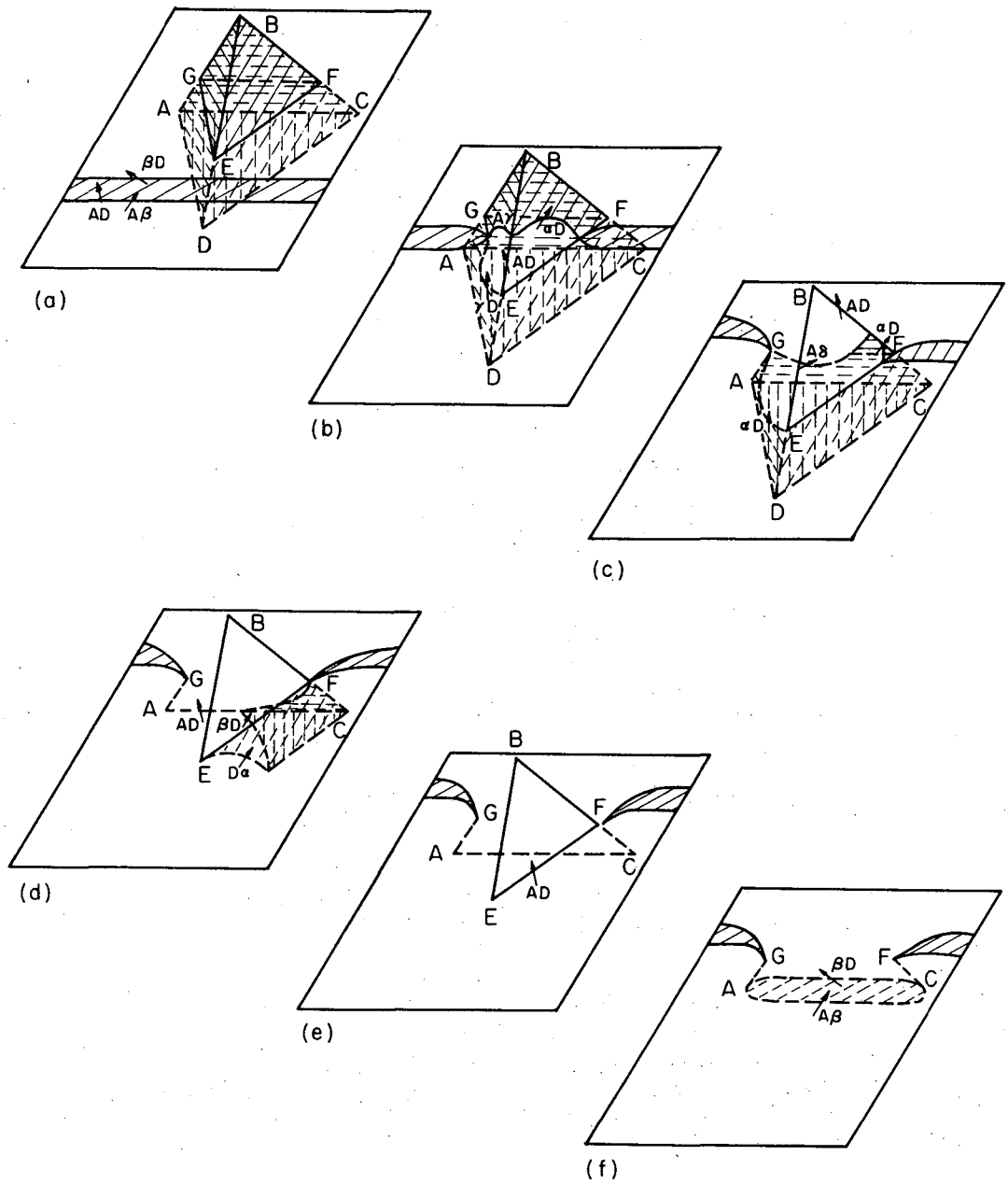

MUB-12144

Fig. 14 a-f The sequence of dislocation reactions that take place when the moving dislocation first contacts a stair rod dislocation of the stacking fault tetrahedron that lies in the cross-slip plane of the moving dislocation.

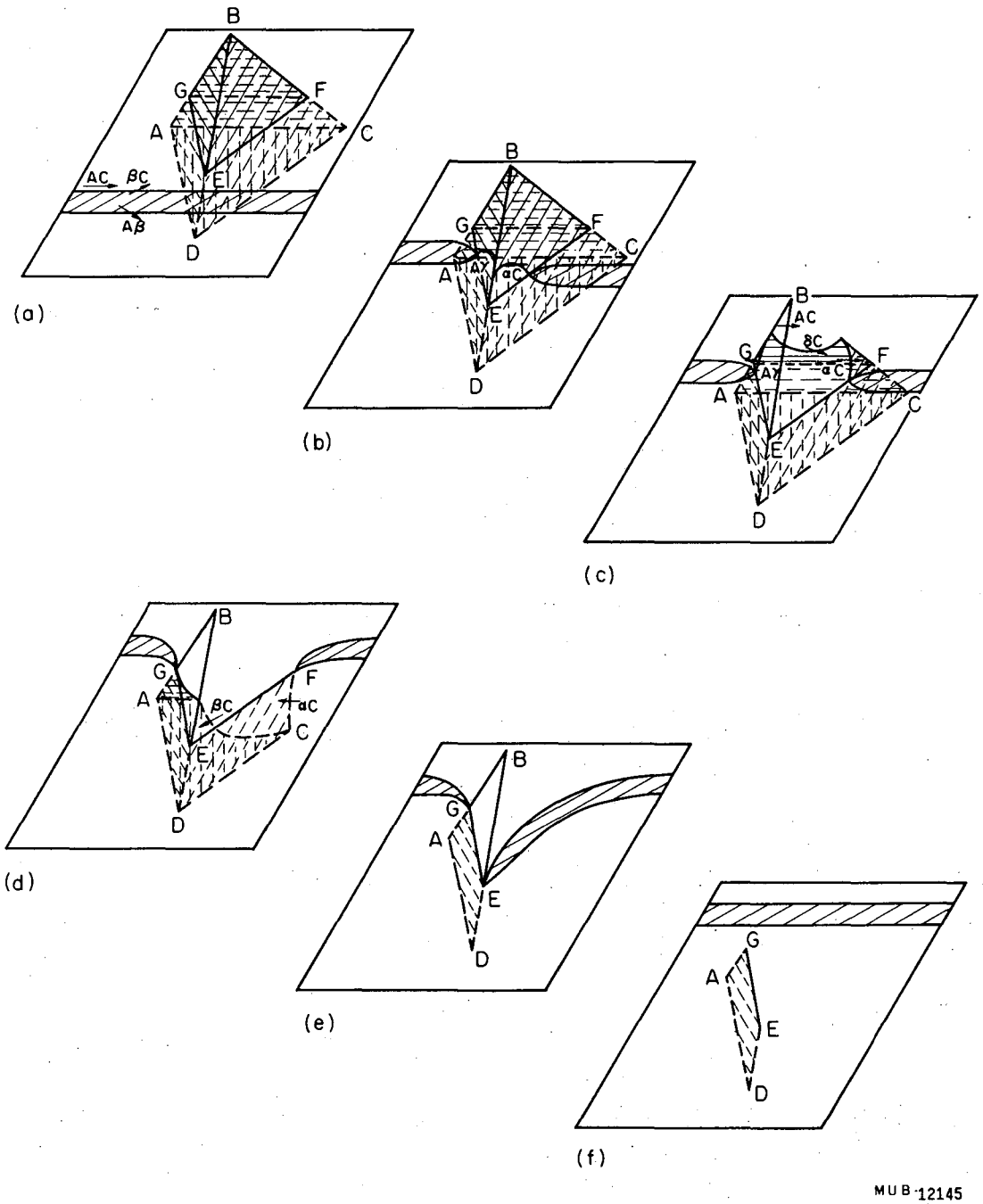

Fig. 15 a-f The sequence of dislocation reactions that take place when the moving dislocation first contacts a stair rod dislocation of the stacking fault tetrahedron that does not lie in the cross-slip plane of the moving dislocation.

i. As in the preceding case a constriction point is required at the point of contact between the interacting dislocation and a stair rod of the tetrahedron.

ii. The constricted point can extend into segments of Shockley and Frank sessile partials in faces DAB and DBC.

$$AC = A\gamma + \gamma C \quad \text{face DAB} \tag{13}$$

$$AC = A\alpha + \alpha D \quad \text{face DBC} \tag{14}$$

iii. The reaction then follows as previously described producing the Frank sessile and perfect prismatic loops.

In the above two cases, 2/3 of the reactions should result in jogged dislocations and 1/3 result in Frank sessile dislocation loops. This is in agreement with the experimental observations. If we assume that the radius of curvature of the moving dislocations is large compared to ℓ, the edge length of the stacking fault tetrahedra, it then becomes evident that the moving dislocation-stair rod interaction should be expected to happen much more frequently than the moving dislocation-face interaction. The observed proportion of the two types of reaction products tends to confirm this expectation.

If the glissile dislocation and the stair rod dislocation of the stacking fault tetrahedron are to interact as in the proposed mechanism, the following dislocation reactions are necessary:

a) $AD = A\gamma + \gamma D$

(Perfect) = (Shockley) + (Shockley)

b) $AD = A\alpha + \alpha D$

(Perfect) = (Frank) + (Shockley)

c) $A\gamma + \gamma A + \alpha D = AD$

(Shockley) + (Stair rod) + (Shockley) = (Perfect)

Using the simple Burgers vector squared (b^2) energy criterion for reaction each of the above reactions should take place.

The entire interaction, except for the initial constriction step, occurs concurrently with the release of energy. The hardening observed by Meshii and Kaufmann (1959) can be explained as due to the barrier of the constriction step and/or due to the superjogs created on the dislocations as a result of interaction. In the latter case hardening results because the dislocations are effectively pinned by the edge superjogs. In the former case the interacting dislocations are held up against the tetrahedron until a combination of a thermal-stress fluctuation occurs which is sufficient to overcome the barrier of the constriction step. Figure 16 shows glissile dislocations held up by stacking fault tetrahedra indicating the barrier energy to be considerable. From the curvature of the held up dislocations the stress on the dislocations is on the order of $2\times10^{-3}G$. This stress level is comparable to the flow stress of $10^{-3}G$ obtained by Meshii and Kaufmann for wire samples of gold containing stacking fault tetrahedra.

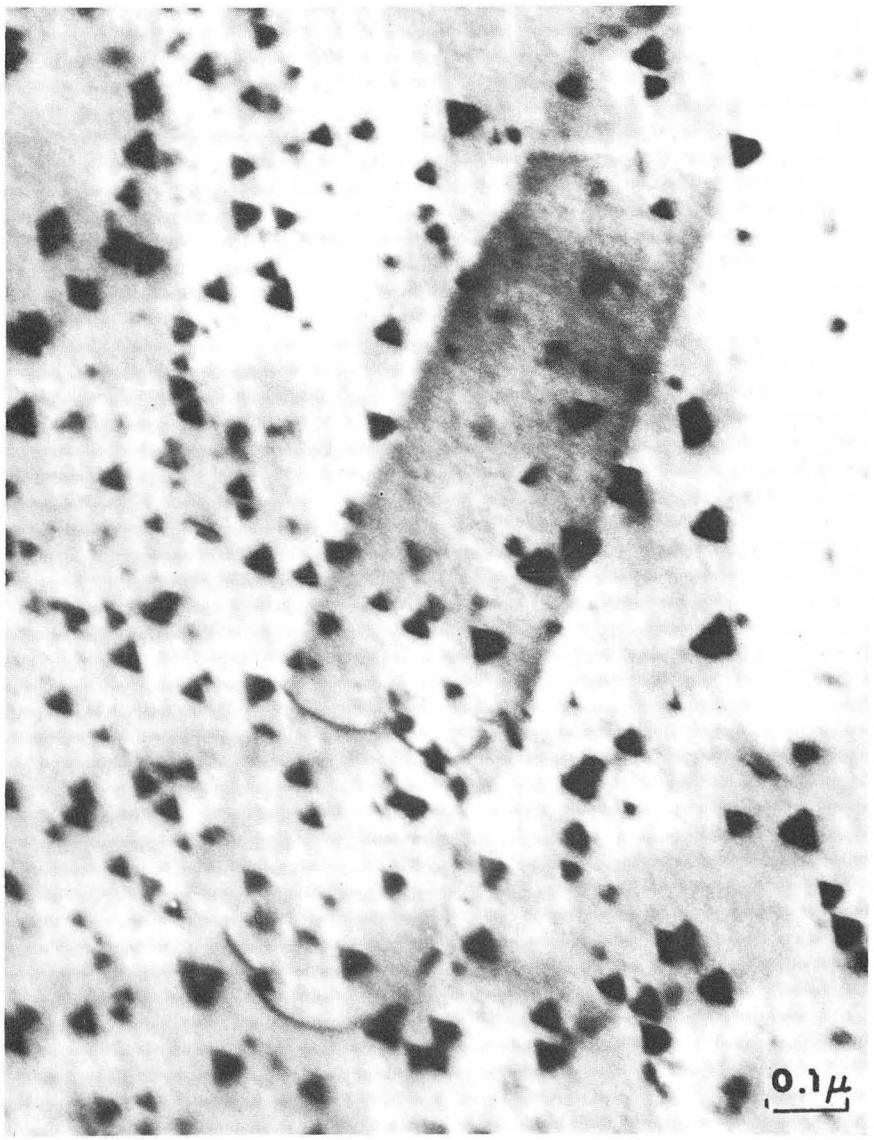

XBB 686-3942

Fig. 16 Several dislocations being held up by stacking fault tetrahedra.

Figure 11 represents an unusual case. This reaction is an example of the type where the Burgers vector of the interacting dislocation does not lie in either of the two planes containing the stair rod of the stacking fault tetrahedron which is first intersected. The unusual shape of the resulting Frank sessile dislocation loop as well as the slip trace can be explained in the following way. Figure 17 illustrates the sequence of reactions that could have produced these results. In Fig. 17b the interacting dislocation first contacts the stacking fault tetrahedron at point E. In Fig. 17c the interacting extended dislocation has constricted and Shockley partial dislocations begin to sweep out the stacking faults in planes DBC and DAB. In Fig. 17d, the interacting dislocation cross slips into a plane parallel to ABC and produces the Frank sessile dislocation loop ABEHI.

3. Interactions without Direct Contact Between Stacking Fault Tetrahedra and Moving Dislocations

Besides the direct contact interactions discussed in the preceding section, moving dislocations can interact with stacking fault tetrahedra by aiding in their collapse to Frank sessile dislocation loops. Figure 18 gives an example of this type of interaction. The foil orientation is again [001] in which a complete stacking fault tetrahedron appears as a square and a Frank sessile dislocation loop appears as a triangle. Figure 18a shows a few dislocations that have stopped just before reaching the stacking fault tetrahedron (A). Figure 18b taken several seconds later shows that the stacking fault tetrahedron has collapsed to a Frank sessile dislocation loop (B). The collapse of a stacking fault tetrahedron to a Frank sessile loop requires the nucleation of one or more Shockley

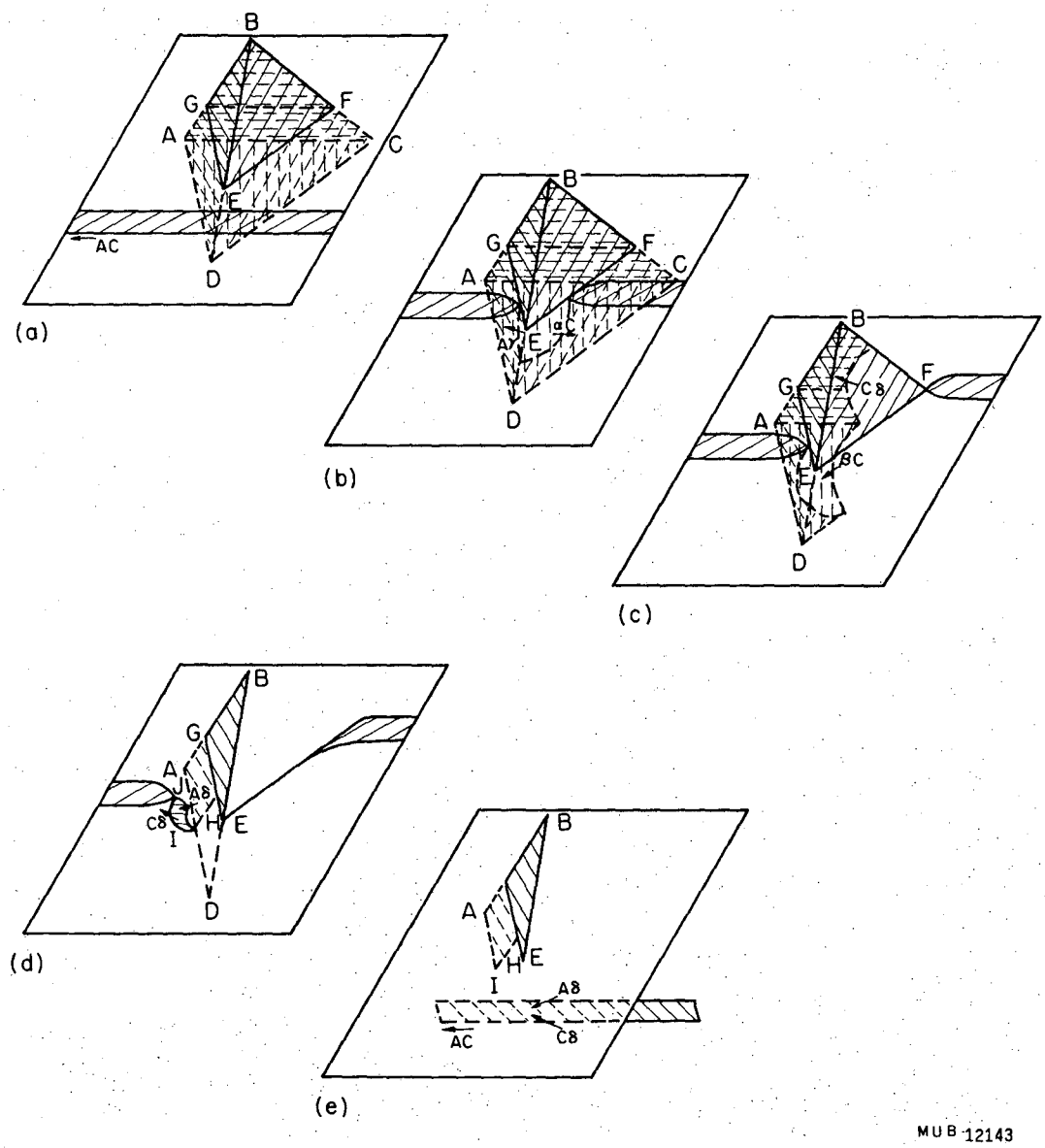

Fig. 17 The sequence of dislocation reactions thought to take place in the reaction of Fig. 8.

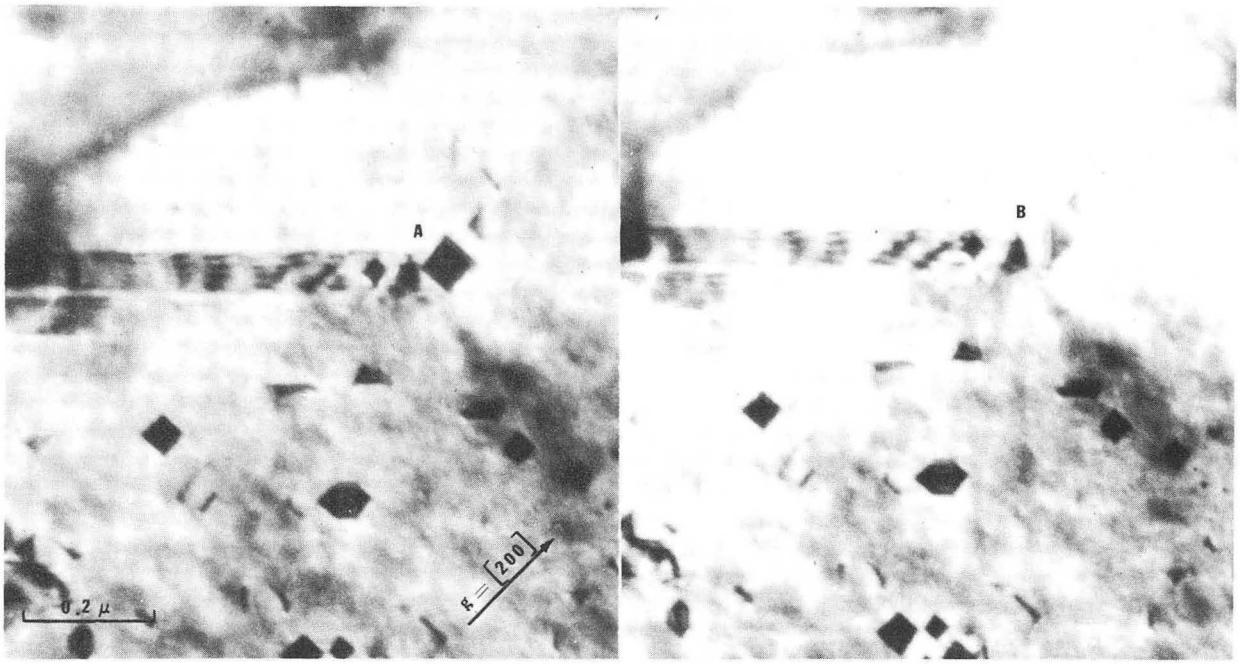

(a) (b)

IM 2330

Fig. 18a Dislocations being held up by a stacking fault tetrahedron.

Fig. b The subsequent collapse of the tetrahedron, several seconds later to a Frank sessile loop.

partial dislocations. Figure 19 shows the reactions that could have occurred to produce the results of Fig. 18.

Three cases can be distinguished by which the nucleation might occur. In the first case, the stress field of the moving dislocation aids in the nucleation of a Shockley partial dislocation loop in one of the four faces of the stacking fault tetrahedron. The nucleated Shockley partial dislocation reacts with the stair rods, sweeping out the stacking faults on two other faces resulting in the collapse of the stacking fault tetrahedron to a triangular Frank sessile dislocation loop. In the second case, the dislocation stress field aids in the nucleation of two Shockley partials in the edge of the stacking fault tetrahedron, and in the third case three Shockley partial dislocations nucleate at the corner.

From the above experimental observations direct contact as well as the non-contact interaction of dislocations with stacking fault tetrahedra have been shown to occur. The particular mechanism which may be dominant and rate controlling however is dependent on the particular set of experimental conditions. High temperatures, slow moving extended dislocations and large stacking fault tetrahedra favor the dominance of the non-contact collapse mechanisms. The interaction for this case follows a two stage process where first the stress field of the dislocation collapses the stacking fault tetrahedra to a Frank sessile dislocation loop and then the dislocation interacts with the loop.

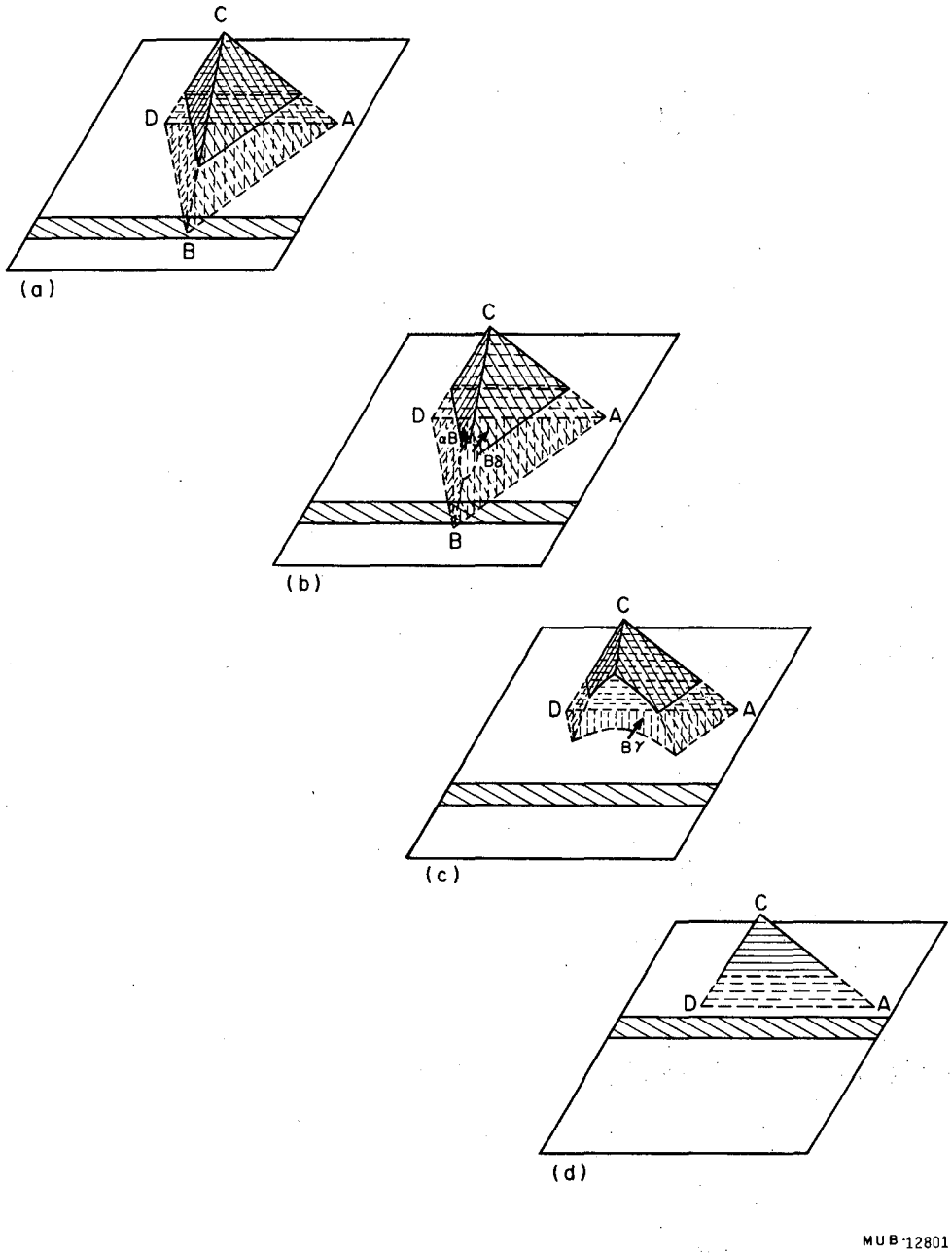

Fig. 19 A sequence of dislocation reactions which can be used to explain the collapse of the stacking fault tetrahedron

B. Stacking Fault Loop-Dislocation Interactions

In the description of the dislocation-stacking fault loop interactions to follow, Thompson's (1955) notation will be used to represent the Burgers vectors of the interacting dislocations and the stacking fault loops as well as their glide and habit planes. In the schematic drawings the interacting dislocation will have the Burgers vector AB. The primary and cross slip planes will be ABC and ABD, respectively. The essential features of the interactions are unchanged if the stacking fault loops are viewed as unextended rather than extended. For this reason and those of simplification the loops are represented as unextended in the following drawings.

A number of geometrical parameters must be considered in the analysis of the glissile dislocation stacking fault loop interaction. [See Saada and Washburn (1963).] Figure 20 illustrates the essential geometrical features of the problem where an oblique view of the four possible orientations of the stacking fault loops are presented. With the help of this figure three separate cases for glissile dislocation interaction with stacking fault loops can be distinguished.

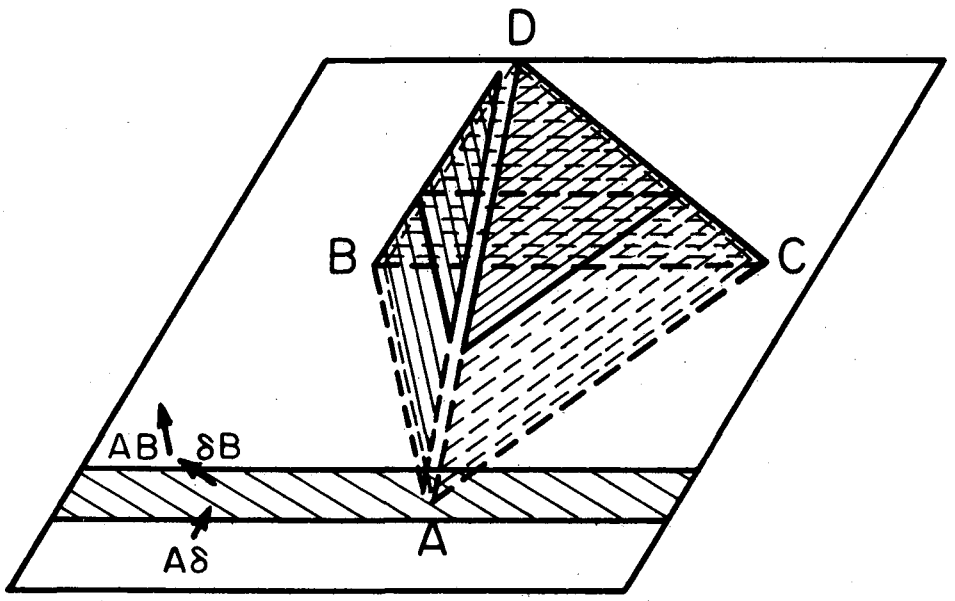

MUB 12962

Fig. 20 Oblique view of the four possible orientations of the stacking fault loops.

1. Interactions in which the Loop does not Lie in Either of the Slip Planes of the Interacting Dislocation.

Case 1 occurs when the interacting dislocation of Burgers vector AB intersects either the stacking fault loop ADC or DCB, both of which do not lie in either of the slip planes of the interacting dislocation. Figure 21 illustrates the sequence of dislocation reactions that can occur when this situation is realized.

a. The moving dislocation first must constrict from the extended form $A\delta + \delta B$ to AB at the first point of contact (Fig. 21b)

$$A\delta + \delta B = AB \tag{1}$$

b. The constricted segment of the interacting dislocation can then dissociate in the stacking fault of the loop into Frank sessile and Shockley partial dislocations $A\beta$ and βB respectively (Fig. 21c)

$$AB = A\beta + \beta B \tag{2}$$

c. The stacking fault is swept away by the glide of theShockley partial dislocation, $A\beta$, and the interacting dislocation acquires a segment that does not lie on the primary glide plane. A segment of the original stacking fault is left unreacted (Fig. 21d)

$$A\beta + \beta B = AB \tag{3}$$

d. Points E and F of the interacting dislocation can join to form the perfect prismatic dislocation loop EDF (Fig. 21e) which can then glide to the surface of the foil leaving the stacking fault loop AEFC and the unjogged glissile dislocation, AB (Fig. 21f).

The above series of reactions can be used to explain the results of the dislocation-stacking fault loop interactions which have occurred in

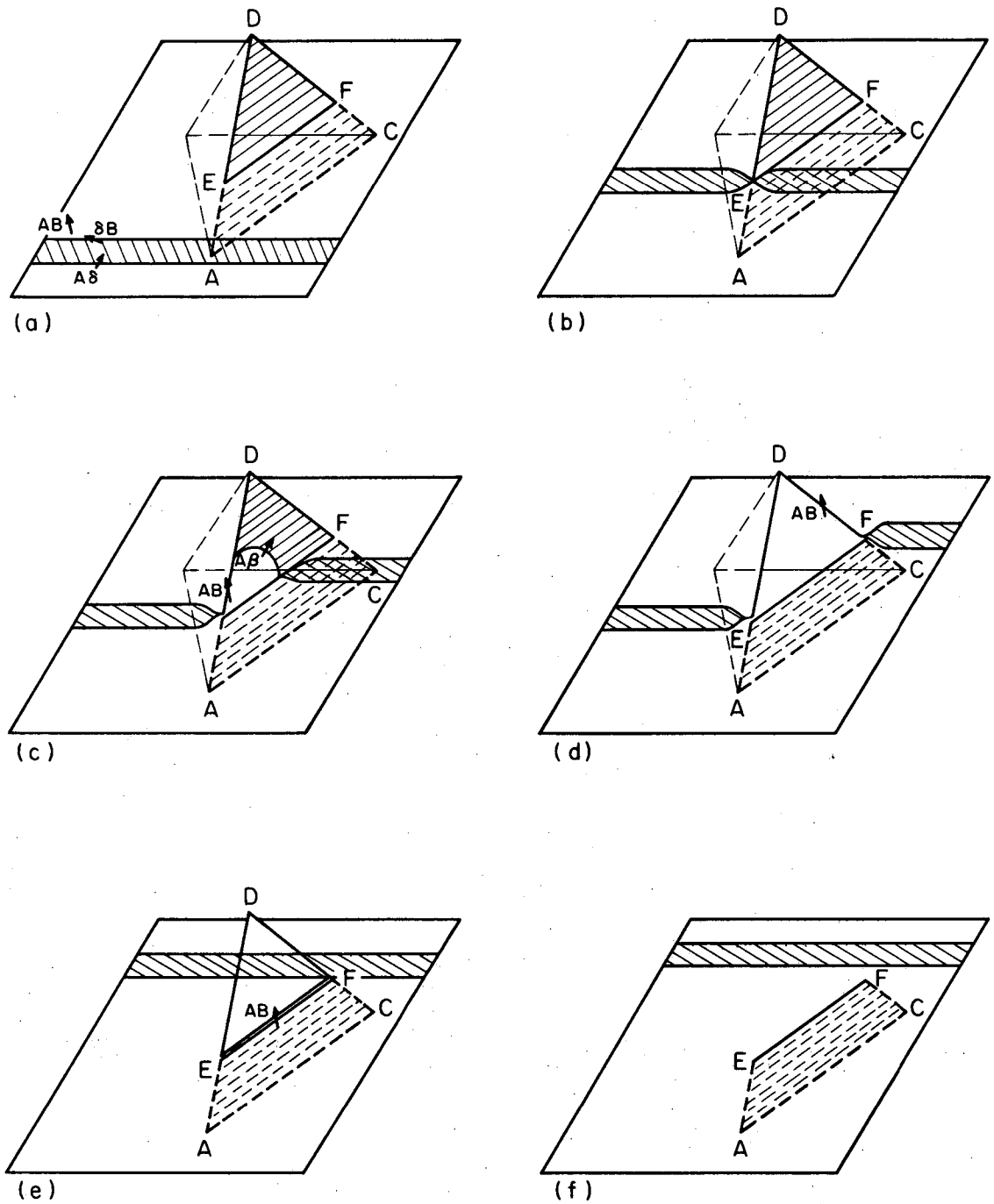

MUB 12964

Fig. 21 a-f The sequence of dislocation reactions that takes place when the moving dislocation intersects a stacking fault loop which does not lie in either of the slip planes of the interacting dislocation.

Figs. 22 and 23. The slip trace indentations of the three reactions shown in Figs. 22 and 23 are thought to result from, first, the conversion of the stacking fault loop to a perfect prismatic loop and second, the prismatic glide of the perfect loop to the surface of the foil. In reaction (2) of Fig. 22 and in the reaction of Fig. 23, the entire stacking fault of the loop is destroyed and converted to a perfect prismatic loop. In reaction (1) of Fig. 22 and reaction (2) of Fig. 26 only part of the stacking fault is destroyed. This result can be achieved only through the dislocation reaction

$$AB = A\alpha + \alpha B \tag{4}$$

where a perfect dislocation, AB, dissociates to Frank sessile, $A\alpha$, and Shockely partial, αB, dislocations.

2. Interactions in Which the Loop Lies in the Cross-Slip Plane of the Interacting Dislocation.

Case 2 occurs when the interacting dislocation, AB, intersects the stacking fault loop ADB which lies in the cross slip plane of the interacting dislocation. Figure 24 illustrates the sequence of dislocation reactions which can occur when this situation is realized.

a. The moving dislocation first must constrict from the extended form $A\delta + \delta B$ to the perfect form AB at the point of contact (Fig. 24b).

$$A\delta + \delta B = AB \tag{5}$$

b. The constricted segment of the interacting dislocation can then dissociate in the stacking fault of the loop into two Shockley partials, $A\gamma$ and γB, which removes the stacking fault each on its side (Fig. 24c).

$$AB = A\gamma + \gamma B \tag{6}$$

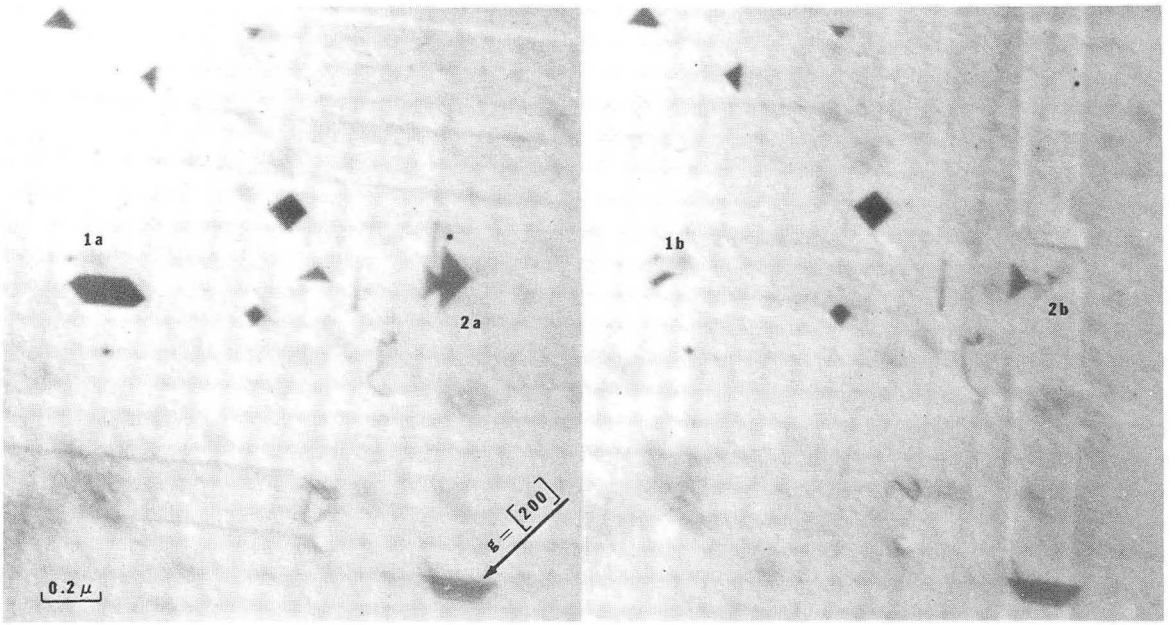

(a) (b)

IM 2331

Fig. 22 Interactions between a moving dislocation and a stacking fault loop which does not lie in either of the slip planes of the interacting dislocation [resulting in the complete or partial removal of the stacking fault and transformation of the Burgers vector of the loop from a/3⟨111⟩ to a/2⟨110⟩].

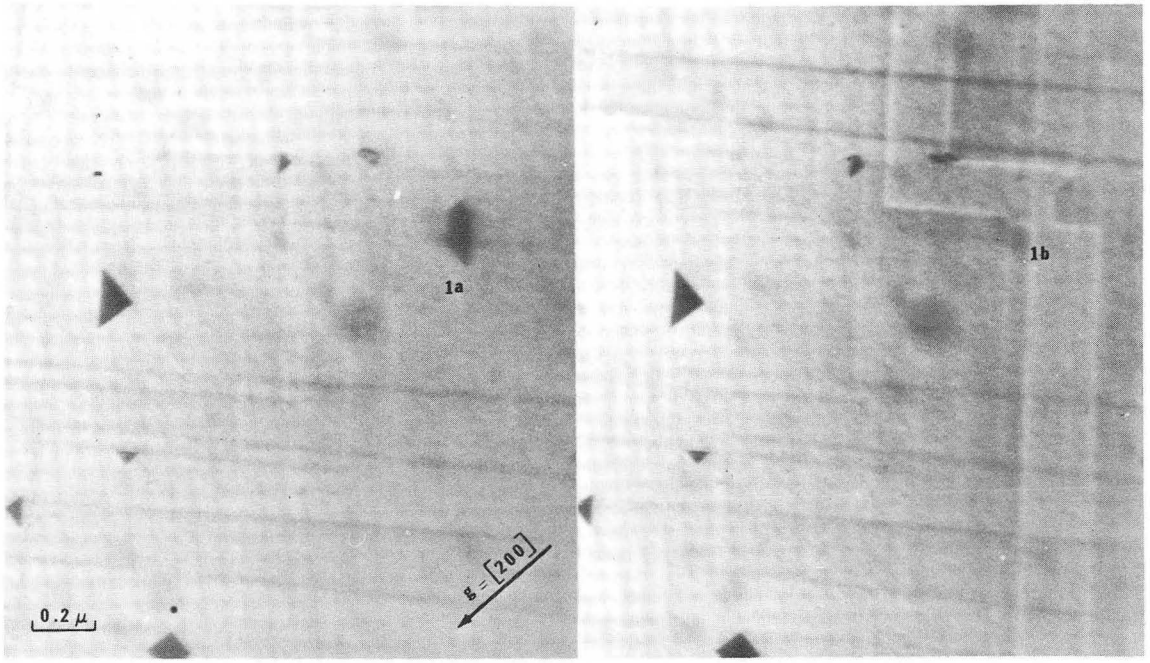

(a) (b)

IM 2325

Fig. 23 Interactions between a moving dislocation and a stacking fault loop which does not lie in either of the slip planes of the interacting dislocation [resulting in the complete or partial removal of the stacking fault and transformation of the Burgers vector of the loop from a/3⟨111⟩ to a/2⟨110⟩].

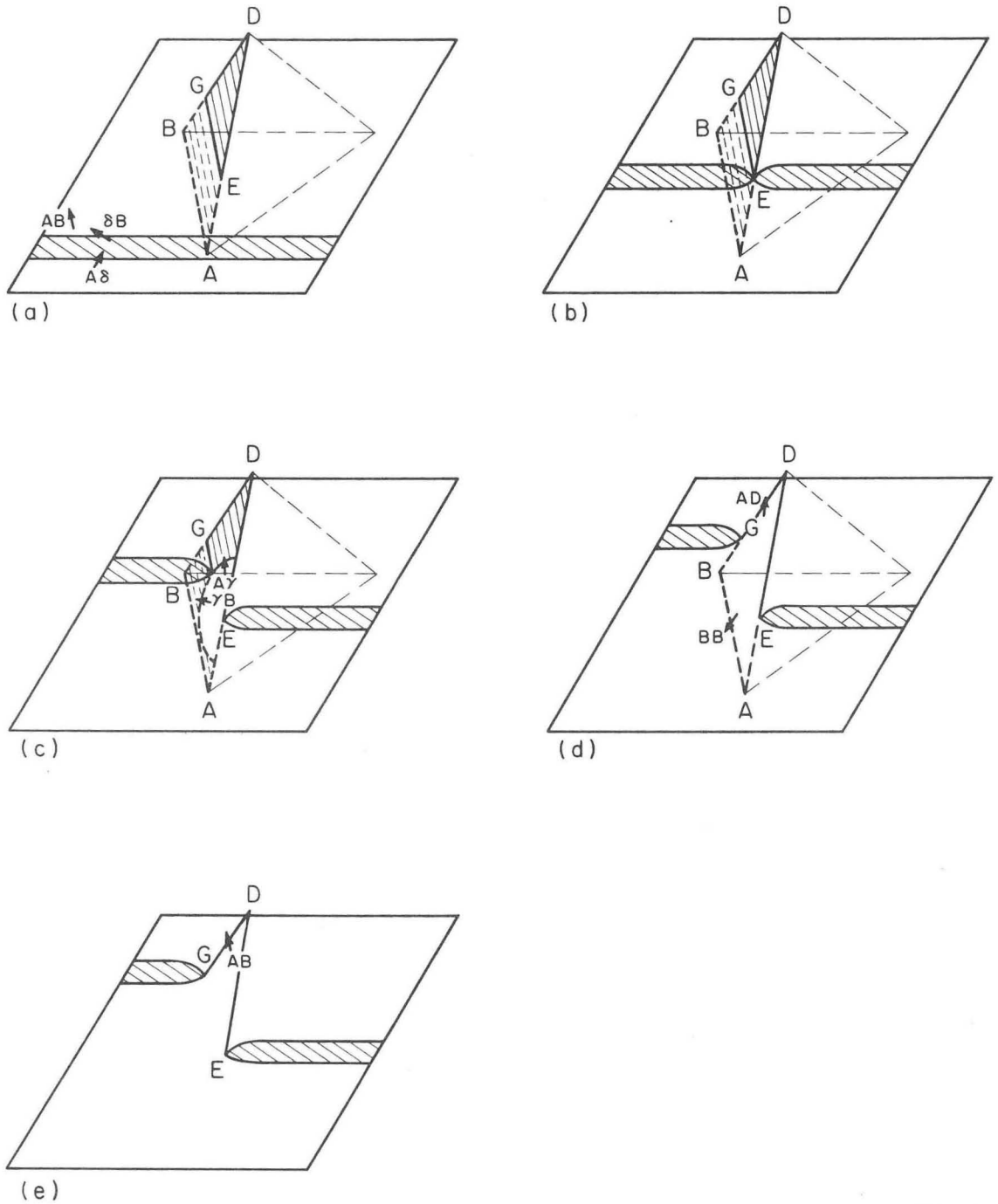

MUB 12965

Fig. 24 The sequence of dislocation reactions that takes place when the moving dislocation intersects a stacking fault loop which lies in the cross slip plane of the interacting dislocation.

c. The two Shockley partial dislocations can then recombine at the perimeter of the loop to form two dislocation segments of different Burgers vectors, AD and DB, forming nodes with the interacting dislocation (Fig. 24d).

$$A\gamma + \gamma D = AD \tag{7}$$

$$\gamma B + D\gamma = DB \tag{8}$$

d. The two dislocation segments can then recombine to form a single dislocation with the Burgers vector of the interacting dislocation (Fig. 24e).

$$AD + DB = AB \tag{9}$$

It would also be possible for the two sides of the interacting dislocation to combine, forming a jogless dislocation free to move while leaving behind a perfect prismatic loop as in the previous case.

The above series of reactions can be used to explain the results of the dislocation-stacking fault loop interactions which have occurred in Figs. 25, 26, and 27. Reaction (1) of Fig. 26 and the reactions of Figs. 25 and 27 illustrate the usual type of result obtained when the moving dislocation intersects a stacking fault loop lying in the dislocation's cross slip plane. In all three of these cases the two segments of the dislocation loop (Fig. 24c) resulting from the sweeping out of the two Shockley partial dislocations have combined to form a single dislocation segment in the cross slip plane having the same Burgers vector as that of the interacting dislocation.

3. <u>Interactions in Which the Loop Lies in a Plane Parallel to That of the Primary Slip Plane of the Interacting Dislocation</u>.

Case 3 occurs when the interacting dislocation, AB, comes close to the stacking fault loop, ABC, which lies in a plane parallel to the

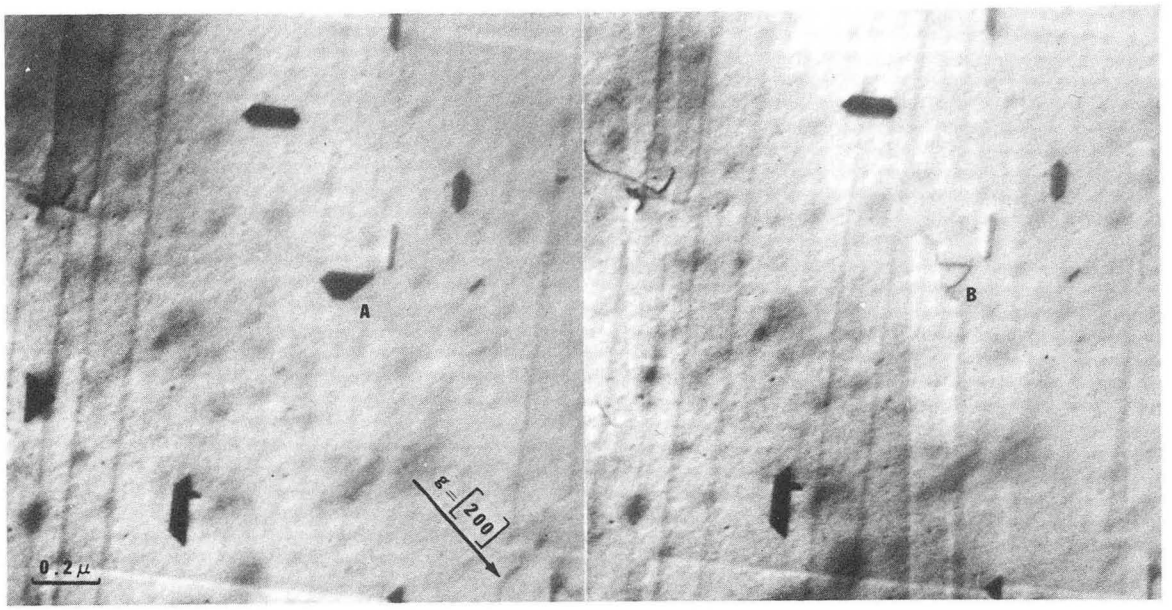

(a) (b)

IM 2327

Fig. 25 Interactions between a moving dislocation and a stacking fault loop which lies in the cross slip plane of the interacting dislocation [resulting in the complete removal of the stacking fault and transformation of the Burgers vector of the loop from a/3⟨111⟩ to a/2⟨110⟩].

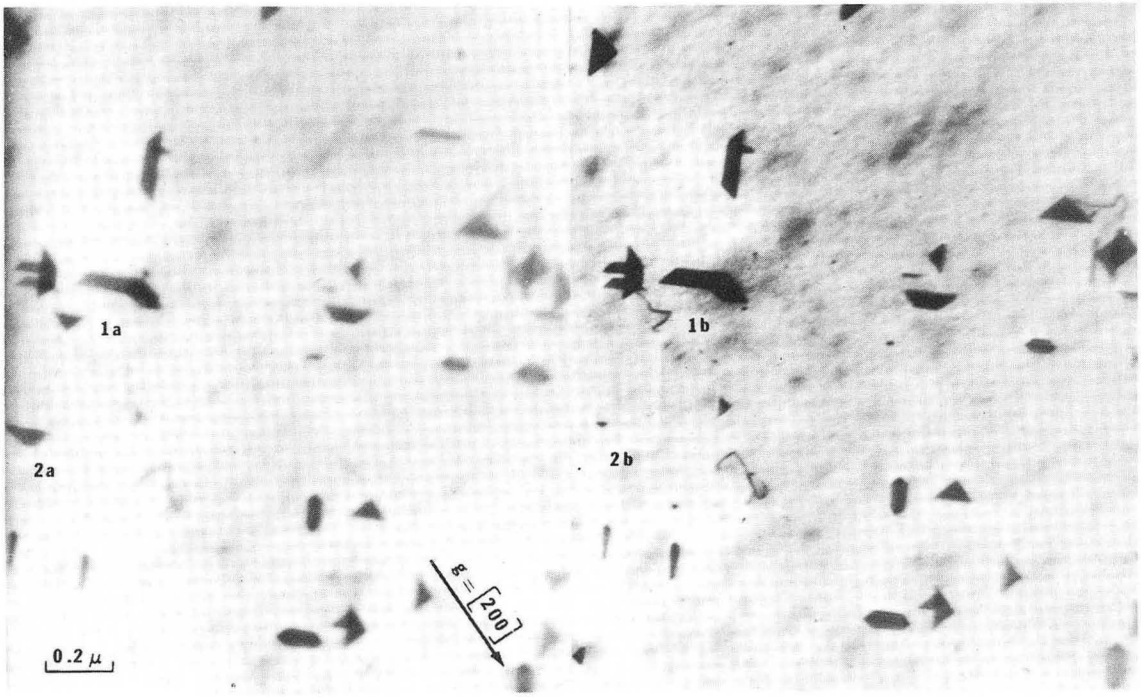

(a) (b)

TM 2336

Fig. 26 Interactions between a moving dislocation and a stacking fault loop which lies in the cross slip plane of the interacting dislocation [resulting in the complete removal of the stacking fault and transformation of the Burgers vector of the loop from a/3⟨111⟩ to a/2⟨110⟩.

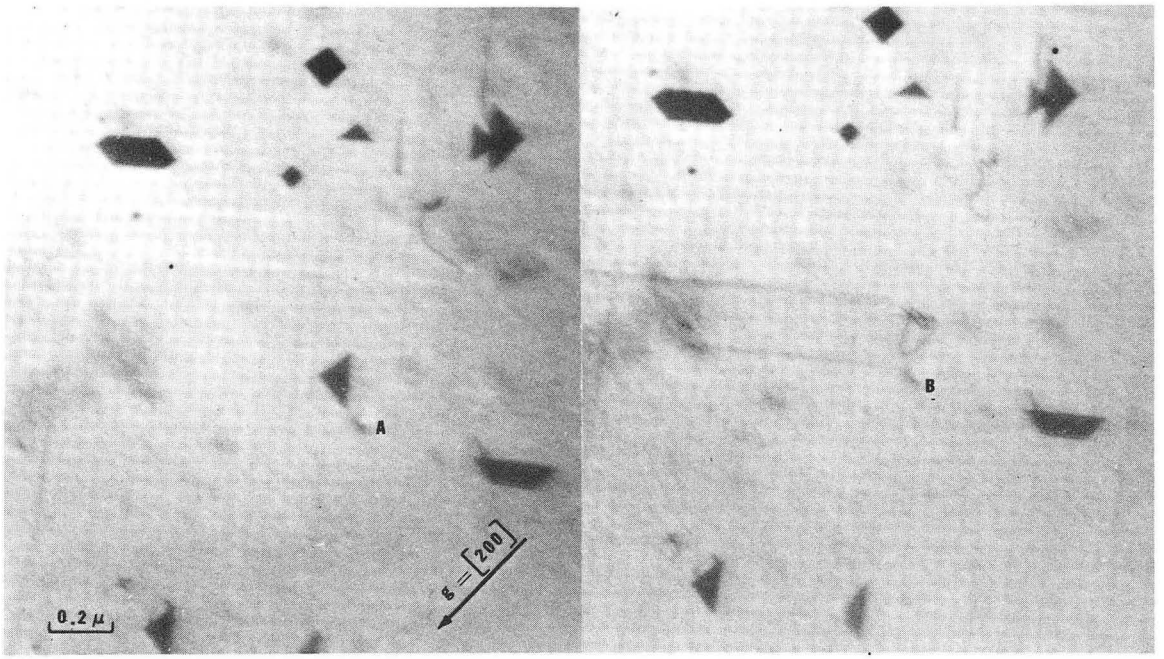

(a) (b)

IM 2323

Fig. 27 Interactions between a moving dislocation and a stacking fault loop which lies in the cross slip plane of the interacting dislocation [resulting in the complete removal of the stacking fault and transformation of the Burgers vector of the loop from a/3⟨111⟩ to a/2⟨110⟩].

primary slip plane of the moving dislocation. Figure 28 illustrates the sequence of dislocation reactions that can occur when this situation is realized.

a. In this case there is little probability of direct contact between the loop and the moving dislocation because they would have to lie in the same atomic layer. However, if the dislocation passes close to the loop, its stress field can cause nucleation of a Shockley partial dislocation in the stacking fault of the loop (Fig. 28b).

b. The stacking fault is swept away by the glide of the Shockley partial dislocation and recombines at the perimeter of the loop to form a perfect prismatic loop (Fig. 28c).

The reaction which has occurred in Figs. 29 and 30 can be explained by the above mechanism. In both of these cases non-contact interaction is evident as the slip traces of the moving dislocations have not been interrupted. In Fig. 29, the loop lies in a parallel plane to the moving dislocation while in Fig. 30 the loop lies in a non-parallel plane.

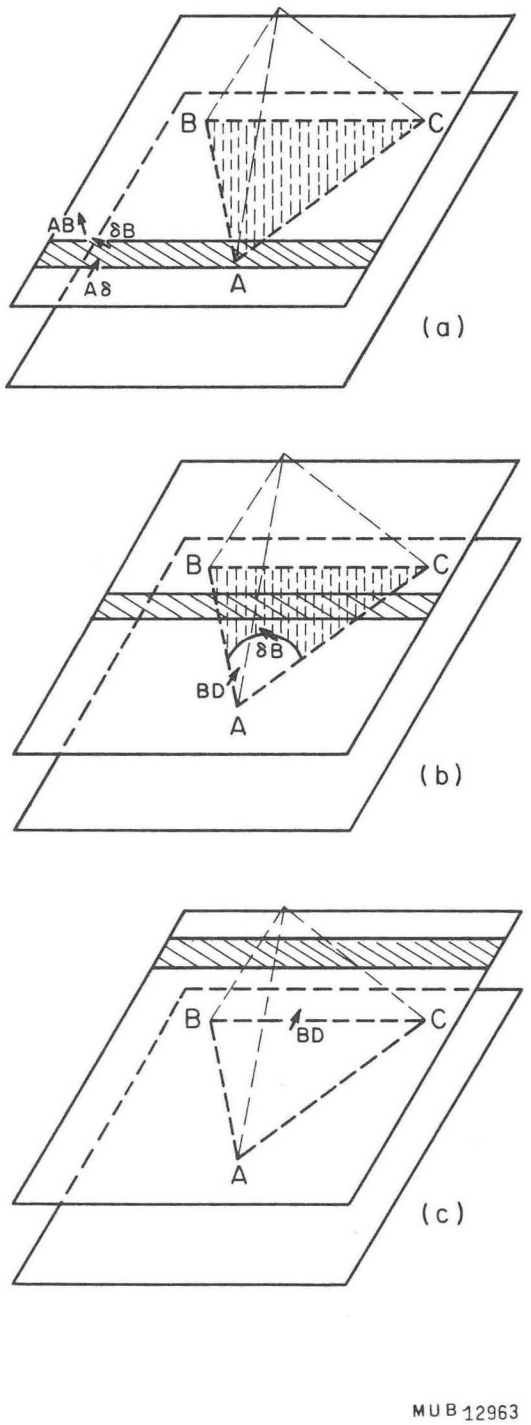

Fig. 28 The sequence of dislocation reactions that takes place when the moving dislocation passes close to but does not intersect a stacking fault loop.

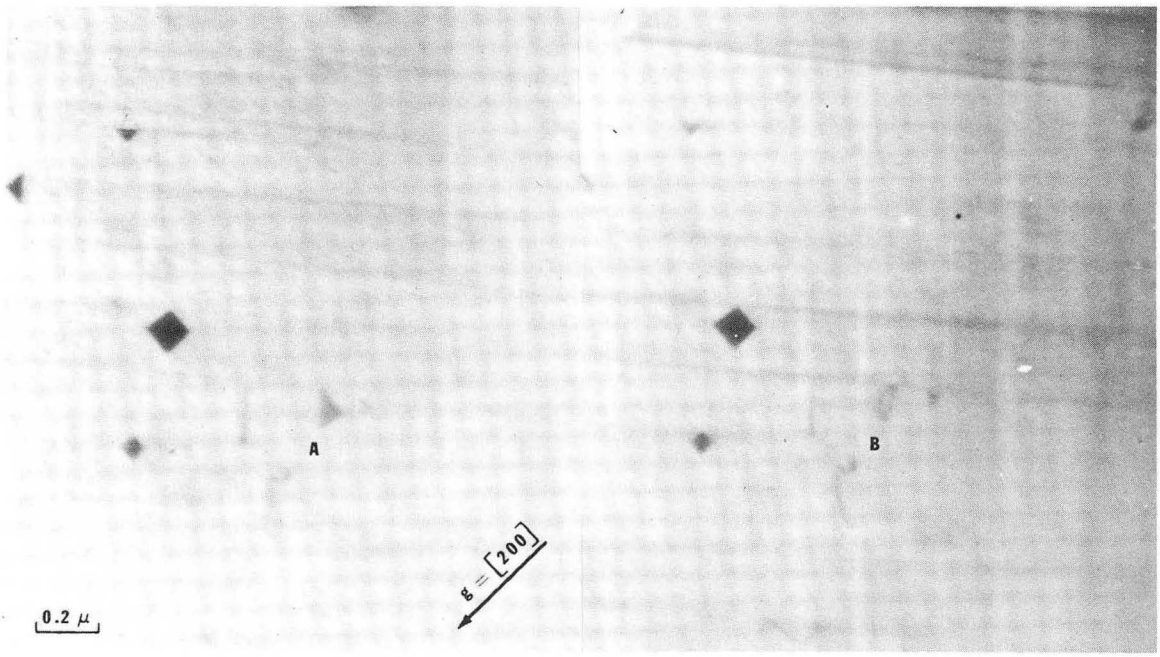

(a) (b)

IM 2326

Fig. 29 Interactions between a moving dislocation and a stacking fault loop which is not intersected by the interacting dislocation [resulting in the removal of the stacking fault and transformation of the Burgers vector of the loop from a/3⟨111⟩ to a/2⟨110⟩].

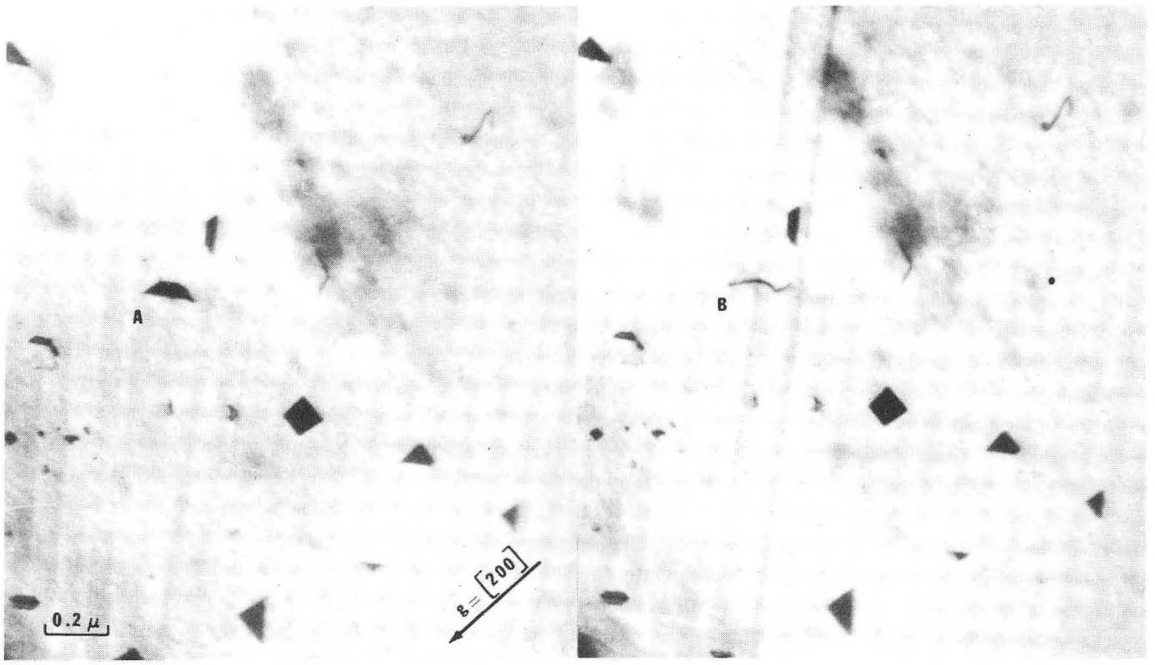

(a) (b)

IM 2324

Fig. 30 Interactions between a moving dislocation and a stacking fault loop which is not intersected by the interacting dislocation [resulting in the removal of the stacking fault and transformation of the Burgers vector of the loop from a/3⟨111⟩ to a/2⟨110⟩].

IV. CONCLUSIONS

Direct contact of a moving dislocation with a stacking fault tetrahedron produced one of two reaction products depending on the Burgers vectors and spatial relationship between the stacking fault tetrahedra and the interacting dislocations. In the first case contact interaction resulted in the collapse of the stacking fault tetrahedron and the production of large jogs in the interacting dislocation. In the second case, interaction resulted in the collapse of the stacking fault tetrahedron into a segment of a Frank sessile dislocation loop formed from one of the faces of the stacking fault tetrahedron. Two-thirds of the tetrahedra interactions resulted in the products of case one.

Interactions of dislocations with stacking fault tetrahedra without direct contact resulted in the collapse of the stacking fault tetrahedra into triangular Frank sessile dislocation loops.

Direct contact of a moving dislocation with a stacking fault loop resulted in two types of reaction products. In the first case interaction resulted in the complete removal of the stacking fault converting the $\frac{1}{3}\langle 111\rangle$ type dislocation loop into $\frac{1}{2}\langle 110\rangle$ segments which became part of the interacting dislocation. In the second case interaction resulted in only the partial removal of the stacking fault leaving behind a segment of the original stacking fault loop.

Interactions of dislocations with stacking fault loops without direct contact resulted in the conversion of the $\frac{1}{3}\langle 111\rangle$ stacking fault loop into a $\frac{1}{2}\langle 110\rangle$ type perfect prismatic loop.

APPENDIX

Flow Stress and the Constriction Energy

It will be assumed that for a certain range of experimental conditions the mechanisms described in the preceding section dominate in the deformation of the macroscopic specimen. The interaction with either the stacking fault tetrahedron or loop requires the interacting extended dislocation to constrict in order for reaction to take place. It is this constriction step which will be considered as the rate controlling one in determining an expression for the flow stress. The strain rate should follow the general relation:

$$\dot{\epsilon} = R(\Delta\epsilon) = k[C]_{SFL}\ \rho\{Ab\} \qquad (1)$$

where

R = rate of dislocation-stacking fault loop reaction

$\Delta\epsilon$ = strain resulting per reaction

k = rate constant for the dislocation stacking fault loop reaction

$[C]_{SFL}$ = concentration of stacking fault loops

ρ = density of dislocations

A = area swept out per reaction

b = Burgers vector of the interacting dislocation

That is, the strain rate is equal to the rate of interaction of the moving dislocation with the stacking fault loops times the strain resulting per reaction.

The rate constant, k, has the form

$$k = Be^{-E^*/kT} \qquad (2)$$

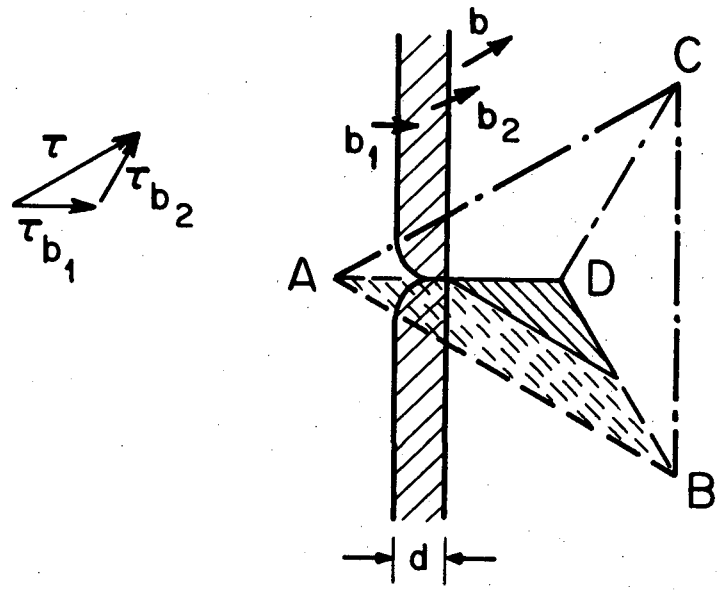

MUB 12961

Fig. A1 Schematic drawing of constriction needed in the interacting extended dislocation for contact interaction to occur between it and the stacking fault loop.

where

B = pre-exponential factor containing an entropy and frequency term

E^* = activation energy for the reaction

Combining Eqs. (1) and (2)

$$\dot{\epsilon} = B\{Ab\}\ \rho[C]_{SFL}\ e^{-E^*/kT} \qquad (3)$$

For the mechanism proposed, the activation energy for reaction should have the form

$$E^* = E_c - G\ \tau\ b^3 \qquad (4)$$

where

E_c = energy to constrict the extended dislocation

τ = stress on the dislocation

b = Burgers vector

G = geometry constant

From Stroh (1954) the constriction energy is a function of the width of the extended dislocation which is in turn inversely proportional to the stacking fault energy.

The value of τ, is usually expressed as a function of two terms

$$\tau = \tau_a - \tau_i \qquad (5)$$

where

τ_a = applied flow stress

τ_i = internal back stress

Combining Eqs. (3), (4), and (5) the following expression results for the flow stress,

$$\tau_a = \tau_i + \frac{E_c}{Gb^3} - \frac{kT}{Gb^3} \ln \frac{B\{Ab\}\rho[C]_{SFL}}{\dot{\epsilon}} \qquad (6)$$

It can be seen from Eq. (6) that the flow stress is strongly dependent on the stacking fault energy, γ_{SF}, and the temperature, T. Extrapolation of the flow stress to 0°K should give us a value for the constriction energy.

Other parameters which must be considered in the quenching hardening of gold are the defect density and size which control the number of interaction points as well as $\Delta\epsilon$, the strain resulting per reaction. In fact the effect of density can be studied since as was shown in Fig. 1 both the density and size can be varied over a wide range by alterations in the quenching and aging treatments. A very low density for example might permit the bowing of dislocations around stacking fault tetrahedra at stresses lower than that needed for contact interaction.

REFERENCES

1. J. Friedel, Dislocations (Pergamon Press, Oxford, 1964), p. 161.
2. P. B. Hirsch, A. Howie, R. B. Nicholson, D. W. Pashley and M. J. Whelan, Electron Microscopy of Thin Crystals (Butterworths Publishing Company, Washington, D.C., 1965), p. 271.
3. P. B. Hirsch and J. Silcox, Phil. Mag., 3, 987 (1958).
4. P. B. Hirsch and J. Silcox, Phil. Mag., 4, 72 (1959).
5. H. Kimura and R. Maddin, Lattice Defects in Quenched Metals (Academic Press, New York, 1965), p. 319.
6. M. Meshii and J. W. Kauffman, Acta Met., 7, 180 (1959).
7. T. Mori and M. Mschii, Acta Met., 12, 104 (1964).
8. G. Saada and J. Washburn, J. Phys. Soc. Japan, 18, Suppl. 1, 43 (1963).
9. A. N. Stroh, Proc. of the Phys. Soc. (London) B67, 427 (1954).
10. J. L. Strudel and J. Washburn, Phil. Mag. 9, 491 (1964).
11. G. I. Taylor, Proc. Roy. Soc., A145, 362 (1934).
12. N. Thompson, Proceedings of the Bristol Conference, London (1955).

PART II

I. INTRODUCTION

Quenched and aged gold has been shown by Silcox and Hirsch (1959) to form stacking fault tetrahedra.

These three-dimensional sessile defects consist of a tetrahedron of stacking faults bounded by $\frac{1}{6}\langle 110\rangle$ type stair rod dislocations. It has recently been shown by Yokota and Washburn (1967) that stacking fault loops can also be formed in quenched and aged gold by slight alteration in the usual quenching and aging treatments. Both of these sessile defects can be produced in a wide range of sizes, from as large as several thousand angstroms down to a few hundred. Through the direct observation technique of electron microscopy, the annealing kinetics of these tetrahedra and loops can be studied individually.

A number of investigators, among them Meshii and Kaufmann (1959) and Cottrell (1961) have studied the bulk annealing of stacking fault tetrahedra using the indirect methods of electrical resistivity and mechanical testing. They have found the stacking fault tetrahedron to be extremely stable. Recovery was found to take place at measurable rates for gold near 600°C and for silver at around 900°C.

A number of mechanisms have been proposed to explain the annealing behavior of stacking fault tetrahedra. The mechanisms may be divided into two classes, those involving only the successive emission of vancancies as proposed by DeJong and Koehler (1963) and those involving first the collapse to a planar defect before the emission of vacancies. The planar defect may be a triangular stacking fault loop as suggested by Silcox and Hirsch (1959) or a triangular perfect prismatic loop as

proposed by Kuhlmann-Wilsdorf (1965).

The DeJong-Koehler mechanism requires the formation of ledges in the faces of the stacking fault tetrahedron. The Silcox-Hirsch and the Kulhmann-Wilsdorf mechanisms each require the nucleation of Shockley partial dislocations from one or more tetrahedron corners. Jøssang and Hirth (1967) have recently calculated the total energies of intermediate truncated stacking fault tetrahedra and have arrived at the conclusion that the ledge mechanism is responsible for the annealing of stacking fault tetrahedra due to the extremely large activation energy required in either of the collapse mechanisms. If in fact, Jøssang and Hirth are correct in their conclusion, annealing of stacking fault tetrahedra as revealed by direct observation under the electron microscope should show tetrahedra shrink and disappear as tetrahedra. If however either of the collapse mechanisms should be responsible for the recovery process, this also can be determined under direct microscope observation. In this case, the orientation of the specimen as well as the diffraction conditions must be carefully chosen so as to clearly reveal the products of collapse.

A study of the annealing behavior of stacking fault loops by transmission electron microscopy allows an almost direct check on several important aspects of the theory of dislocation climb. Although Tartour (1967). Dobson et al. (1967) and others have recently done extensive work on aluminum, a face-centered cubic metal with a high stacking fault energy, very little work has been done on other fcc materials of much lower stacking fault energy such as gold. Because of the low stacking fault energy for gold, the $\frac{1}{3}\langle 111\rangle$ dislocation surrounding the stacking fault loop can dissociate into $\frac{1}{6}\langle 110\rangle$ type stair rod and $\frac{1}{6}\langle 112\rangle$ Shockley

paraial dislocations. A study of the annealing behavior of an extended loop should yield valuable insight into the mechanisms of extended jog formation and motion.

The subject of the present study is the annealing of quenched and aged gold containing stacking fault tetrahedra and loops. The purpose of the study is to obtain direct experimental evidence through transmission electron micrographs of the processes responsible for the annealing. These results will be used to formulate and refine theoretical models for the annealing of stacking fault tetrahedra and loops.

II. EXPERIMENTAL PROCEDURE

A. Specimen Preparation

Specimens 25 mm long by 12 mm wide and 75 or 125 microns thick were prepared from sheets of 99.999% pure gold obtained from Cominco Products Inc. of Spokane, Washington. The thin sheet specimens were first annealed in air at 1000°C for 48 hrs. producing grains of 0.4 mm average grain size and ⟨001⟩ preferred orientation. The specimens were then quenched from a temperature of 1000°C into an ice water bath and aged for 1 to 2 hrs. at 150, 100 or 0°C.

B. Thin Foil Preparation

Thin foil samples suitable for observation under the electron microscope were prepared by the modified window technique described in detail in Part I. In place of the non-corrosive holders as described in the experimental procedures of Part I, wider specimens were employed instead which allowed masking of at least a 3 mm edge around the specimen. The masked edge acted in a similar manner as did the holders in minimizing plastic deformation of the specimen during thinning.

A variation of the electropolishing technique described in Part I was used successfully a number of times in the present study. In this technique the specimen was allowed to etch slightly in the fast polishing step of the procedure. This was accomplished by increasing the hydrochloric acid content of the electropolishing solution or by raising the temperature of the constant temperature bath. When the etched specimen was further polished using the more controllable chromic acid solution, entire grains were separated from the specimen. These grains were recovered from the solution, rinsed and stored in ethyl alcohol at 0°C.

C. Electron Microscope Technique

A Siemens 1A electron microscope operated at 100 kV with a beam current less than 10 μamps was used to make all of the microscope observations. A detachable specimen cap constructed of gold was used with the standard Siemens single tilt specimen holder and stage. The detachable cap permitted the annealing of the thin foil specimens in a furnace outside of the microscope. The hot stage technique, where the specimen is annealed directly in the microscope was used in an initial study to determine the gross qualitative features of the annealing process. In this case the difficulty of controlling and measuring temperatures could be ignored. Whenever quantitative measurements were desired, however, the annealing treatments were conducted outside the microscope in an 1"×20" resistance tube furnace controlled to ±1°C. An inert argon atmosphere was introduced at a rate of 2 cu. ft/hr. See the diagram of Fig. 1 which shows the location of the cap and specimen as well as the controlling and recording thermocouples in the furnace.

Besides the gold specimen cap, a pair of 100 mesh gold grids were also used so that the cap assembly was constructed entirely of gold. These precautions were taken so as to minimize the chances of contamination as well as plastic deformation to the specimen from differential thermal strains. The specimen was fixed stationary in the cap by carefully interweaving the pair of ductile gold grids around the specimen.

Because the single, instead of the double tilting arrangement was used, the necessary diffraction conditions were obtained by making slight adjustments in the specimen orientation by rotating the specimen and grids within the cap. Therefore a number of adjustments were necessary

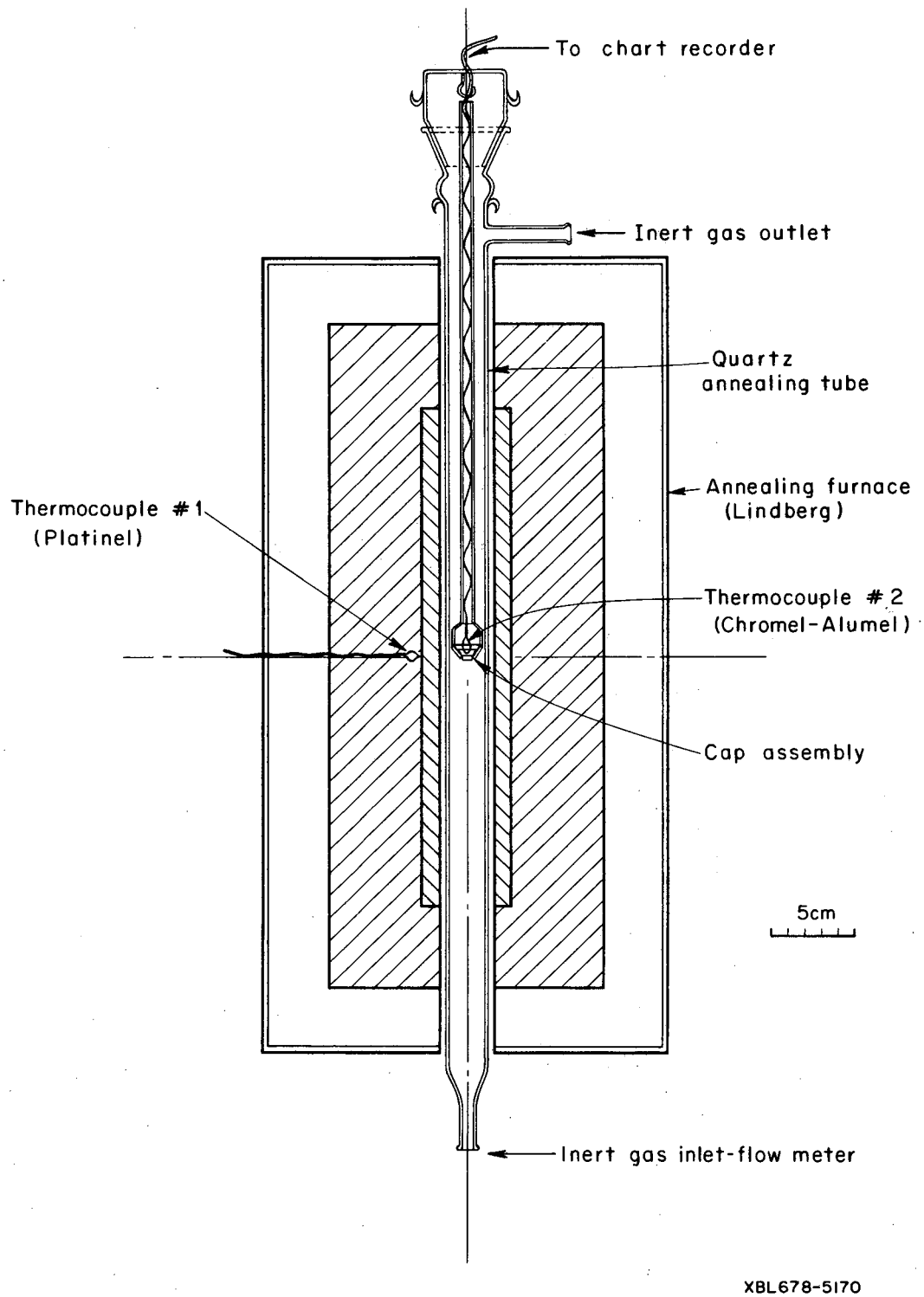

Fig. 1 Annealing furnace showing location of specimen cap and controlling and recording thermocouples

initially to achieve the desired diffraction condition. When the correct conditions were once obtained however, it was found relatively simple to achieve the same orientation a second time. This aspect of the technique was found extremely important as many annealing treatments outside the microscope had to be performed. This ease resulted from having to adjust only one axis of tilt instead of two as when the double tilt stage and holder are used.

Microscope observations were recorded on Kodak electron image plates. Plates were used instead of the more economical fils so as to avoid any measurement errors as a result of film shrinkage. Moreover the 2-1/2x3-1/2 in. plates allowed a larger area of observation than did the film.

A serious problem in making repeated observations of a process under study was in locating a particular area a number of times in the microscope. Although it was not always possible, unusual features e.g., bend contours, dirt spots, etd., were used to locate general areas. Then developed plates of previously taken observations were compared to locate the exact areas.

Magnification errors were avoided by making calibration checks before and after each annealing experiment using a calibrated replica grid. If observations were not made all in one sitting or if use of the microscope was interrupted by break down, additional magnification checks were made. In the case of the loop annealing study fixed positions in the micrographs were sought as well. This was accomplished by using three or more small stacking fault tetrahedra as reference points which fixed both the plane and the magnification of the observation.

III. RESULTS AND DISCUSSION

A. Annealing of Stacking Fault Tetrahedra

1. Experimental Observations

Figures 2a and b are micrographs taken of an area before and after 30 minutes annealing at a temperature of 175°C. Note that the complete stacking fault tetrahedra (1) and (3) which appear as squares in Fig. 2a, have become triangular Frank sessile dislocation loops in Fig. 2b. This same collapse has occurred for the stacking fault tetrahedron (2) that cuts one of the surfaces of the foil. The resulting Frank loop in this case appears as a trapezoid. The collapse of stacking fault tetrahedron (4) may have been aided by the stress field of the dislocation (5). For the other three examples, however, the resulting Frank loops do not lie on parallel planes, suggesting that stresses that may have been present during annealing did not aid significantly in their collapse.

The tetrahedra in Fig. 2 were in the size range 1000-2000Å. Smaller tetrahedra, on the order of 100-200Å generally required higher temperatures and/or longer times for collapse. Figures 3a, b, c, and d are micrographs taken of an area annealed for a) 0, b) 30, c) 60, and d) 90 minutes at 400°C showing the collapse of smaller stacking fault tetrahedra to triangular Frank sessile loops. Reactions can be seen at the positions which have been circled. After collapse of the tetrahedron the resulting loop shrinks maintaining sides parallel to the ⟨110⟩ directions.

Figure 4 shows the annealing process of an area containing tetrahedra of a wide size distribution. The complete sequence of the annealing steps from collapse of the tetrahedra to shrinkage of the loops at 300°C are illustrated. In Fig. 4b the largest of the stacking fault tetrahedra

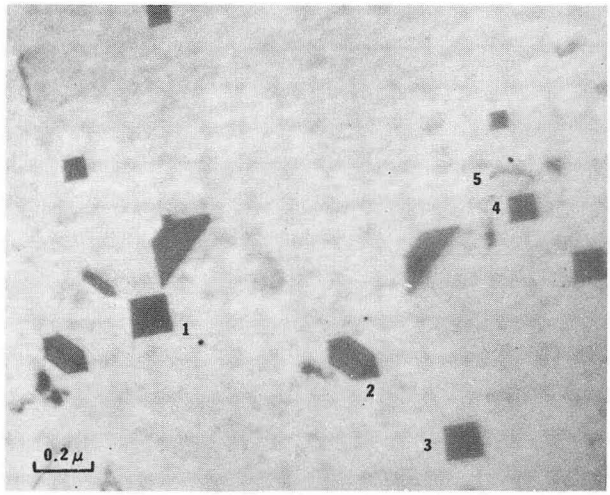

(a)

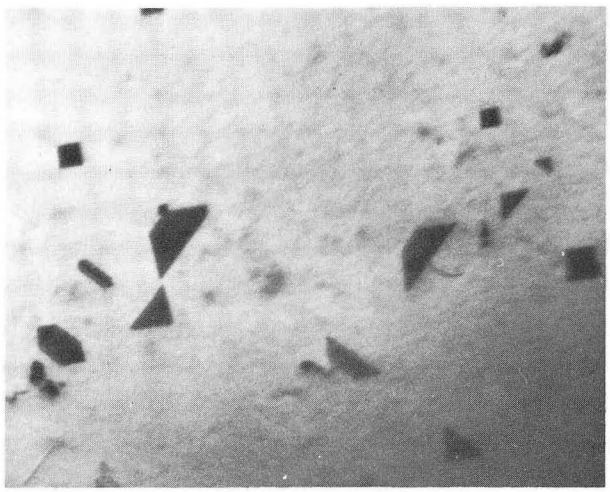

(b)

XBB 6711-6574

Fig. 2 Collapse of stacking fault tetrahedra to triangular stacking fault loops at 175°C after 30 minutes annealing.

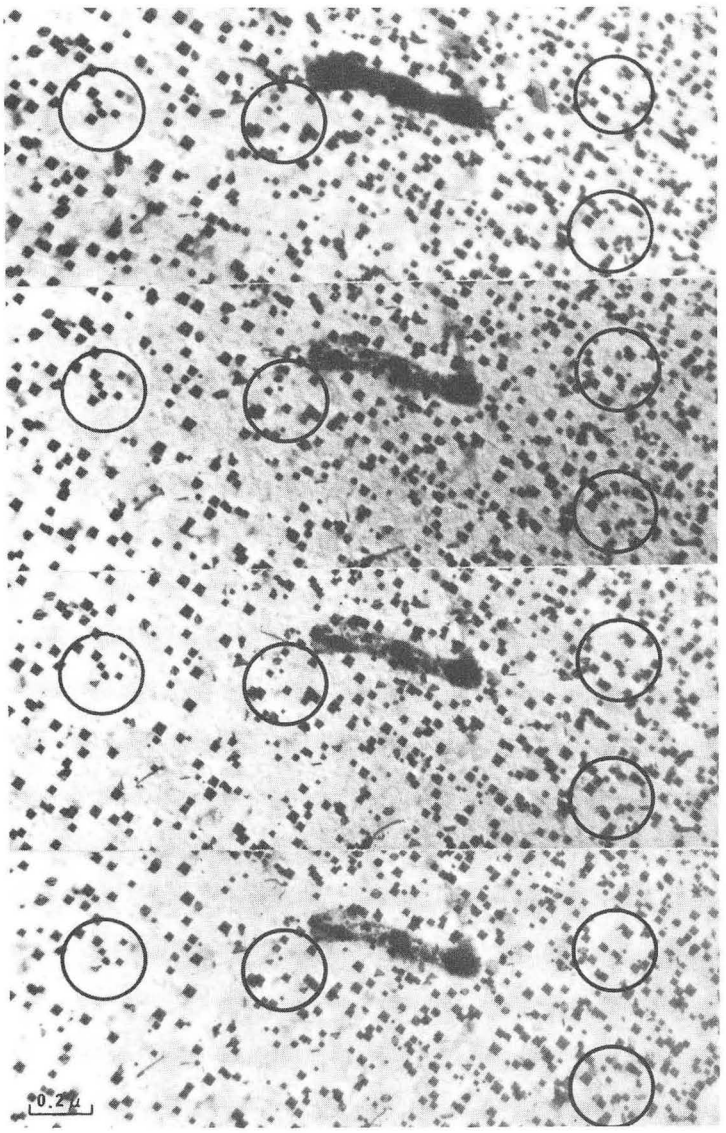

XBB 6711 6572

Fig. 3 Collapse of stacking fault tetrahedra to triangular stacking fault loops at 400°C after a) 0, b) 30, c) 60 and d) 90 minutes annealing; circles locate areas where collapse has taken place.

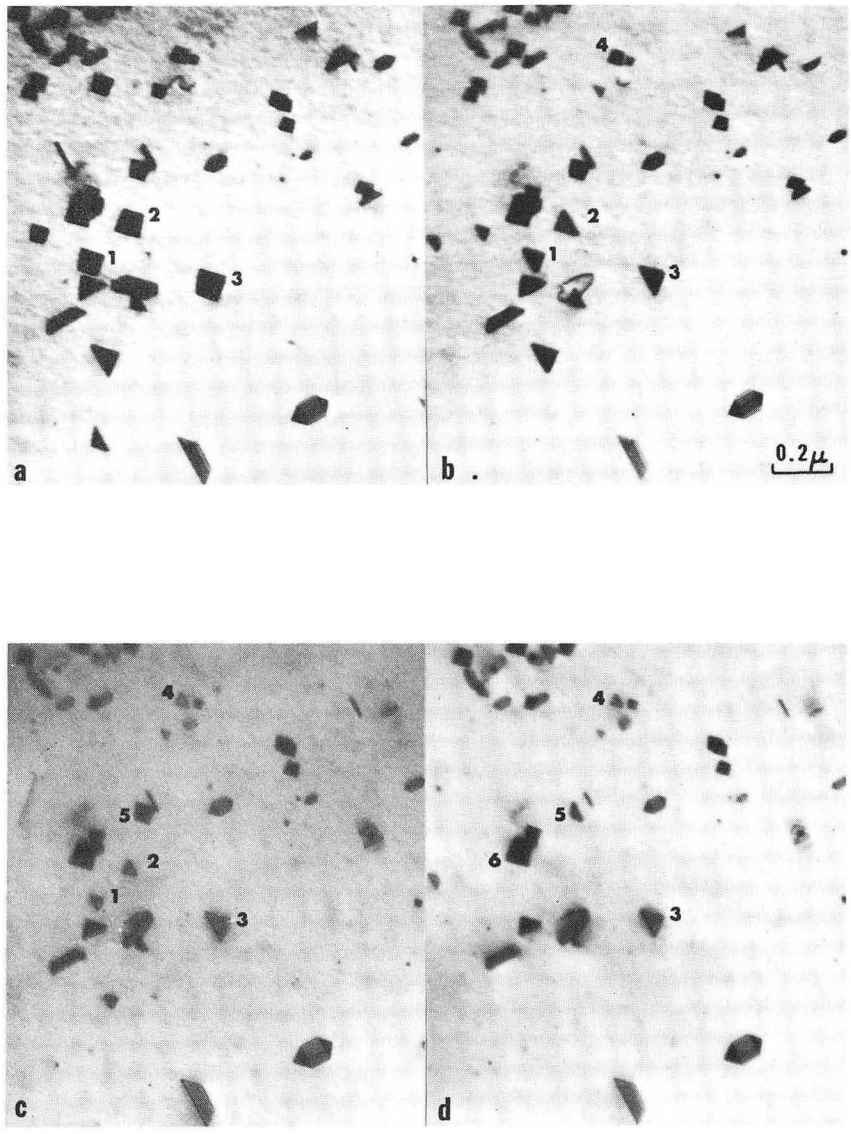

XBB 6711 6568

Fig. 4 Collapse of stacking fault tetrahedra and subsequent shrinkage of stacking fault loops at 300°C after a) 0, b) 2, c) 5, d) 9, e) 17, f) 25 and g) 34 hours annealing. (see next page)

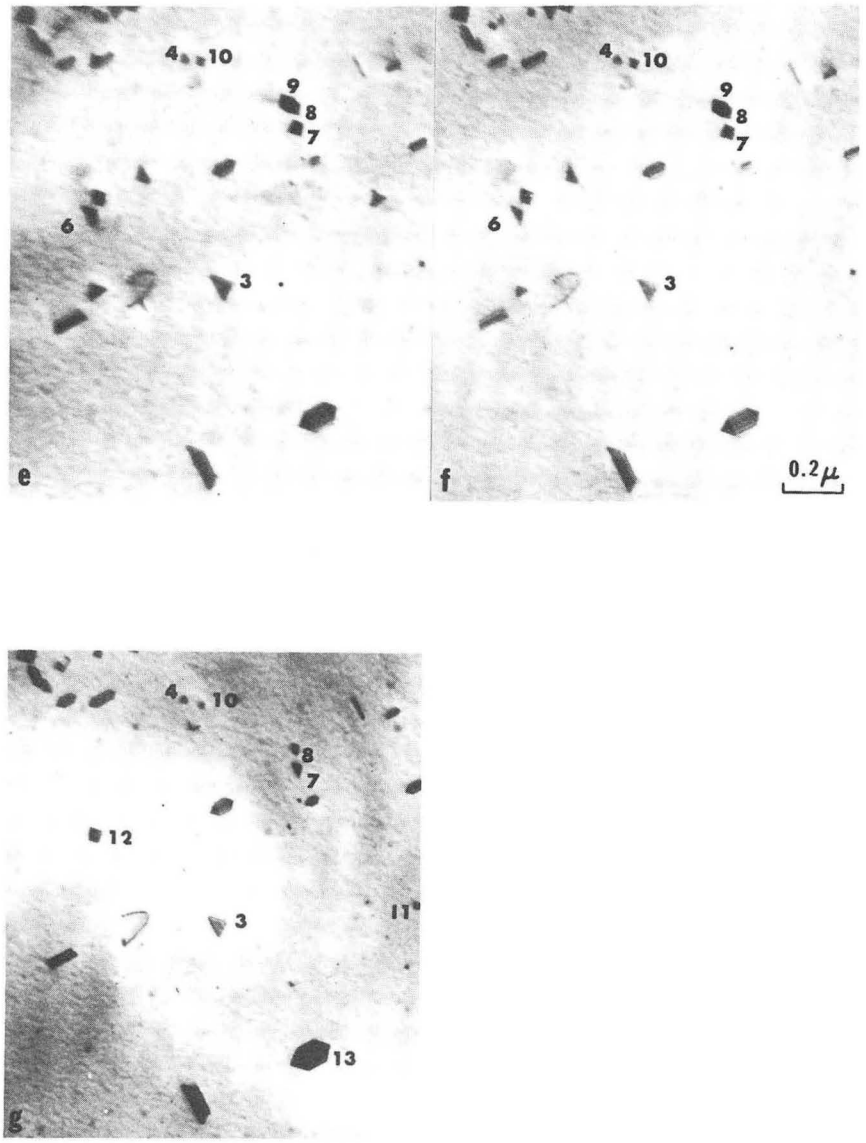

XBB 6711-6569

Fig. 4 (continued)

1, 2, and 3 have collapsed to triangular stacking fault loops. In Fig. 4d the smaller tetrahedra 4 and 5 have collapsed and by Fig. 4g the smallest of the complete stacking fault tetrahedra 7,8,9, and 10 have finally collapsed. Note, however that the large truncated tetrahedra 13 as well as others in Fig. 4g have yet to collapse. The high stability of these truncated stacking fault tetrahedra is quite unexpected since intersection by the surface removes segments of stair rods which would in the complete tetrahedron act as barriers in the collapse process. Resolution of this apparent incongruity will be postponed to a later section where all aspects of the mechanisms responsible for stacking fault tetrahedra collapse will be discussed together.

Also unexpected is the wide variation in the shrinkage behavior shown by the Frank sessile loops that have formed from collapse of the tetrahedra. For example, of the loops 1, 2, and 3 which have collapsed in Fig. 4b only loop 3 is still present after over 30 hours of annealing. Loop 1 and 2 have shrunk much faster having completely disappeared in less than 10 hours annealing as shown in Fig. 4d.

From a large number of observations such as described above a number of generalizations can be made about the annealing of stacking fault tetrahedra:

a) Stacking fault tetrahedra in a wide size range, 2000-100Å readily collapsed to triangular stacking fault loops.

b) In the same temperature range, 400 to 150°C, stacking fault tetrahedra did not shrink as tetrahedra. That is all of the stacking fault tetrahedra which eventually disappeared, annealed out by first collapsing to Frank sessile dislocation loops and then shrank as loops.

c) The larger stacking fault tetrahedra collapsed at lower temperatures and shorter times as compared to the smaller tetrahedra which required higher temperatures and longer times. That is, the collapse of stacking fault tetrahedra appears to be size dependent. An exception to this general behavior is the annealing of stacking fault tetrahedra cut by the surface of the thin foil. For the same edge length, the truncated tetrahedra appear to be more stable than the complete tetrahedra.

d) The shrinkage of the Frank sessile dislocation loops were quite irregular, some loops shrinking quite rapidly and others nearby shrinking only very little. Furthermore, not all sides of the same loop appeared to shrink equally.

Any mechanism which might be proposed to explain the annealing of stacking fault tetrahedra must of course include and explain the above observations.

2. Collapse of Stacking-Fault Tetrahedra

From the experimental observations of the previous section the recovery of stacking fault tetrahedra in gold has been found to occur through collapse of the tetrahedra into stacking fault loops. Further recovery it was found takes place through the shrinkage of these loops rather than through the process of tetrahedra shrinking directly as tetrahedra. The ledge mechanism by which stacking fault tetrahedra could shrink directly as tetrahedra was first suggested by de Jong and Koehler (1963) and later expanded by Kimura et al (1963). The mechanism requires that ledges nucleate and move in the stacking fault faces as shown in Fig. 5. Two types of stacking fault ledges are possible each having quite different characteristics. The ledge which faces toward an edge of the tetrahedra as shown in Fig. 5a, resembles a row of 1/3 vacancies, while the second type of ledge which faces toward a corner, Fig. 5b, may be regarded as a row of 1/3 interstitials. The stair rod dislocations bounding the vacancy ledge are of the $\frac{1}{6}\langle 110\rangle$ type while the interstitial ledges are associated with $\frac{1}{3}\langle 100\rangle$ stair rods. Hirsch (1962) has estimated the energy of the interstitial ledges to be 2 to 3 times that of the vacancy ledges. Kuhlmann-Wilsdorf (1965) has further shown that in order for shrinkage to occur by interstitial ledges a very high activation energy must be overcome. A minimum vacancy undersaturation of 0.2 at 600°C,[1] is needed before the barrier energy can be appreciably reduced. The required 0.2 undersaturation, however cannot conceivably be realized even neglecting the contributions of other vacancy sources.

1. The known critical temperature for annealing of stacking fault tetrahedra in gold.

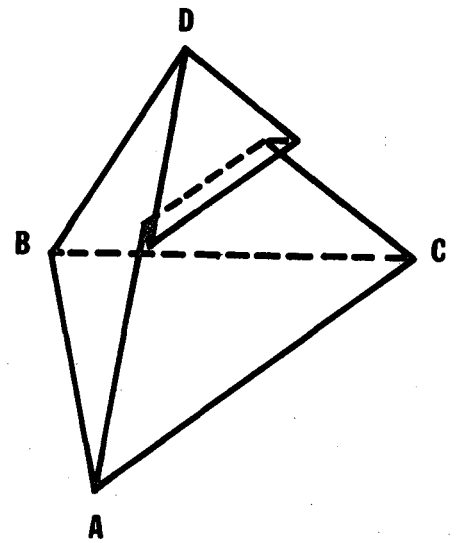

(a)

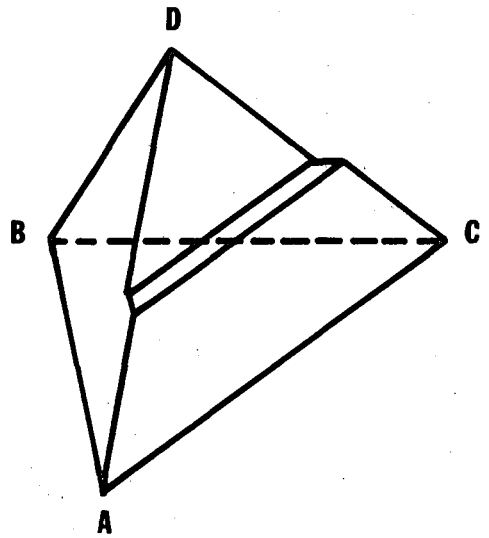

(b)

XBL 686-1120

Fig. 5 (a) Vacancy and (b) interstitial ledges on stacking fault tetrahedra

She then suggested that vacancy ledges nucleated from edges instead of corners could possibly operate to effect shrinkage. However this mechanism is feasible only if the line energy of vacancy ledges is much less than generally acknowledged (from 0.2 eV to 0.05 eV per atomic plane). The generally accepted 0.2 eV value for the line energy of the ledge would make, using her relationship, the nucleation energy approximately 15 eV for a 1000Å tetrahedron.

As stated earlier however, no tetrahedra were observed to anneal out through any of the above ledge mechanisms. Instead, annealing resulted through the collapse of tetrahedra into loops which then shrank through the emission of vacancies. Kulhmann-Wilsdorf was the first to suggest this alternate annealing mechanism. She viewed the rapid annealing of tetrahedra as noted by Cottrell (1961) through resistivity measurements at the 600°C critical temperature, to be the result of a chain reaction in which collapsing tetrahedra provided vacancies for further tetrahedra to grow to their limiting size and collapse and so on.

The collapse of a stacking fault tetrahedron to a Frank sessile loop involves the reaction

$$\text{SFT} \longrightarrow \text{FSL} \qquad (1)$$

requiring the nucleation of one or more Shockley partial dislocations at some point on the SFT. The rate of tetrahedra collapse can be expressed by the relation

$$R = k_1[\text{SFT}]$$

where [SFT] is the density or concentration of stacking fault tetrahedra in the above expression. The rate constant, k_1, has the general form

$$k_1 = Ae^{-E_1^A/kT}$$

where

E_1^A = activation energy for the reaction

A = pre-exponential factor which includes frequency and entropy terms

k = Boltzmann's constant

T = absolute temperature

To be able to predict the rate of annealing of stacking fault tetrahedra, it is necessary to first examine the various ways in which collapse can take place and second to make an estimate of the barrier or activation energy.

Before proceeding to a detailed discussion of mechanisms of collapse and their activation energies a number of terms and concepts should first be defined and clarified.

1) E_{SFT} and E_{FSL} are the energies of the stacking fault tetrahedron and the triangular Frank sessile loop defects respectively. The energy of the defects can be thought of as composed to two terms:

$$E_T = \Sigma E_s + \Sigma E_I$$

where

E_T = total energy of defect

E_s = self energies of the dislocations and stacking faults comprising the defect

E_I = interaction energies of the various dislocation segments of the defect.

2) ΔE is the difference in the total energies between the SFT and the FSL of the same edge length, ℓ.

$$\Delta E = E_{SFT} - E_{FSL}$$

ΔE is represented by the shaded area in Fig. 6.

3) E_1^A is the activation energy for the reaction SFT $\xrightarrow{k_1}$ FSL. E^* is the activation energy for the collapse process when the total energies of the SFT and FSL are equal (position 2 of Fig. 6). In region 1

$$E_1^A = \Delta E + E^*$$

and in region 3

$$E_1^A = E^*$$

E^* should not be thought of as a constant since it can vary with the size of the SFT. It is the energy which must be supplied by thermal fluctuation and/or external stress in order for collapse to occur, even when the SFT is unstable with respect to the FSL configuration.

In the discussion to follow, it will be viewed as the energy needed to nucleate one or more Shockley partials in the face, E_f^* edge E_e^* or corner, E_c^*, of the SFT to effect collapse to a FSL.

Three general mechanisms for the collapse of SFT to FSL can be visualized, each involving the nucleation of one or more Shockley partial dislocations. The first mechanism involves the nucleation of a Shockley partial loop in one of the four faces of the SFT. The dislocation reactions involved in the collapse are shown in Fig. 7. If the SFT we are considering is very large the loop interaction with the neighboring stair rods can be neglected and the total energy of the

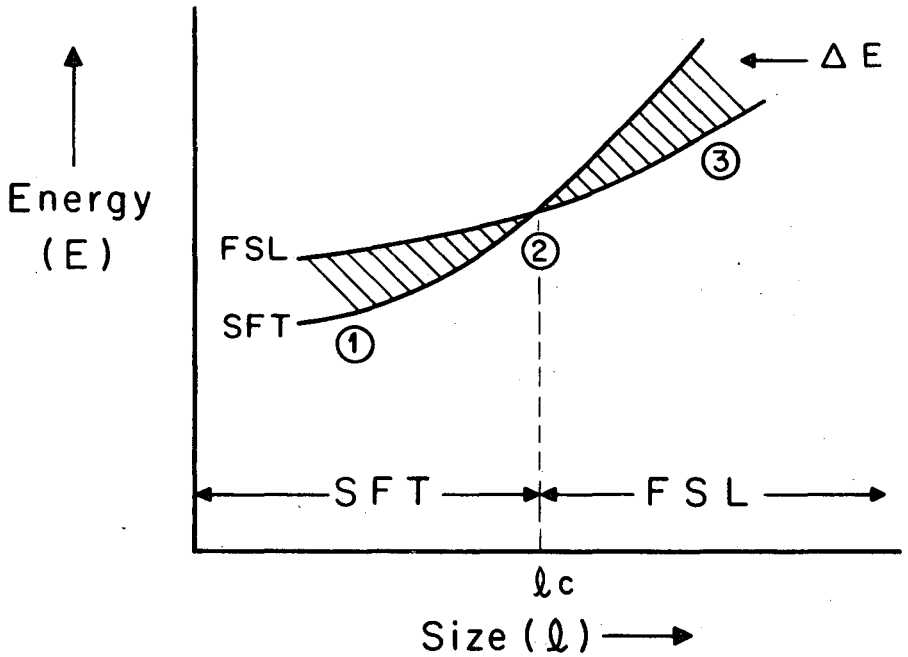

(a)

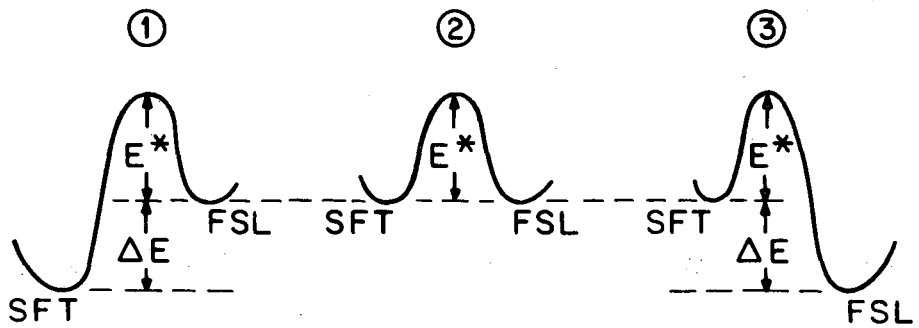

(b)

MUB-12802

Fig. 6 (a) Energy versus defect edge length for Frank sessile loops (FSL) and stacking fault tetrahedra (SFT)

(b) Energy barrier profiles for 1) $\ell < \ell_c$, 2) $\ell = \ell_c$ 3) $\ell > \ell_c$

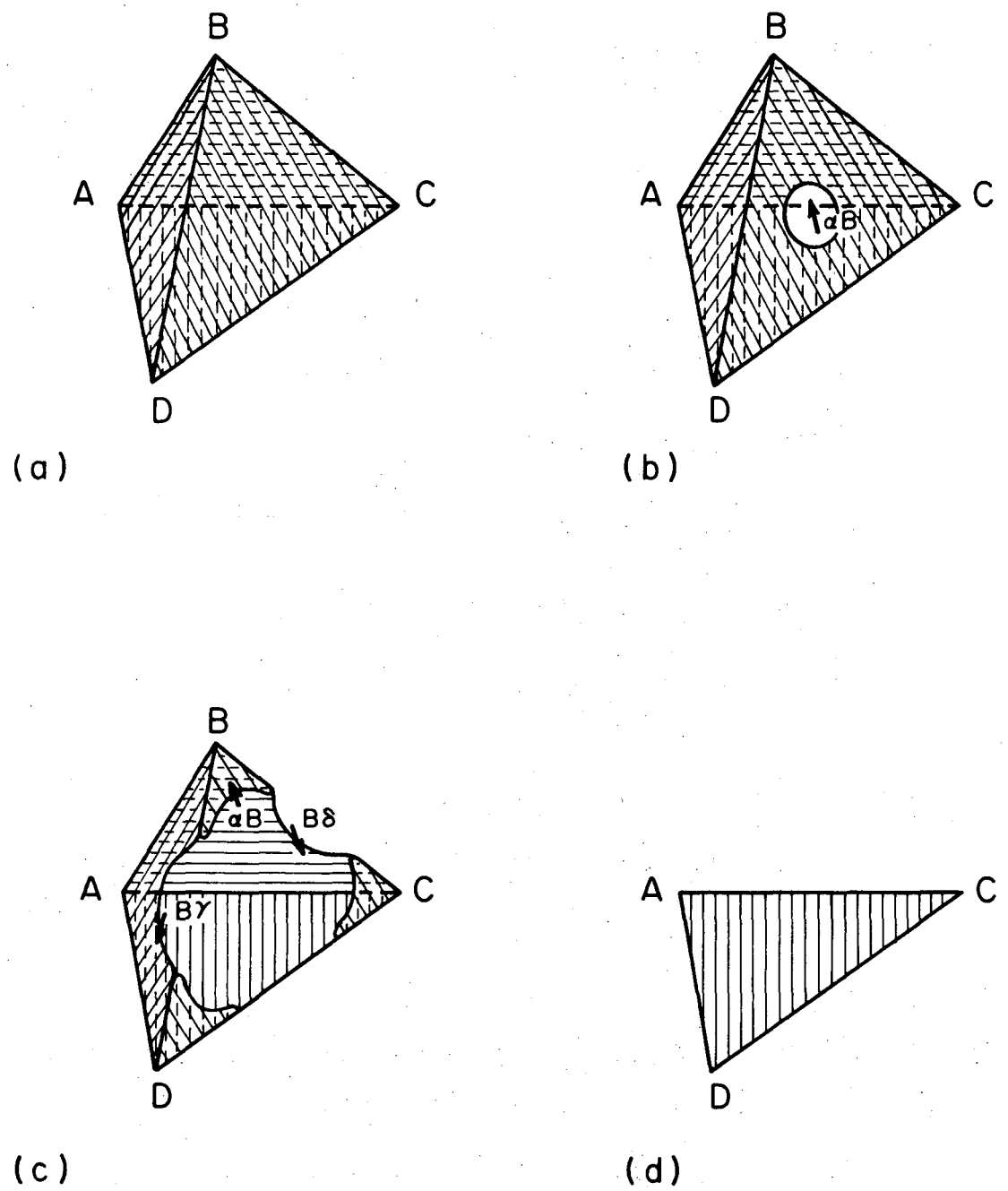

MUB-12804

Fig. 7 Dislocation reactions involved in the collapse of a SFT by nucleation of a Shockley partial in the face

loop E_f can be expressed by the approximate expression:

$$E_f = E_L(r \ln r) - E_{SF}(r^2) - W_\tau(r^2)$$

where

E_L = energy of the dislocation loop formed (proportional to $r \ln r$).

E_{SF} = energy of the stacking fault destroyed in the formation of the loop (proportional to r^2).

W_τ = work done by the external stress field, τ, as the dislocation loop expands. This stress can also be provided by a dislocation.

E_f has a maximum value at the critical radius r_c which must be supplied by a thermal fluctuation to nucleate a stable Shockley loop. This mechanism was first proposed by Meshii and Kauffman (1960) in order to explain the results of their annealing experiments. They obtained an experimental value of 4.7 eV for the activation energy of the annealing process which agreed well with their calculated value of 6.6 eV based on the above model.

The second mechanism involves the nucleation or dissociation of two Shockley partial dislocations from one of the stair rod dislocations. (Fig. 8) The activation energy for this mechanism has a form similar to the preceding case.

$$E_e = E_L - E_{SF} - W_\tau - E_{SR}(r)$$

where E_L, E_{SF} and W_τ have the same meanings as in the previous case.

E_{SR} = energy of the length of stair rod dislocation destroyed in the formation of the two Shockley partial dislocations.

If nucleation takes place in this manner, the value of the activation energy, E^*, for collapse should be slightly smaller than the preceding

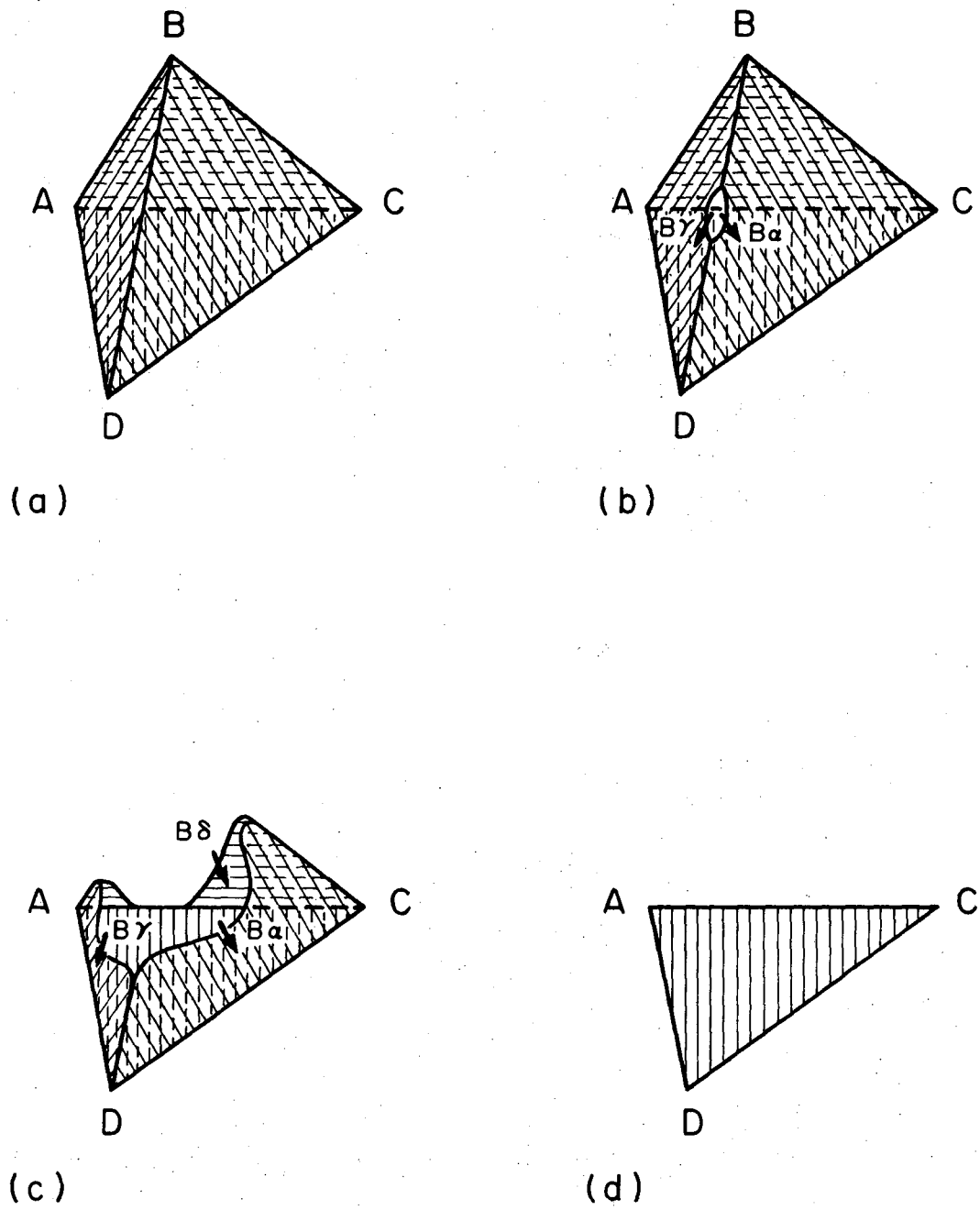

MUB-12805

Fig. 8 Dislocation reactions involved in the collapse of a SFT by nucleation of a pair of Shockley partials in the edge

case, because of the length of stair rod dislocation that is destroyed. However, the number of sites where the process can occur is very much smaller. For face nucleation, the number of sites available for the nucleation of a Shockley partial dislocation loop is proportional to ℓ^2 where ℓ is the edge length of the tetrahedron. For edge or stair rod nucleation, the number of sites is proportional to ℓ.

The third possible mechanism involves the nucleation or dissociation of three Shockley partial dislocations from a corner of the tetrahedron where three stair rod dislocations meet. The expression for the activation energy, E_c, based on this model has the same form as case II discussed above. The activation energy for this mechanism is expected to be slightly lower than either of the preceding mechanisms but, the number of nucleation sites is only 4, the corners of the tetrahedron. (Fig. 9)

The increased stability of tetrahedra cut by the foil surface is understandable when viewed in the light of the mechanisms for collapse proposed. For example in the corner collapse mechanism, the corners are the active sites for nucleation of the Shockley partials. In the case of the truncated tetrahedron 13 of Fig. 4, two corners remain of the original 4 reducing the possible nucleation sties by one-half. The total stair rod length is also reduced but by less than one-half while total stacking fault area is reduced by less than one-third. Therefore any of the three proposed mechanisms can be used to explain why a truncated tetrahedron should be more stable than the complete one of the same edge length even though stair rod segments in the tetrahedron are removed which should make nucleation easier.

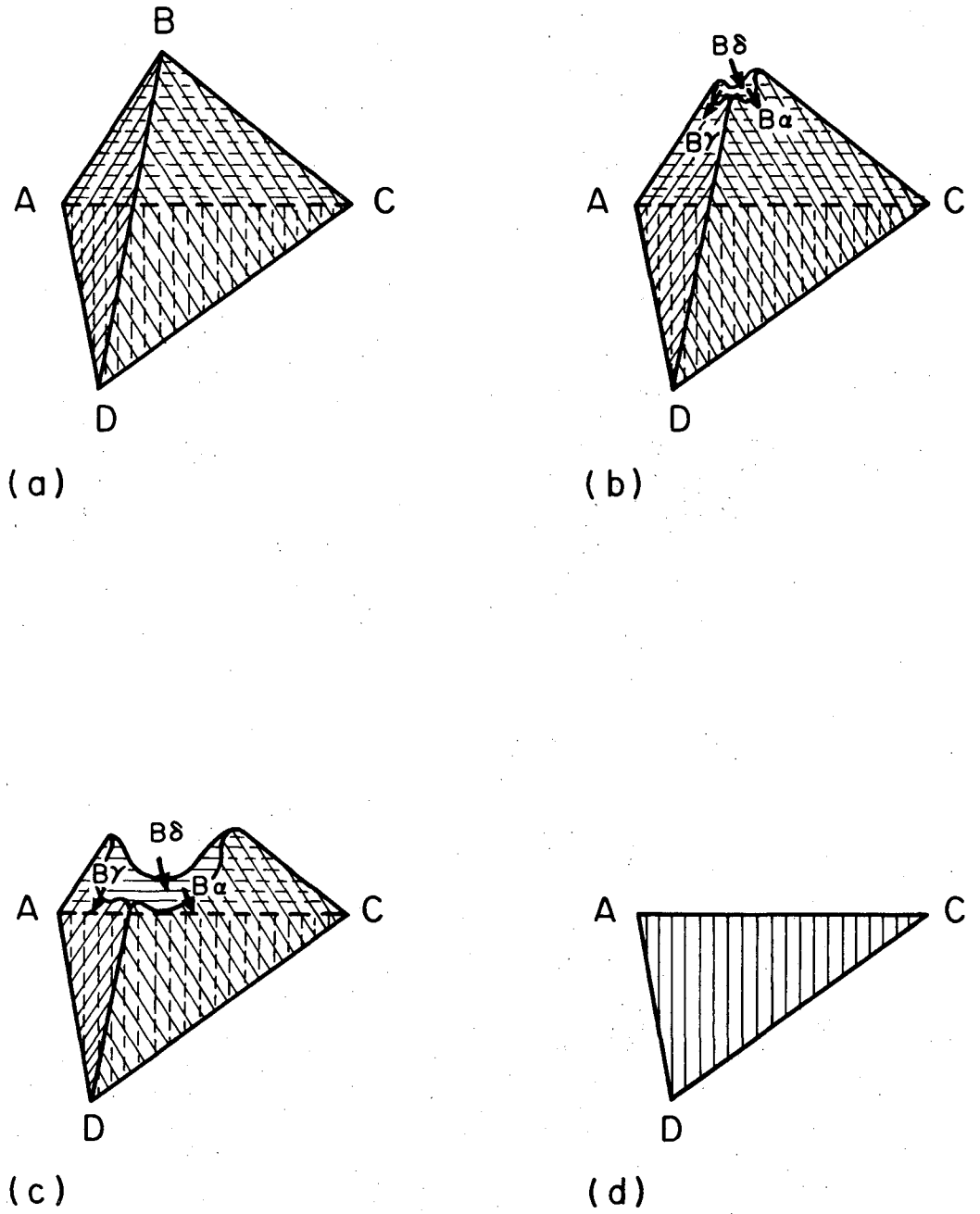

MUB-12806

Fig. 9

The measured activation energy in a macroscopic annealing experiment may well be influenced by all three mechanisms and must be related by the expression

$$k = A_c e^{-E_c^*/kT} + A_e e^{-E_e^*/kT} + A_f e^{-E_f^*/kT}$$

The dominance of any particular mechanism would be dependent on the pre-exponential term, A, as well as the activation energy E^*. Because

$$A_c \ll A_e \ll A_f$$

and

$$E_c < E_e < E_f$$

it is conceivable that each of the three mechanisms could dominate over a particular temperature range.

The activation energy for the corner collapse mechanism has been calculated by Jøssang and Hirth (1966) and Humble et al. (1966) taking into account the interaction terms of the neighboring stair rod dislocations. The truncated configuration of the stacking fault tetrahedron as it collapses to a Frank sessile loop is approximated by straight lines as shown in Fig. 10. An energy maxima occurs if the energy of the truncated tetrahedron is plotted vs the height, h, of the plane of the Shockley partials above the base of the tetrahedron. This maxima is shown to vary with the size, ℓ, of the SFT. (Fig. 11) Using a stacking fault energy value of 55 ergs/cm^2 for Au Jøssang and Hirth (1966) have determined a value of 31 eV for the activation energy at the critical edge length, ℓ_c= 265Å. The high value of E^* can be reduced somewhat if the

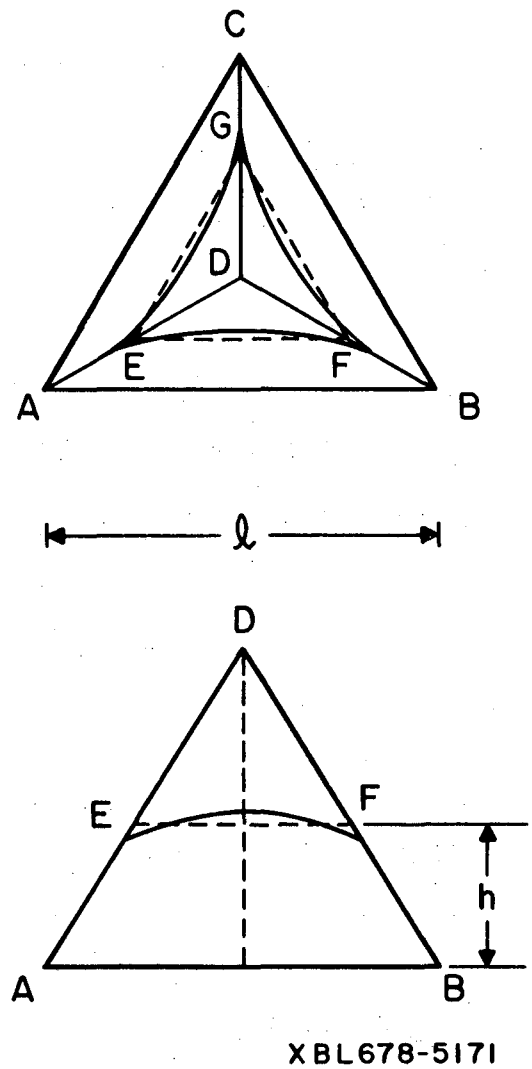

Fig. 10 The idealized configuration of a truncated tetrahedron used by Jøssang and Hirth (1966) to calculate barrier energies for collapse from a corner

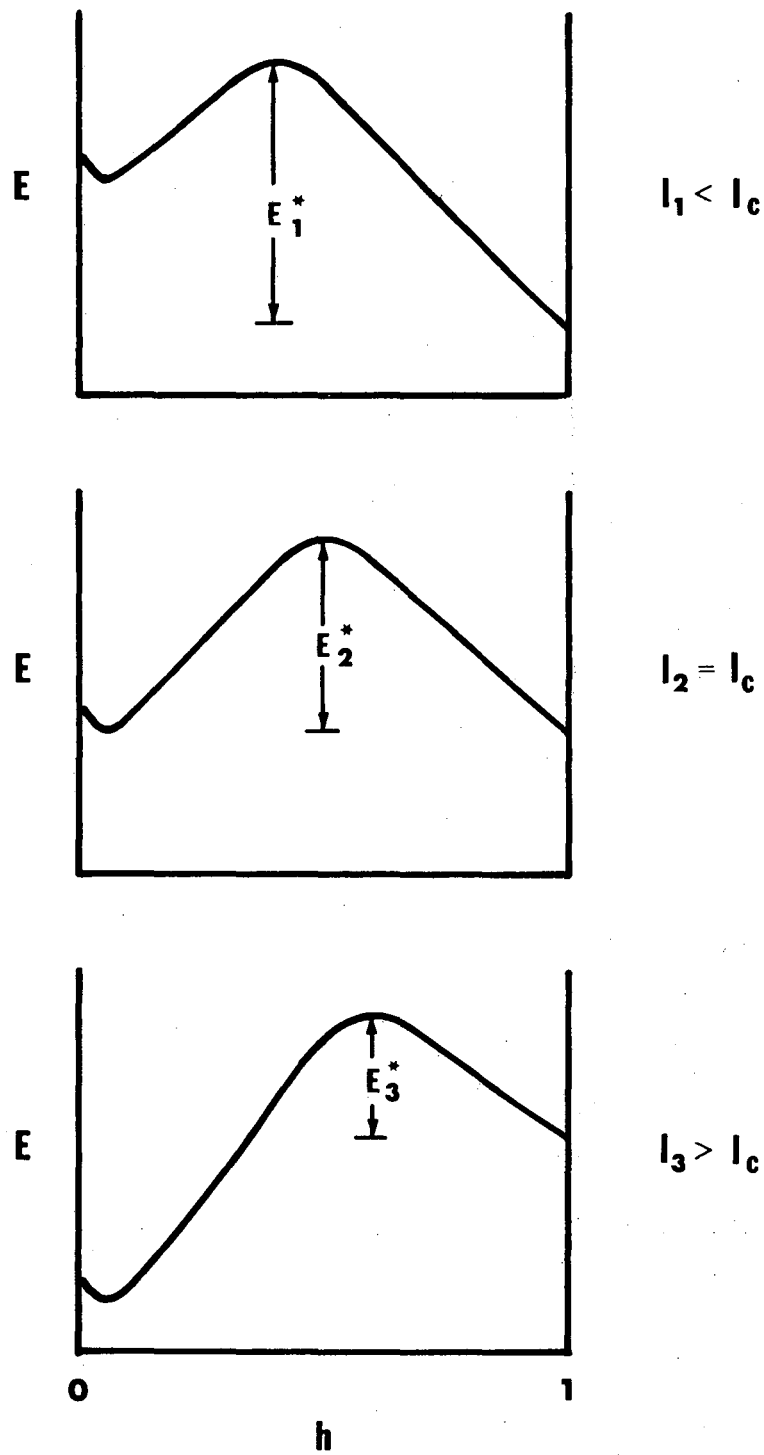

XBL 686-1127

Fig. 11 Energy of the truncated tetrahedron as the Shockley partials extend from h = 0 (FSL) to h = 1 (SFT)

correct curvature of the Shockley is introduced into the calculations but certainly not enough to make the value approach one which would allow collapse to occur with the high frequency observed. A stacking fault energy of 55 ergs/cm^2 belongs at the upper end of values suggested for the stacking fault energy of gold. Use of a lower stacking fault energy in the calculations would increase the activation energy for a given tetrahedron edge length. Local stresses can reduce somewhat the activation energy for collapsed but here again the calculations of Hirth (1963) show that nucleation can occur at appreciable rates only for stress levels approaching G/30.

The effect of impurities can conceivably cause a reduction in the activation energy for nucleation of the Shockley partials. In the present case, the bulk specimens were found to absorb during the quenching and annealing treatments an additional 0.002% by wt. oxygen. This oxygen could have combined with the Cu and Ag impurities of the originally 99.999% gold and acted as the nuclei for growth of many of the stacking fault tetrahedra finally formed. In fact, the maximum possible concentration of impurity-oxygen or impurity-vacancy complexes is equal to the concentration of stacking fault tetrahedra produced in our experiments. If impurities are concentrated at the corners of the tetrahedron one can picture them as preventing the stair rods from completely forming at the corners. This would reduce slightly the required activation energy needed for collapse. However such an effect alone would not be enough to reduce E^* by a factor of 10. Jøssang's calculations also show that the energy maximum, Fig. 11, for a 300Å tetrahedron occurs at $h \cong 1/2$.

There is reason to believe, as will be discussed in the next section, that the impurities present would tend to cluster instead along the stair rods of the tetrahedron which would make collapse more difficult. That is, impurities should increase not decrease the barrier energy for collapse.

This discussion of the differences in the observed behavior of the annealing of stacking fault tetrahedra with that predicted by calculations will be continued in Section C where it will be considered together with the results of macroscopic annealing tests.

B. Annealing of Stacking Fault Loops

1. Annealing Behavior of Hexagonal Stacking Fault Loops

Figure 12 shows several stages in the annealing of a nonregular hexagonal stacking fault loop in gold. Note that the loop corners appear to remain angular during shrinkage and do not round as hexagonal loops do in aluminum (Tartour 1966). This nonrounding of loops in gold makes measurement of its shrinkage rate more complicated than the case for aluminum, since a single parameter such as the loop radius cannot be used to describe the shrinkage process. Consequently other means of describing the shrinkage process had to be sought. In an initial study, various rates of shrinkage were calculated based principally on measurements of changes in the area and circumference of the loop with time. This approach led, however, to the conclusion stated earlier in Section B that the shrinkage behavior for loops in gold was extremely erratic making systematic study of the shrinkage process appear impossible.

From further and more detailed inspection of the shrinkage process, a method was devised where the degree of shrinkage of each side of the loop could be measured independently. Such a measurement requires three fixed reference points in the vicinity of the loop being studied which would then fix both its exact position and plane within the foil. In the present study small stacking fault tetrahedra served as the required reference points. By carefully superimposing each successive annealing stage of the loop, the amount each side of the loop shrank could be accurately determined. Utilizing the above procedure the shrinkage behavior of the loop of Fig. 12 was determined. The (111) projections of the successive stages of the loop are shown in Fig. 13a. The shrinkage

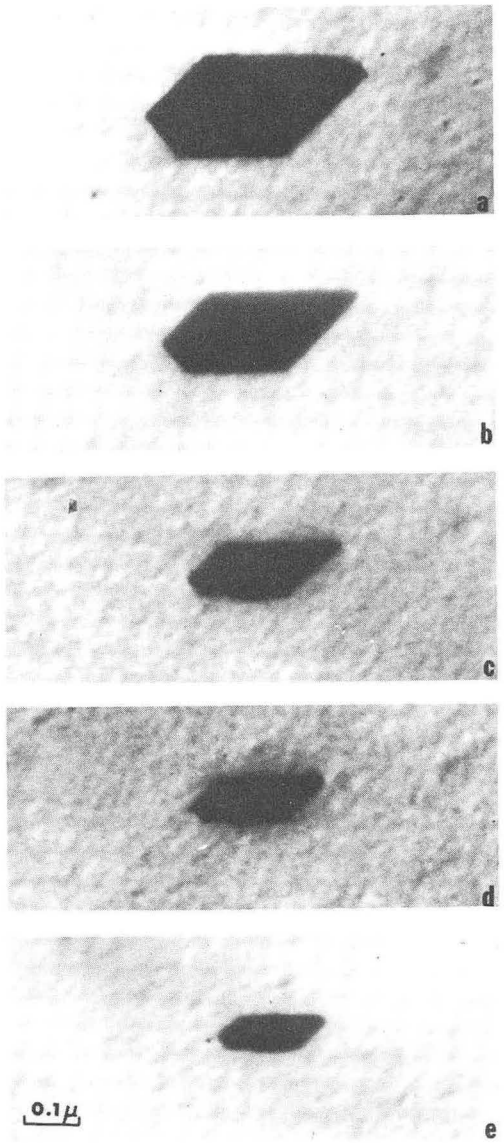

XBB 6711-6570

Fig. 12 Shrinkage of a non-regular hexagonal stacking fault loop.

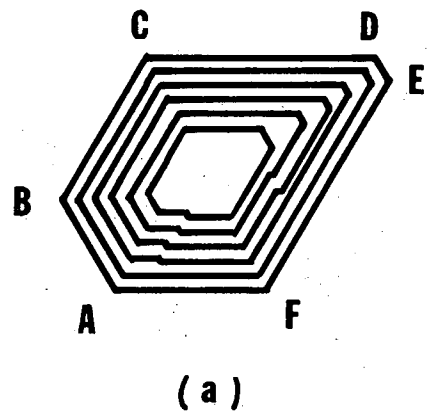

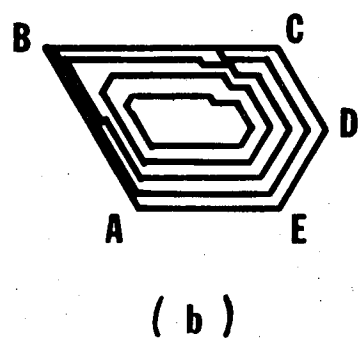

XBL 686-1124

Fig. 13 (a) (111) projection of the loop of Fig. 12.
(b) (111) projection of the loop of Fig. 20.

behavior of several sides of the loop is plotted and shown in Fig. 14. Note that shrinkage is linear and independent of the size of the loop. This independence of size on the shrinkage rate appears to hold as long as the loop remains angular. Furthermore, the position of each side with regard to the foil surfaces seemed not to influence its shrinkage rates. Sides AF and CD were closest and parallel to the surfaces of the thin foil specimen. This behavior is contrary to that observed in aluminum where Dobson et al. (1967) found that both the size of the loop and its position in relation to vacancy sinks effect the shrinkage behavior.

2. Annealing Behavior of Triangular Stacking Fault Loops

Compare now the annealing behavior of the heagonal loop of Fig. 12 bounded by 120° corners with the triangular stacking fault loop of Fig. 15. Given similar annealing treatments the shrinkage of the triangular loop is negligible when compared to the hexagonal loop. Numerous similar observations of this kind over a wide time and temperature range lead one to the conclusion that the shrinkage behavior of stacking fault loops bounded by 60° corners is quite different from those bounded by 120° corners. Such behavior would of course not be expected in a stacking fault loop bounded by a $\frac{1}{3}\langle 111\rangle$ Frank dislocation. However, for low stacking fault energy materials such as gold, the $\frac{1}{3}\langle 111\rangle$ Frank dislocation can dissociate into a $\frac{1}{6}\langle 110\rangle$ stair rod and a $\frac{1}{6}\langle 112\rangle$ Shockley partial dislocation, thereby lowering the total energy of the loop. If stacking fault loops in gold are extended, the triangular and hexagonal stacking fault loops should have the configuration of Fig. 16b. Note the difference in the nature

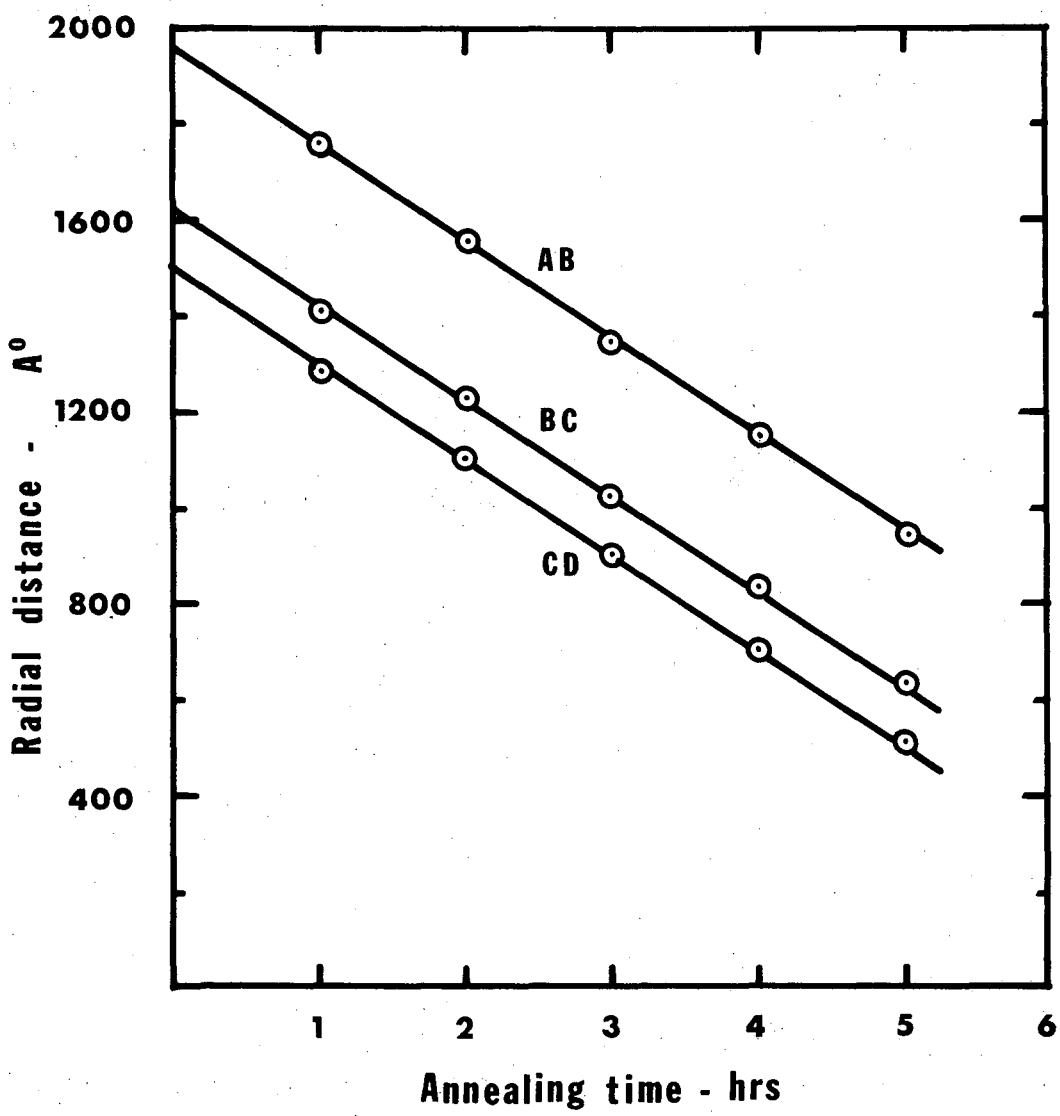

XBL 686-1122

Fig. 14 Shrinkage behavior of three sides of the loop of Fig. 12.

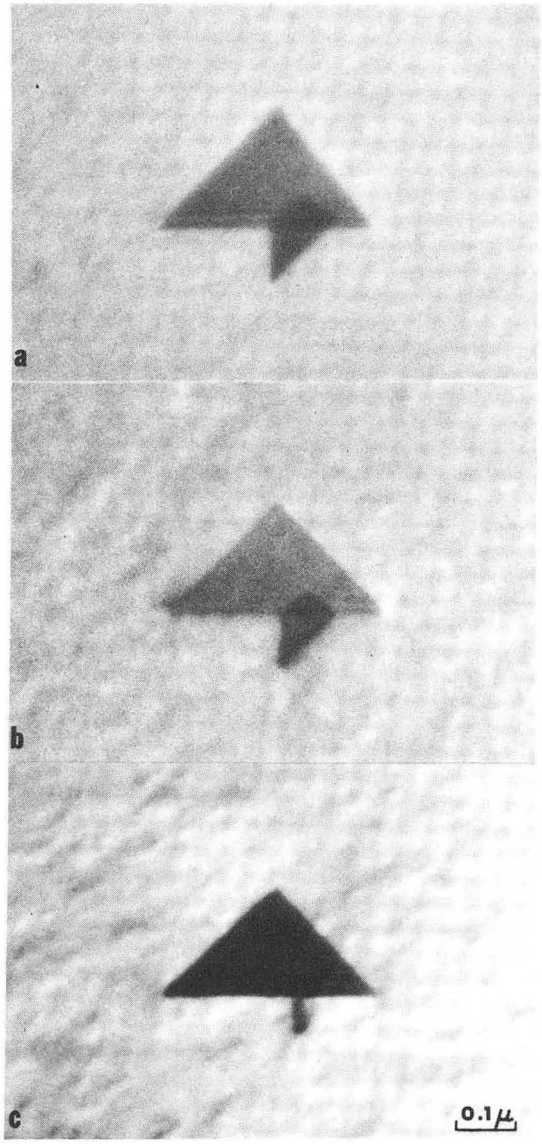

XBB 6711-6567

Fig. 15 Shrinkage behavior of a triangular stacking fault loop.

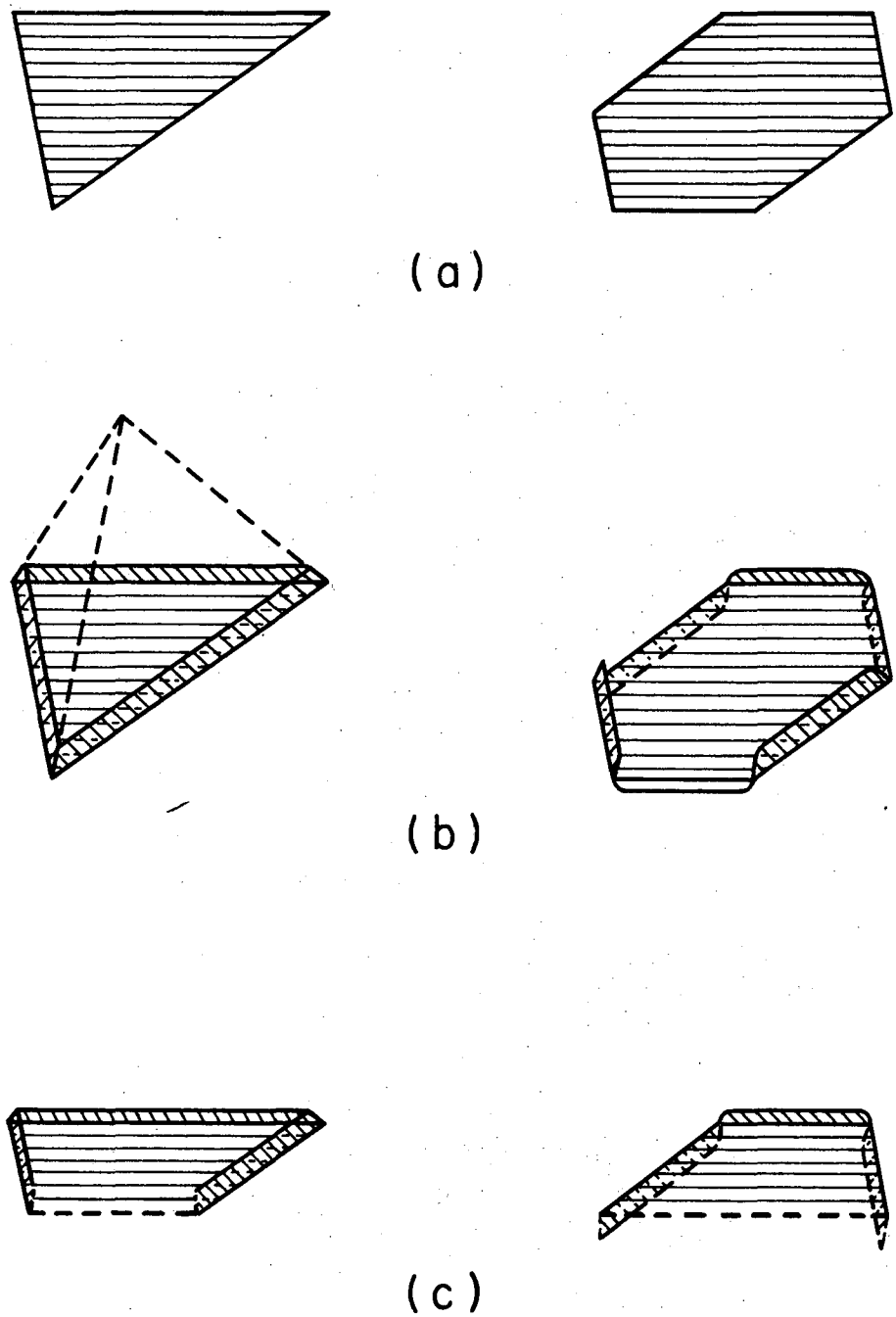

XBL678-5176

Fig. 16 Configurations of a) 1/3⟨111⟩ type stacking fault loops b) extended stacking fault loops, c) extended loops cut by the foil surface

of the 60° and 120° corners. At the 60° corner the two Shockley partials are on the same side of the plane of the loop; the corner is closed by a $\frac{1}{6}\langle 110\rangle$ type stair rod making it extremely stable. At the 120° corner the Shockley partials are on opposite sides of the loop plane which results in a constriction that requires a lower barrier energy to form jogs.

3. Annealing Behavior of Loops Cut by the Foil Surface

If stacking fault loops in gold are extended it would explain the unexpected annealing behavior of the triangular loop 1 of Fig. 17 which has been intersected by the foil surface. For an unextended loop one would expect the surface to increase the shrinkage rate assuming the process was diffusion controlled. The intersected loop on the contrary is made more stable by its intersection with the foil surface. One can see why this is so when the configuration of the loop is examined along the truncated side as shown schematically in Fig. 16c. Such corners make nucleation of the required jogs for climb very difficult. If in fact jogs are created at the corners of the loop, as will be discussed in a later section, the truncated loop of Fig. 17 would be more stable than the triangular loop of Fig. 14 since there is one less corner at which jogs can be nucleated.

Note also the super jogs formed during annealing on the lower loop of Fig. 17. The stabilization of such superjogs might occur from the presence of impurity clusters along the perimeter of the loop. Jogs formed at one corner can travel along the edge of the loop until it meets an impurity cluster. The superjog is created by many jogs piling up at this point.

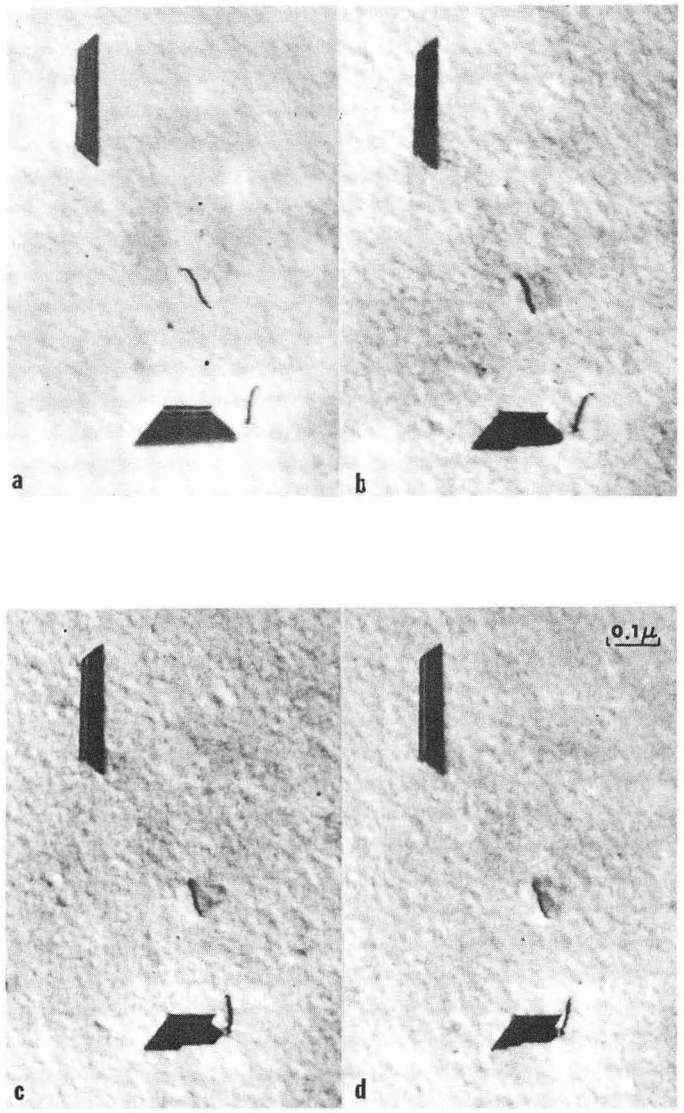

XBB 6711-6565

Fig. 17 Shrinkage behavior of loops cut by the foil surface.

4. Electron Diffraction Contrast from Extended Stacking Fault Loops

If stacking fault loops in gold are indeed extended, as one might conclude from the experimental evidence described in the preceding paragraphs, the loops should exhibit corresponding electron diffraction contrast effects. Loops in an ⟨001⟩ orientation which appear as triangles can be easily distinguished from the square appearing stacking fault tetrahedra as mentioned earlier. The diffraction contrast expected utilizing ⟨200⟩ type reflections are similar for both the extended as well as the unextended loop. Contrast can be expected from both the stacking fault in the form of fringes and the surrounding dislocation. When one of the ⟨220⟩ type reflections are used however, one-half of the $\frac{1}{3}$⟨111⟩ type loops will remain in contrast while the remaining loops should completely disappear. If the loops should however be extended, again one-half of the loops should remain in full contrast but instead of the remaining loops disappearing there should be contrast from two of the three sides of the loop. The differences in contrast effects expected are shown schematically in Fig. 18. Figure 19 shows the actual contrast from loops utilizing the [020] and [$\bar{2}$20] reflections. It should be pointed out here that a similar experiment for aluminum, which is thought to have a high stacking fault energy, i.e., 135 erg/cm^2 was performed by Tartour (unpublished) who showed similar but much more diffuse contrast. Possibly this contrast is due to the strains inherent in an edge dislocation. The contrast observed for gold can therefore be partly or wholly residual contrast. Yet the above contrast experiments together with the experimental observations of the preceding sections, i.e., the differences in the annealing behavior of triangular and

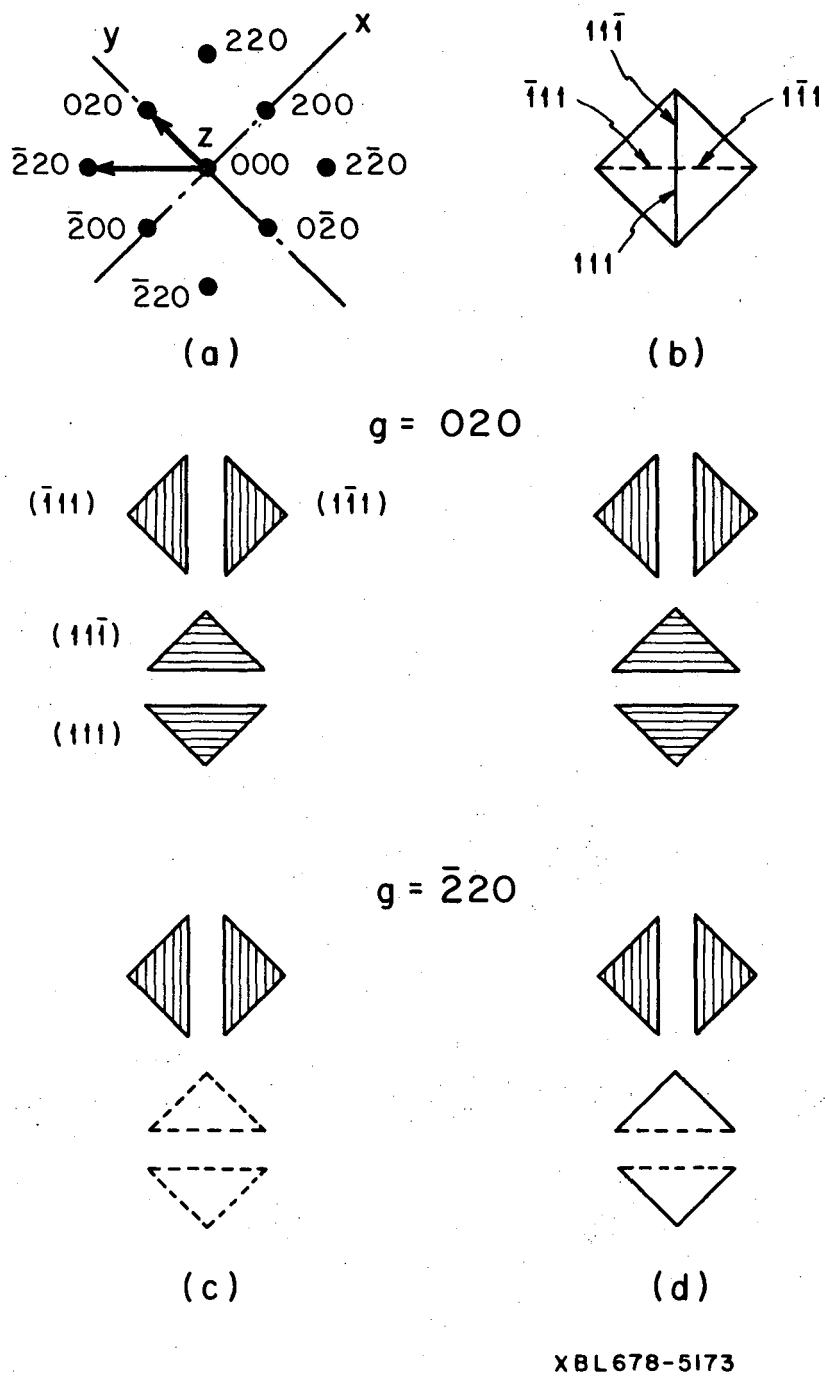

XBL678-5173

Fig. 18 Contract expected from c) unextended 1/3⟨111⟩ type loops and d) extended loops

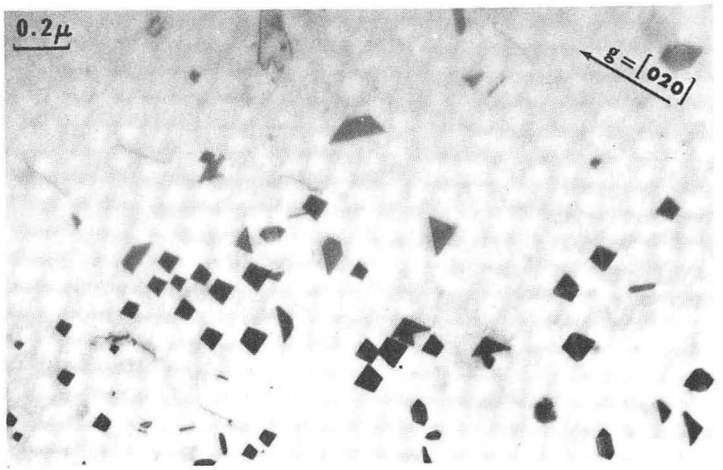

(a)

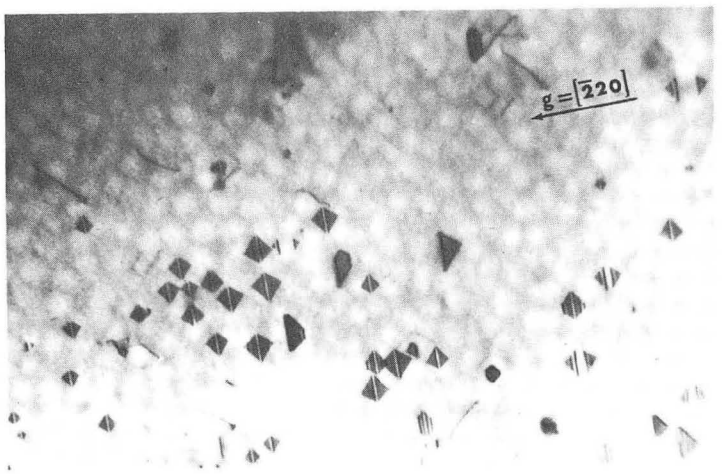

(b)

XBB 6711-6575

Fig. 19 Contrast changes observed when a) g = [020] b) g = [$\bar{2}$20].

hexagonal loops and the influence of the foil surface on the annealing of loops cut by it, suggests very strongly that stacking fault loops in gold are indeed extended. The following discussion will be based on this assumption.

5. Nucleation of Shrinkage from Loop Corners

Consider next the annealing of the loop of Fig. 20 which is bounded by both 120° and 60° corners. The shrinkage behavior of the loop was determined in the manner described earlier and is shown in Fig. 13b. Note that between the 0 and 2 hrs. annealing stages the loop sides CD, DE and EA which are each bounded by a pair of 120° corners have shrunk considerably more than sides AB and BC which are bounded by one 60° and one 120° corner. Notice also the movement of the 120° corner at C and the superjogs formed there during this period. These jogs could have formed only from the corner C, thus strongly suggesting that the shrinkage of side BC has occurred principally from the action of the 120° corner C toward B. The same can be said of the situation existing at corner A. These observations suggest, at least in the temperature range under study, i.e., 100-400°C, that it is the 120° corners which are responsible for the bulk of the shrinkage with the 60° corners contributing only little if any to the net shrinkage observed.

Consider now the annealing of the stacking fault tetrahedra and loops of Fig. 21. Note in particular the shrinkage behavior of loops 8 and 9 which are again shown schematically in Fig. 22. Shrinkage in each case appears to nucleate from one of the triangular loop corners. This observation appears at first to be in direct contradiction of conclusions

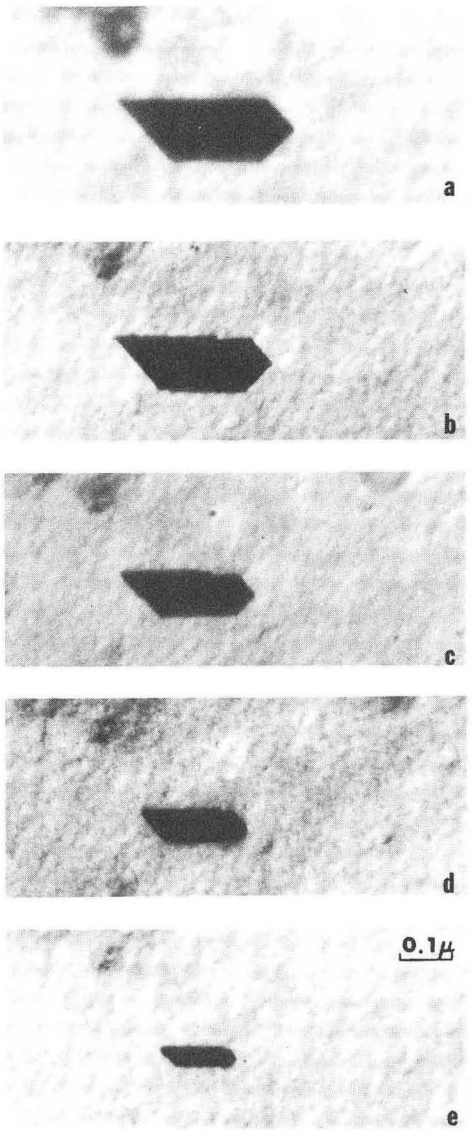

XBB 686-3941-A

Fig. 20 Shrinkage of a loop containing both 60° and 120° corners.

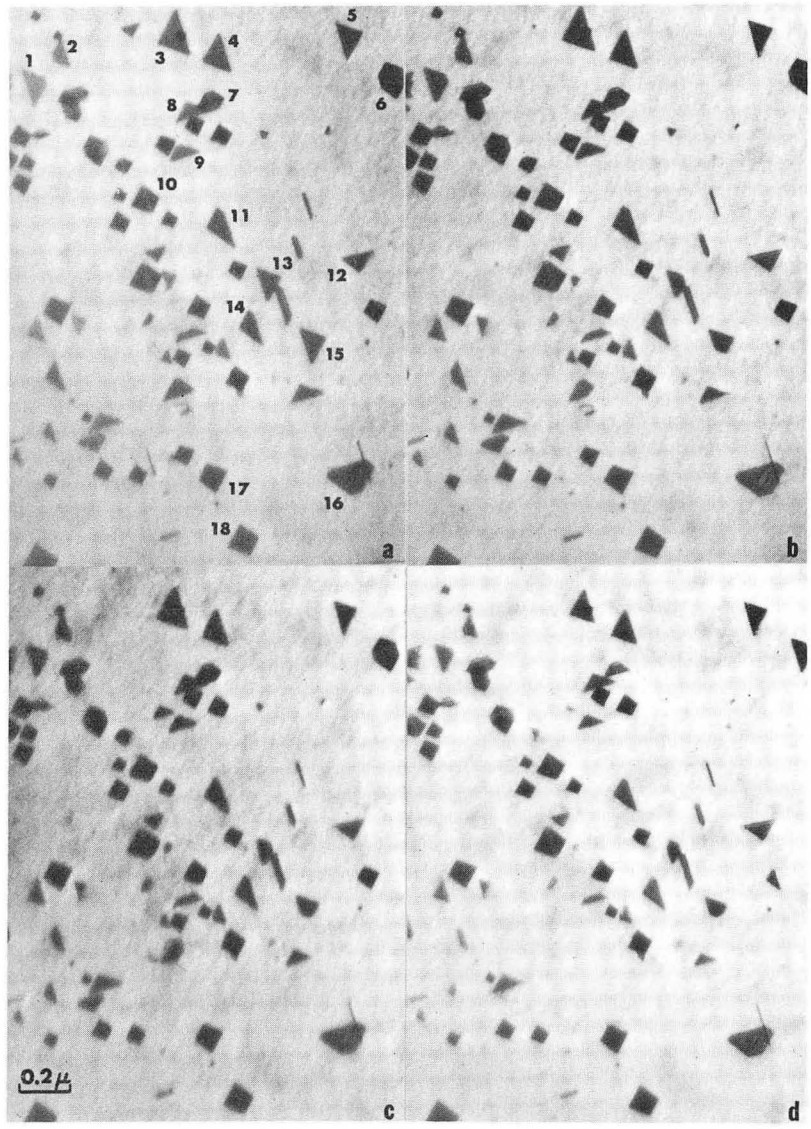

XBB 686-3939-A

Fig. 21 Behavior of loops annealed for a) 0, b) 1, c) 2, d) 3, e) 4, f) 6, g) 8, h) 10 hours at 300°C.

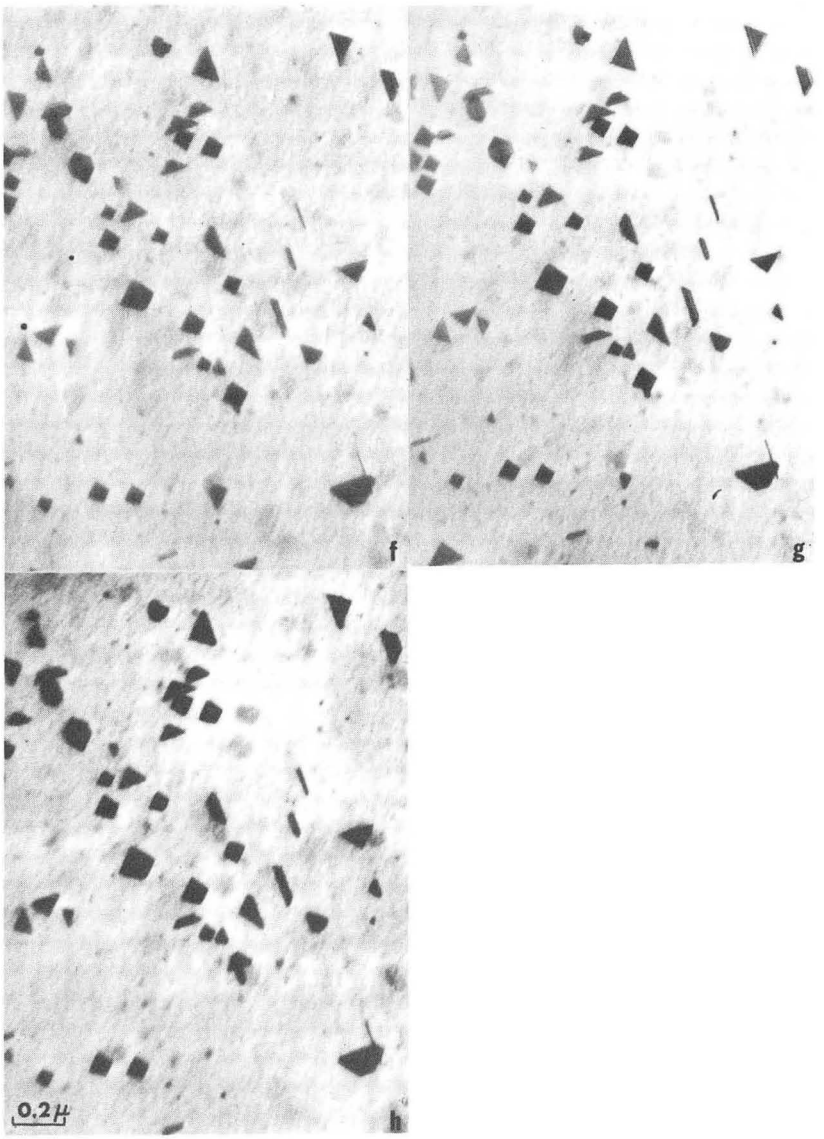

XBB 686-3940-A

Fig. 21 (continued)

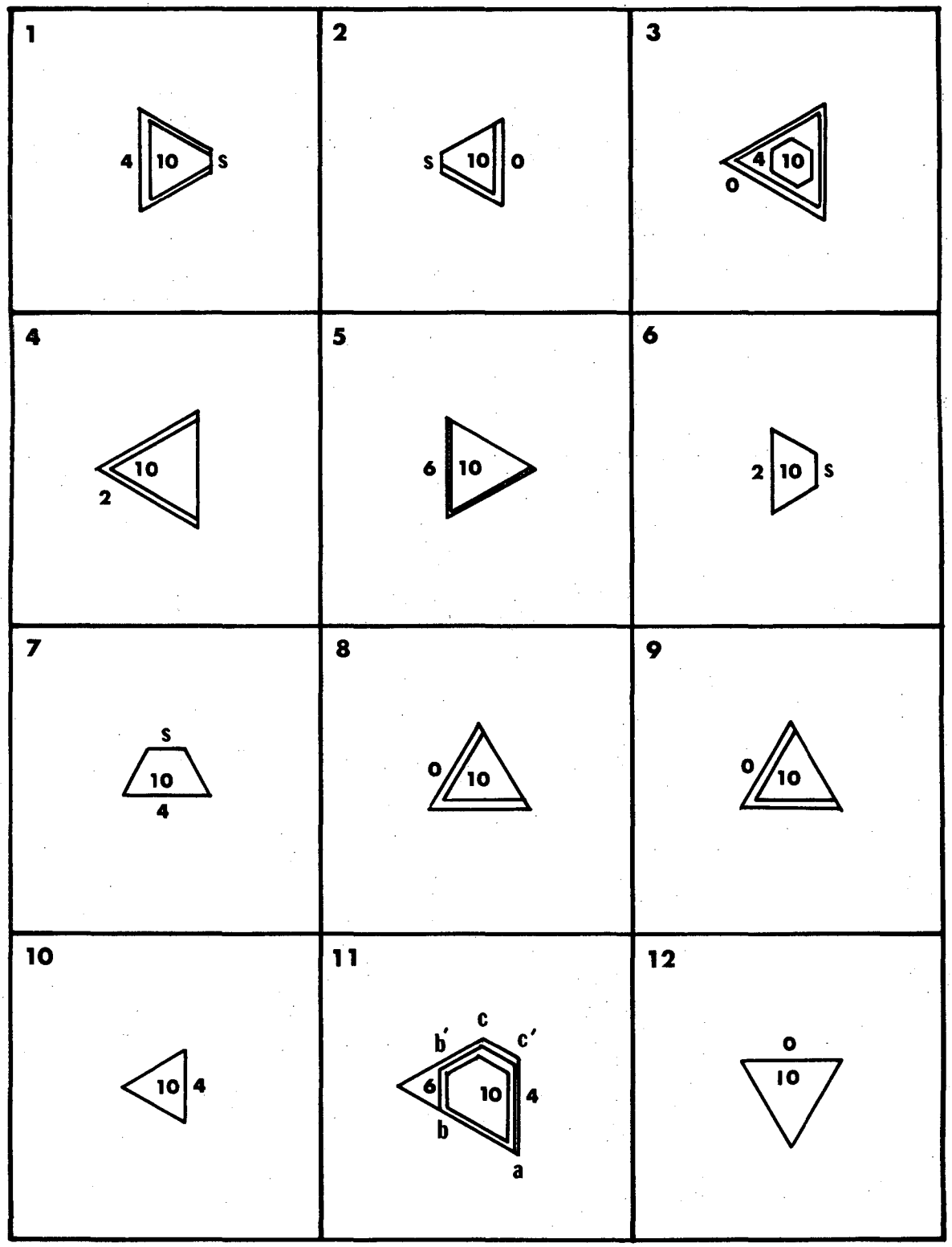

XBL 686-1126

Fig. 22 (111) projections of the loops of Fig. 20

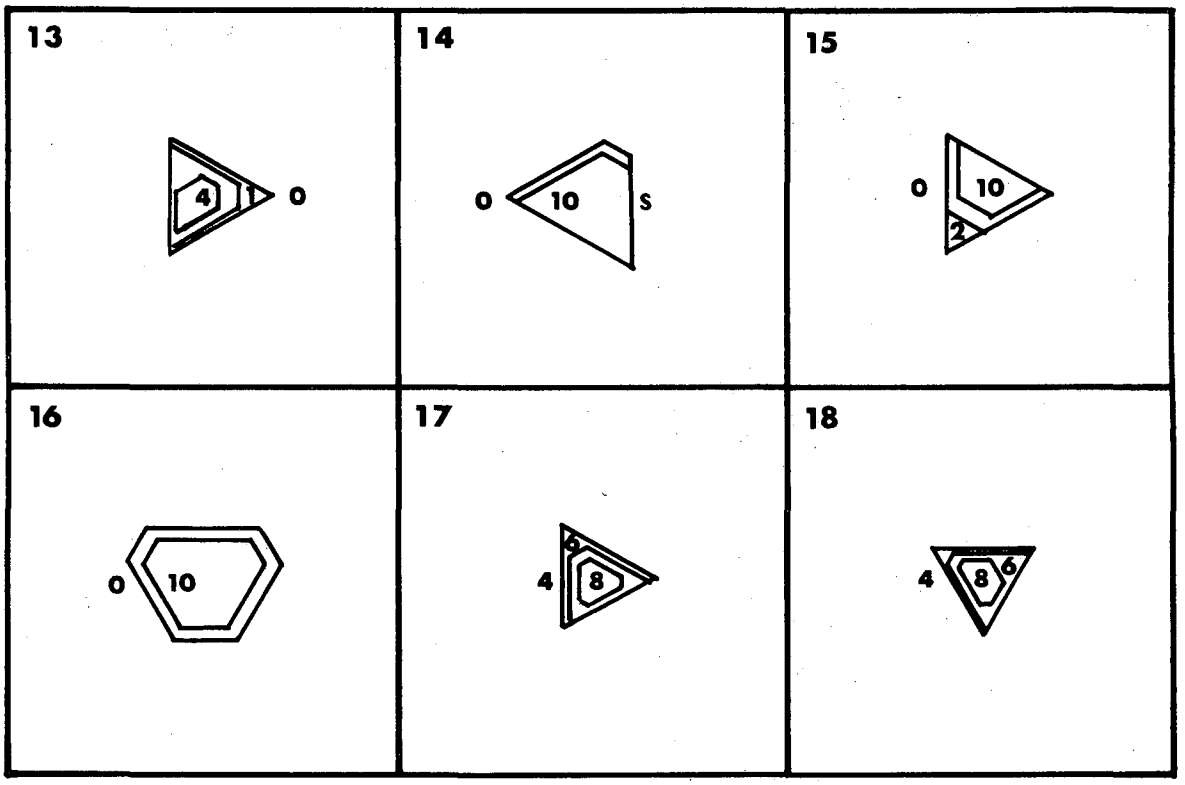

XBL 686-1125

Fig. 22 (continued)

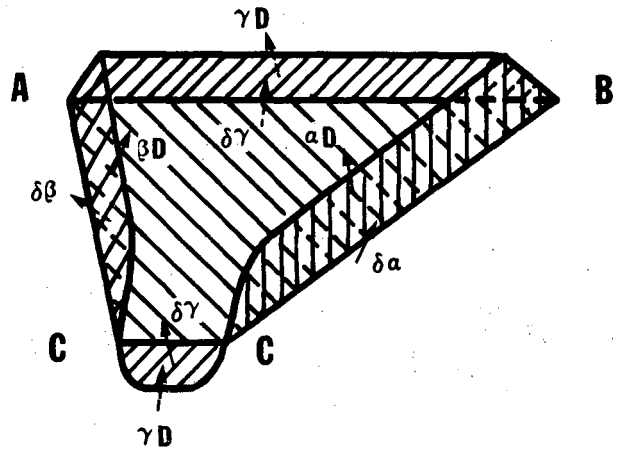

(a)

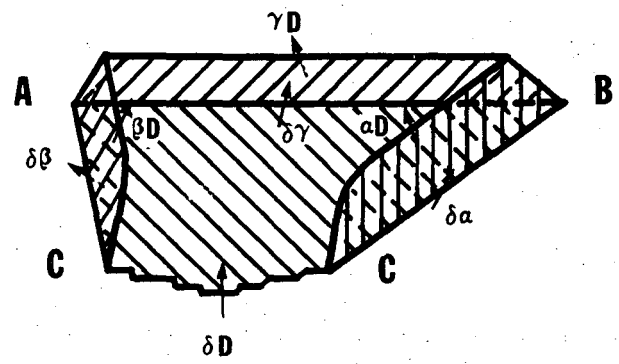

(b)

XBL 686-1123

Fig. 23 (a) Configuration of a pair of stable 120° corners formed from a 60° corner.
(b) Configuration of an unextended loop side bounded by 120° corners.

made earlier with regard to the shrinkage behavior of 60° and 120° bounded loops. However it is also observed that the shrinkage rates for the loop sides adjacent to the active corners are comparable to those observed, for example, from sides ab and ac' of loop 11 which are bounded by one 60° and one 120° corner, and approximately one-half the rate exhibited by the sides of the hexagonal loop 16, where each is bounded by 120° corners. If the active corners of loops 8 and 9 are pcitured not at 60° corners but instead as a pair of 120° hexagonal corners, spaced so close as to appear as a single corner in the electron micrograph, the above observation would again fit into our earlier speculations. That is, the active corners of loops 8 and 9 should be pictured as in Fig. 23a. This analysis would also explain the behavior of the triangular loop 12 which does not shrink at all during 10 hrs. of annealing, and the loops 4 and 5 which do not start to shrink until after 2 and 6 hrs. of annealing respectively. That is, appreciable shrinkage of loops can occur only after formation of stable hexagonal corners from the original 60° corners.

In the process of forming new 120° hexagonal corners on a corner of a triangular loop, the loop acquires a new side as well. If this new side is extended, shrinkage will occur for this side at the expected rates. There is also the possibility that the new side formed between the pair of hexagonal corners can be unextended. This can occur for example if a high concentration of jogs rapidly forms from each of the new corners. A high concentration of jogs is then produced along the new side and thus prevents its extension. This might be part of the explanation for the extremely high rates observed for the new sides

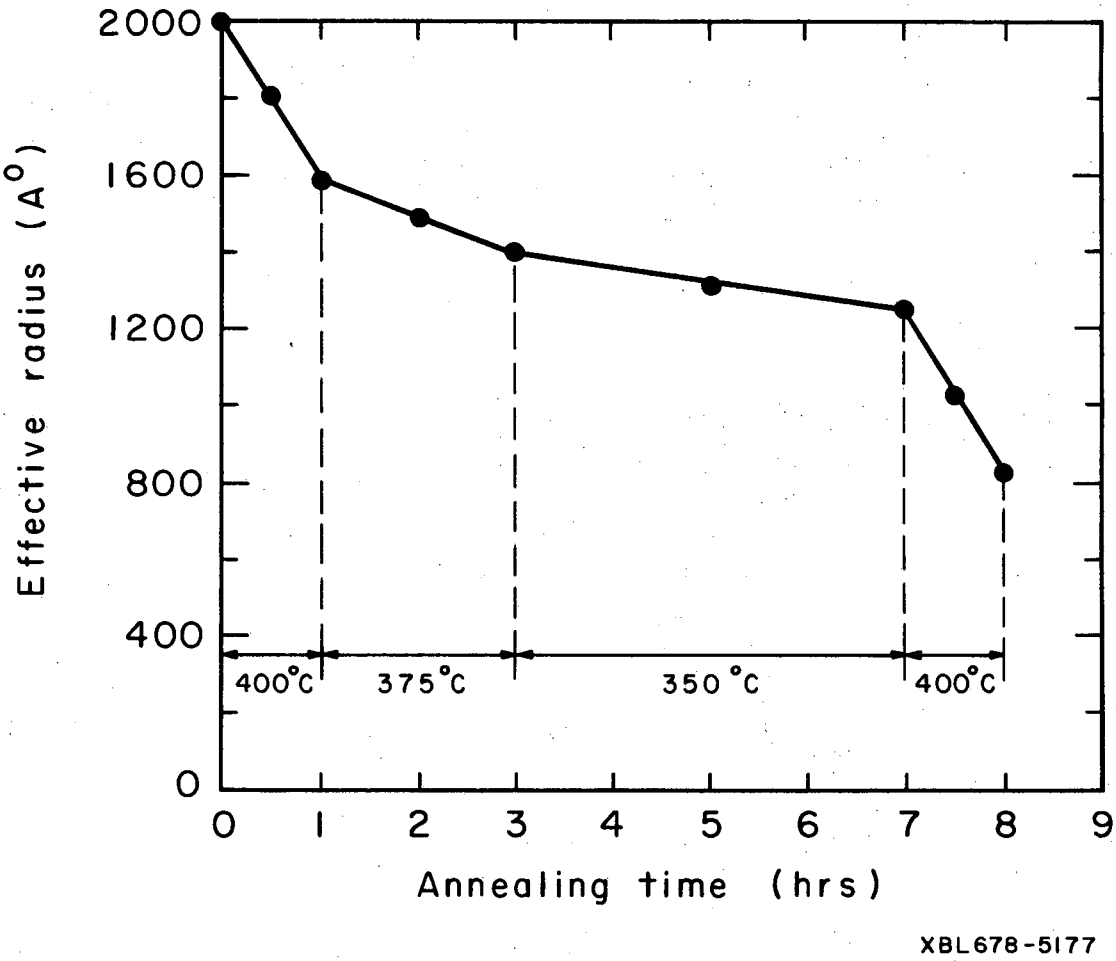

Fig. 24 Shrinkage behavior of a loop side bounded by hexagonal corners at several temperatures.

formed on loops 3 and 11. This new side should be pictured as in Fig. 23b. The force acting on such sides will consist of that due to the stacking fault plus that due to the line tension. The latter will be greatest per unit length for a short side.

6. Activation Energy for Shrinkage

If the shrinkage rate of the loop can be determined for two or more temperatures, an activation energy and a pre-exponential frequency factor can be calculated assuming a thermal activation model for the annealing process. Instead of determining the shrinkage rates for the various temperatures on different loops in the usual way, the annealing rates were determined in the present study on a single loop by the slope intersection method commonly used in resistivity studies. In this method, abrupt changes in the temperature are made during the course of annealing and the shrinkage rates for the two temperatures determined and compared at the intersection where the state of the loop is unchanged except for the expected thermal dependent effects. The technique eliminates the need to know the exact details of the loop's jog distribution and configuration during the annealing process with only changes which are temperature dependent being measured. The curve of Fig. 24 was obtained in this way utilizing three temperatures. Because of the linear behavior of the shrinkage of the loops as shown in Fig. 14, the entire annealing time at each temperature was used to determine the rates. The method also allows a check on any magnification errors between the different annealing segments of the annealing curve, something that could not have been done if the required annealing rates were determined from different loops. The coincidence of the slope of the annealing curve at 400°C

for the beginning and end segments of the annealing curve gives further validity to this technique. The logarithm of the rates determined from the slopes of the three temperatures are next plotted against the reciprocal of the absolute temperature in Fig. 25. The slope of the curve determines the apparent activation energy for shrinkage and the intercept, the pre-exponential frequency factor. The value determined for the activation energy and frequency factor are 1.9 eV and 2×10^{16} Å/hr, respectively. These values correspond to the annealing behavior of loops bounded by 120° corners.

These generalizations can be made of the annealing behavior of stacking fault loops in gold:

i. Stacking fault loops in gold remain angular during shrinkage and do not round as do hexagonal stacking fault loops in aluminum.

ii. The shrinkage rate of the loop is independent of its size as long as the loop remains angular.

iii. The rate of shrinkage of loops whose sides are bounded by 60° corners is much less than from sides bound by 120° corners in the temperature range investigated.

iv. The surface does not appear to effect the rate of shrinkage. Sides formed by interaction of the loop with the surface are very stable.

v. Diffraction contract from the loops as well as the shrinkage behavior of points i-iv suggest that the stacking fault loop in gold is extended.

vi. The loop corners, 60° or 120°, appear to be the active centers for shrinkage.

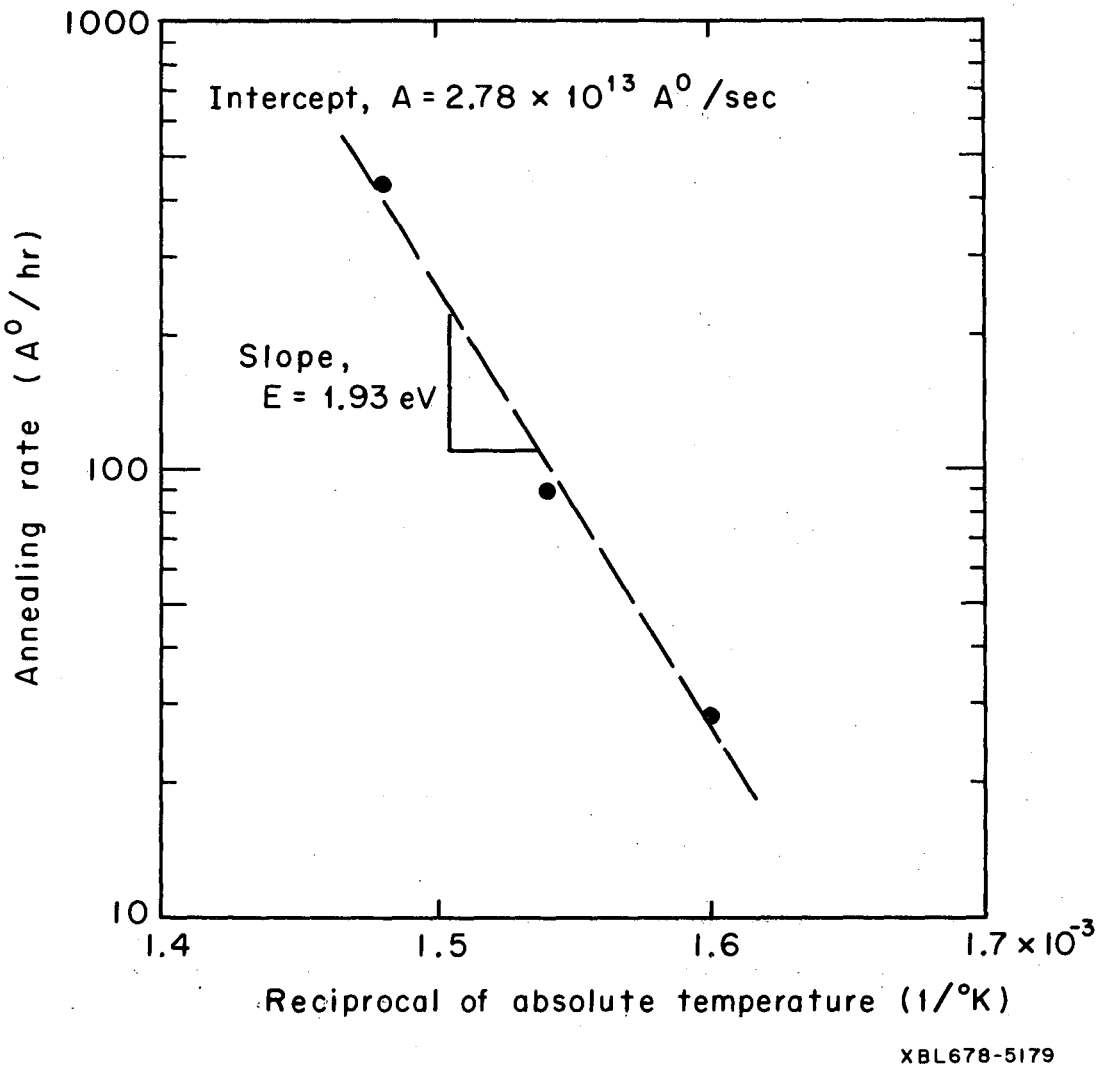

Fig. 25 Arrhenium plot of annealing rates determined from Fig. 24.

vii. The stacking fault loop in gold with sides bounded by 120° corners shrink with an activation energy of 1.9 eV and pre-exponential frequency factor of 2×10^{16} Å/hr.

We will next examine the mechanism of jog nucleation in extended stacking fault loops.

Table I. Rates of shrinkage of the loops of Fig. 21.

Loop No.	R_1(Å/hr)	R_2(Å/hr)	R_c(Å/hr)
1	14	23	
2	14		
3	12	24	190
		23	250
			250
4	13		
5	15		
6	--	--	
7	--	--	
8	13		
9	13		
10	--	--	
11	11	22	300
	10	30	330
12	--	--	
13	35	53	
14	14	--	
15	15	29	
16		19	
17		60	200
18		50	300

7. Nucleation of Jogs in Extended Stacking Fault Loops

Rounding, as it occurs in hexagonal stacking fault loops in aluminum, requires that the rate of jog nucleation from the 120° corners be roughly equal to or even greater than the rate at which jogs move.

$$k_{jN} \gtrsim k_{jM} \text{ rounding}$$

This requirement for rounding is schematically illustrated in Fig. 26a which shows that a third jog "3" must be nucleated from the corner A before jogs 1 and 2 meet and annihilate one another somewhere at point y. If the rate of jog nucleation should be such that jog 3 is nucleated after jogs 1 and 2 have already annihilated one another, the shape of the loop remains angular. That is, if the rate of jog nucleation is much less than that of jog motion the loop will remain hexagonal

$$k_{jN} < k_{jM} \text{ angular}$$

Figure 26b shows the jog distribution required in a round stacking fault loop as formed in aluminum. Note that jogs of a single or multiple atomic length can produce similar rounding. The electron microscope however is unable to resolve such features.

An idealized model of the process of jog nucleation and motion can be constructed by assuming the hard sphere nearest neighbor model approximation for the arrangement of atoms in and around the stacking fault loop. This is done in Fig. 27 which shows the loop in the (111) orientation. The stacking fault loop lies in the atomic plane b. The atomic layers above and below are designated a and c respecitvely. Nucleation

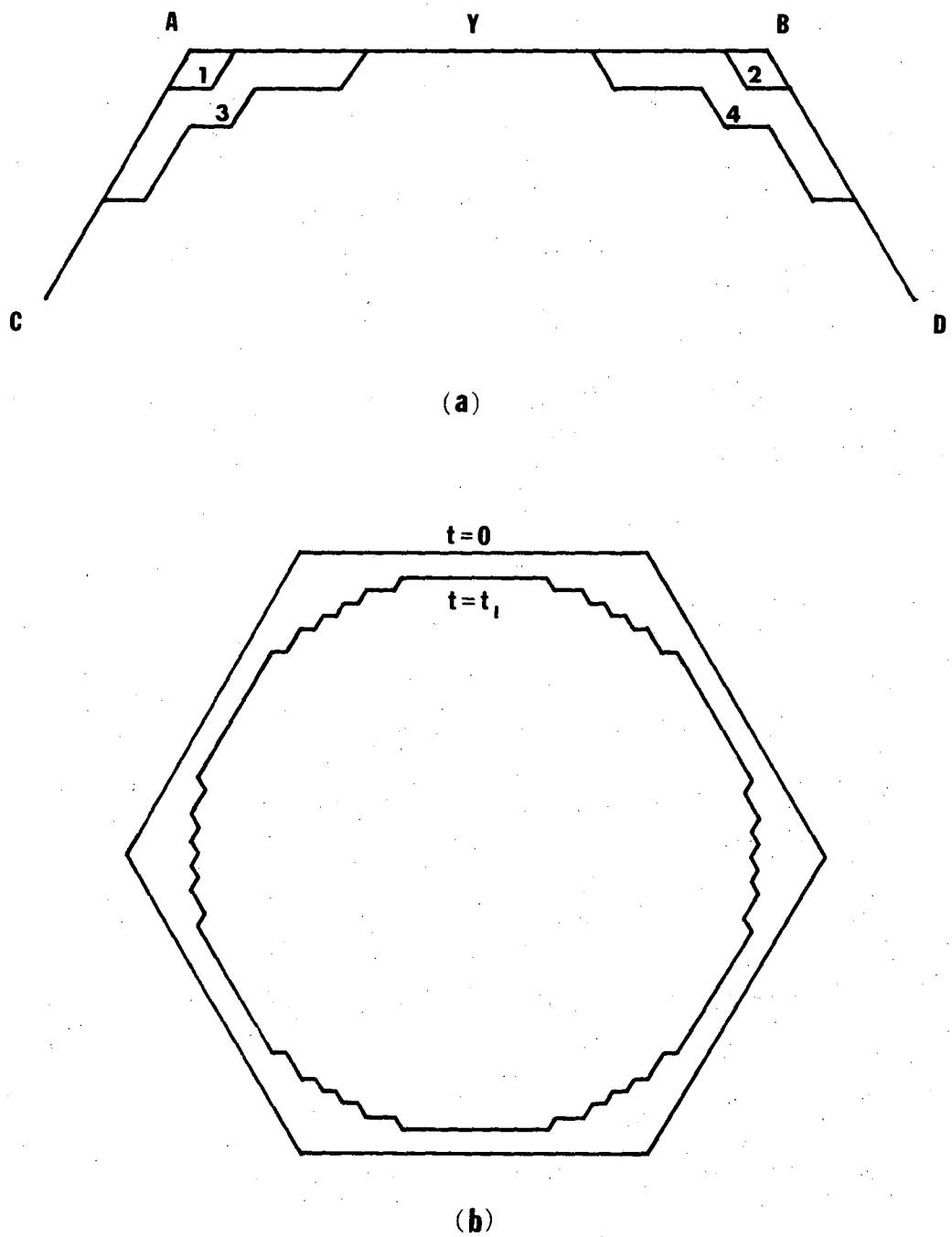

XBL 6711-6099

Fig. 26 (a) Process of rounding in a hexagonal stacking fault loop in aluminum

(b) Jog distribution along a rounded loop

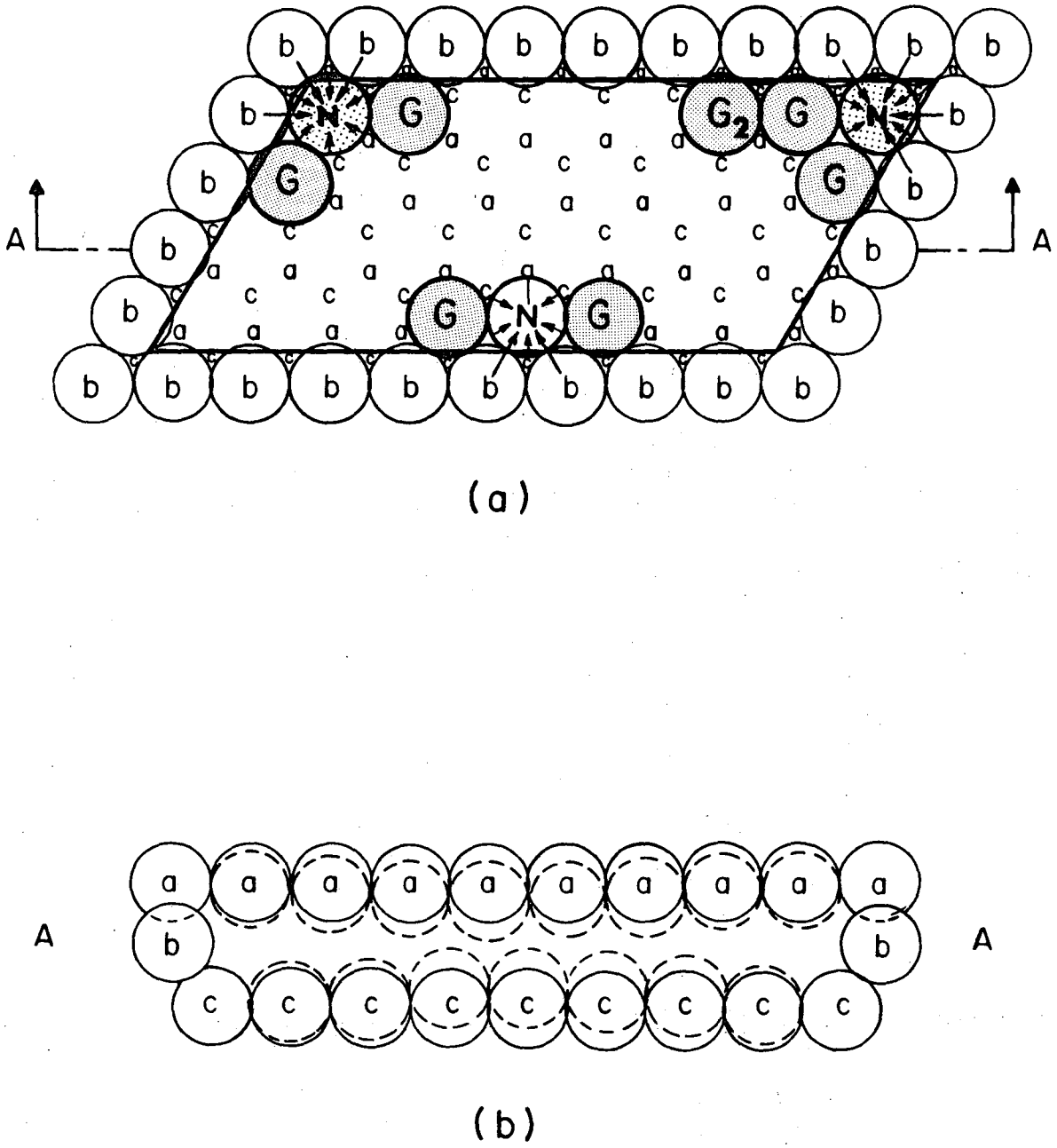

XBL678-5174

Fig. 27 (a) Arrangement of atoms around a 60° and 120 °corner
(b) Relaxation of the atoms in a disc of vacancies to form a stacking fault loop

is accompoished when the site in question is filled by one of its nearest neighbors. By determining the coordination changes which accompany the filling of each of the different nucleation sites one can determine the following expressions for the nucleation of the 60° and 120° corners:

$$k_{N60} = 10\ \nu e^{-(1.4B+E_m)/kT}$$

$$k_{N120} = 9\ \nu e^{-(2.1B+E_m)/kT}$$

where ν = Debye frequency

B = bonding energy

E_m = energy barrier for motion of a vacancy

In the same way, Table II, one can determine the rate expressions for the growth or continued motion of each jog.

$$k_{G60} = 9\ \nu e^{-(2.1B+E_m)/kT}$$

$$k_{G120} = 9\ \nu e^{-(2.1B+E_m)/kT}$$

One can see from these expressions that

$$k_{N60} > k_{N120}$$

and that

$$k_{N120} \cong k_{G120}$$

and

$$k_{N60} > k_{G60}\ .$$

Table II. Coordination changes during nucleation and growth of jogs in a ⟨111⟩-type stacking fault loop.

Process	Total Neighbors	initial coordination of neighbors			final coordination	Average
		Layer A	Layer B	Layer C		
Nucleation 120° corner	9	$\frac{11}{12}$ $\frac{10}{12}$ $\frac{9}{12}$	$\frac{11}{12}$ $\frac{10}{12}$ $\frac{10}{12}$	$\frac{11}{12}$ $\frac{10}{12}$ $\frac{9}{12}$	$\frac{8}{12}$	$\frac{10.1}{12}$
Growth 120° corner	9	$\frac{11}{12}$ $\frac{10}{12}$ $\frac{9}{12}$	$\frac{11}{12}$ $\frac{10}{12}$ $\frac{9}{12}$	$\frac{11}{12}$ $\frac{10}{12}$ $\frac{10}{12}$	$\frac{8}{12}$	$\frac{10.1}{12}$
Nucleation 60° corner	10	$\frac{11}{12}$ $\frac{11}{12}$ $\frac{9}{12}$	$\frac{11}{12}$ $\frac{11}{12}$ $\frac{10}{12}$ $\frac{10}{12}$	$\frac{11}{12}$ $\frac{10}{12}$ $\frac{10}{12}$	$\frac{9}{12}$	$\frac{10.4}{12}$
Growth 60° corner	9	$\frac{11}{12}$ $\frac{10}{12}$ $\frac{9}{12}$	$\frac{11}{12}$ $\frac{10}{12}$ $\frac{10}{12}$	$\frac{11}{12}$ $\frac{10}{12}$ $\frac{9}{12}$	$\frac{8}{12}$	$\frac{10.1}{12}$

That is, the rate of shrinkage from a 60° corner should be greater than from an 120° corner and the rate of jog nucleation is greater than or equal to the rate at which jogs move. These relationships should hold for the case of aluminum where the loop is most likely only slightly extended if at all. In gold, however, the stacking fault loop is more likely extended and the above relations cannot be expected to hold.

The nucleation and motion of jogs must instead be pictured as in Fig. 28. As is shown, the 60° corner in an extended loop presents a more stable configuration than that of a 120° corner and will offer greater resistance to the formation of a jog.

In the case of a 120° corner the activation energy for nucleation includes a work term for increasing the separation distance of the two Shockley partials. In the case of the 60° corner further energy must be expended in the reaction

$$\alpha\gamma \rightarrow \alpha B + B\gamma$$

which forms two Shockley partials from the $\frac{1}{6}\langle 110\rangle$ type stair rod. Qualitatively, we can see that the nucleation of jogs from 60° corners is much more difficult than from 120° corners. This is in agreement with the experimental results of the preceding paragraphs.

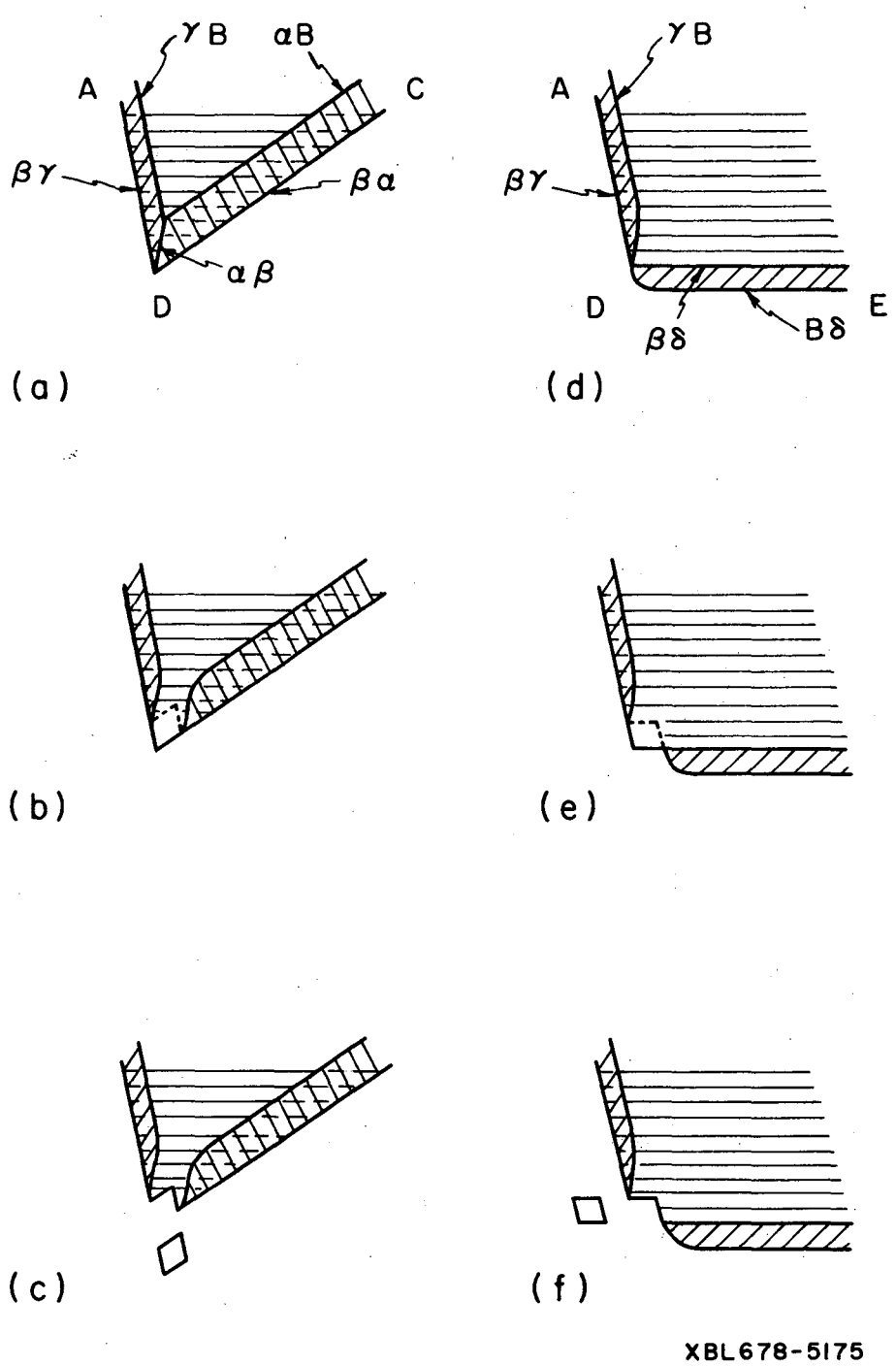

Fig. 28 Nucleation of jogs in extended 60° and 120° corners

C. Stacking Fault Tetrahedra Annealing Kinetics

The kinetics of the annealing process in terms of dislocation reactions can be analyzed in a manner similar to that widely used in chemical kinetic studies with minor modifications. The analysis generally begins with a statement of the macroscopic reaction to be considered in the form of an equation. In the present case the macroscopic, or more commonly, laboratory reaction can be represented by the expression

$$SFT \rightarrow nV$$

where SFT = stacking fault tetrahedra

nV = vacancies

The usual procedure is next to list the various mechanisms which have a role in explaining the kinetic aspects of the reaction. They should be thought of as elementary steps proposed so as to adequately explain the experimental results. Each step occurs at a rate proportional to the concentration of the particular molecular configurations to be considered. The constant of proportionality or rate constant, k, is a function of a pre-exponential term A, an activation energy E, and temperature, T.

$$k_x + Ae^{-E^*/kT}$$

E in the above expression can be thought of as the energy fluctuation needed to overcome the energy barrier of the reaction while A is usually thought in terms of the number of attempts in overcoming the energy barrier per unit time.

The above laboratory reaction has the following elementary steps

$$SFT \underset{k_2}{\overset{k_1}{\rightleftharpoons}} SFL_{60}$$

$$SFL_{60} \underset{k_4}{\overset{k_3}{\rightleftharpoons}} SFL_{120} + V$$

$$SFL_{120} \overset{k_5}{\rightarrow} SFL'_{120} + V$$

The above elementary reactions and the dislocation configurations which take part in them are postulated from the electron microscope evidence as discussed in the preceding sections.

The process of deriving the overall rate expression from the proposed mechanisms can now be carried out. In the present case, the rate expression involves the products SFL_{60} and SFL_{120} which do not occur in the balanced equation and which is present at very low levels in the system. For intermediates of this sort the standard procedure for solving the problem is to assume steady state conditions for the two intermediates. This assumption is that the net rate of formation or decay of the intermediates is negligibly small compared to each of the gross rates of formation and destruction. The nature of this assumption is examined in detail by Johnston (1963).

Assuming steady state conditons for the intermediate products SFL_{60} and SFL_{120} the following relations can be derived,

$$R = \frac{-d[SFT]}{dt} = k_1 [SFT] - k_2 [SFL_{60}]$$

$$\frac{d[SFL_{60}]}{dt} = k_1 [SFT] - k_2 [SFL_{60}] - k_3 [SFL_{60}] + k_4 [SFL_{120}] [V] = 0$$

$$\frac{d[SFL_{120}]}{dt} = k_3 [SFL_{60}] - k_4 [SFL_{120}] [V] - k_5 [SFL_{120}] = 0$$

$$[SFL_{120}] = \frac{k_3 [SFL_{60}]}{k_4 [V] + k_5}$$

$$[SFL_{60}] = \frac{k_1 [SFT]}{k_2 + k_3 - \left\{\frac{k_4 k_3 [V]}{k_4 [V] + k_5}\right\}}$$

The general expression for the reaction rate has the form,

$$\frac{-d[SFT]}{dt} = R = \left\{\frac{k_1 k_3 k_5}{k_2 k_4 [V] + k_2 k_5 + k_3 k_5}\right\} [SFT]$$

But since k_2 and k_4 are very small, the rate expression reduces to

$$R \cong \frac{k_1 k_3}{k_2 + k_3} [SFT]$$

and again if experimental conditions are such that

$$k_2 << k_3$$

The rate expression simplifies down to

$$R \cong k_1 [SFT] = \frac{-d [SFT]}{dt}$$

$$\frac{d [SFT]}{[SFT]} = -k_1 dt$$

$$\text{In } [SFT] = -k_1 t$$

It can be seen from the above equation that the slope of the logarithm of the concentration of stacking fault tetrahedra versus annealing time should give us k_1, the rate constant for the collapse of stacking fault tetrahedra to the triangular stacking fault loop. If the annealing is carried out for several temperatures, an Arrhenius plot of the data gives us a value for the activation energy and pre-exponential factor for the collapse process.

Meshii and Kaufmann (1960) have made such macroscopic measurements using electrical resistivity and changes in yield stress to measure the needed concentration changes of the stacking fault tetrahedra. They found the resoftening process to occur with an activation energy of $E^* = 4.7$ eV. The above calculations show that this activation energy should represent the barrier energy for stacking fault tetrahedra

collapse to extended Frank loops. However, the calculations of Jøssang and Hirth (1966) show this barrier energy should be on the order of 30 eV or a factor of 10 greater.

As we have seen in an earlier section neither the effect of impurities or stress alone can explain this discrepency. Perhaps both effects combined together with a more realistic model for collapse can bring calculated and observed values closer together.

IV. CONCLUSIONS

A study of the annealing of stacking fault tetrahedra in thin foils of gold by transmission electron microscopy has shown:

a) Stacking fault tetrahedra in the size range 100Å-2000Å collapsed to triangular stacking fault loops.

b) In the same temperature range 150°C to 400°C no shrinkage of stacking fault tetrahedra as tetrahedra was observed. All tetrahedra that evenutally disappeared, annealed through the collapse process.

c) The collapse of stacking fault tetrahedra appeared to be size dependent. The larger tetrahedra were observed to collapse at the lower temperatures and shorter times while the smaller tetrahedra required higher temperatures and/or longer annealing times.

d) An exception to observation (c) was the behavior of tetrahedra cut by the foil surface. For the same edge length, truncated tetrahedra appeared to be more stable than the complete tetrahedra.

Tetrahedron collapse can be accomplished by the 1) nucleation of a Shockley partial in one of the tetrahedron faces 2) formation of two Shockleys at the edge or 3) formation of three Shockley partials at the corner. The high stability of truncated tetrahedra suggests that corners and/or edges are important in the collapse process.

After collapse of the stacking fault tetrahedra annealing continues by shrinkage of the stacking fault loops. Observations by transmission electron microscopy show that:

e) Stacking fault loops in gold remain angular during shrinkage maintaining sides accurately parallel to the ⟨110⟩ directions.

f) The shrinkage rate of the loop is independent of its size as long as the loop remains angular. Rounding and dependence on loop size must occur however when a size is reached where the line tension provides the primary driving force for climb.

g) The rate of shrinkage of loops whose sides are bounded by 60° corners is much less than from sides bounded by 120° corners.

h) The surface does not appear to effect the rate of shrinkage loops. Sides formed by intersection with the surface are very stable.

i) Stacking fault loops in gold with sides bounded by stable 120° corners shrink with an activation energy of 1.9 eV and pre-exponential frequency factor of 2×10^{16} Å/hr.

From the above observations and from electron diffraction contrast evidence, it was concluded that stacking fault loops in gold are extended and that the above activation energy represents the barrier energy for jog nucleation from hexagonal corners. Furthermore, it is concluded that the annealing of stacking fault tetrahedra occurs by the consecutive steps: stacking fault tetrahedra → stacking fault triangles → stacking fault loops with 120° corners → vacancies. A steady state kinetic analysis of the process shows that the activation energy for annealing measured from bulk specimens essentially equals the barrier energy for the tetrahedron collapse step.

APPENDIX

Formation of a Stacking Fault Tetrahedron by Cross Slip

A stacking fault tetrahedron can be formed by cross slip of an extended super jog in the following way:

1. The two segments of the dislocation AC are connected by the super jog BD. The super jog is extended to form a stain rod $\gamma\alpha$ and Shockley partials αc and $A\gamma$ (Fig. A1-a).

$$AC = A\gamma + \gamma\alpha + \gamma C$$

2. The upper segment of the dislocation AC cross slips in plane ADC while the lower segment glides in plane ABC. The two segments join to form a perfect prismatic loop. (Fig. A1-b).

3. This loop can dissociate into a stacking fault tetrahedron (Fig. A1-c) or a extended Frank loop (Fig. A1-d).

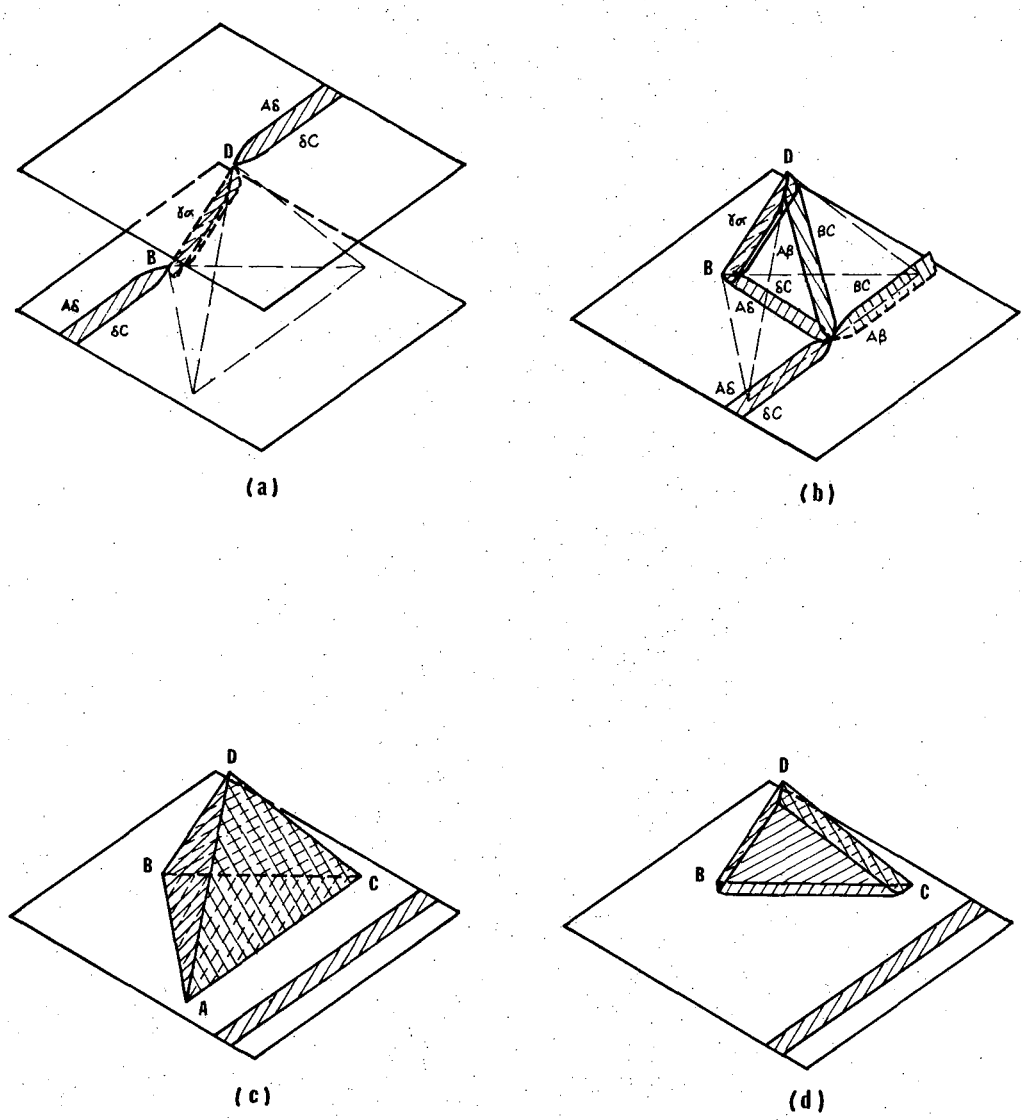

XBL 686-1119

Fig A-1 The sequence of dislocation reactions which occur during cross slip of a super jog to form (b) perfect prismatic loop (c) tetrahedron (d) Frank sissile loop.

REFERENCES

1. R. M. J. Cotterill, Phil. Mag. 6 1351, (1961).
2. M. de Jong and J. S. Koehler, Phys. Rev. 129 49, (1963).
3. P. S. Dobson, P. J. Goodhew and R. E. Smallman, Phil. Mag. 16 9, (1967).
4. P. B. Hirsch, J. Silcox, R. E. Smallman and K. H. Westmacott, Phil. Mag. 3 897, (1958).
5. P. B. Hirsch, Phil. Mag. 7 67, (1962).
6. P. Humble, R. L. Segall, and A. K. Head, Phil. Mag. 15 281, (1967).
7. H. S. Johnston, Notes on Gas Phase Reaction Rate Theory - University of California, Berkeley (1963) to be published.
8. T. Jossang and J. P. Hirth, Phil. Mag. 13 657, (1966).
9. H. Kimura, D. Kuhlmann-Wilsdorf and R. Maddin, Appl. Phys. Let. 3 4, (1963).
10. D. Kuhlmann-Wilsdorf, Acta Met. 13 257, (1965).
11. M. Meshii and J. W. Kauffman, Acta. Met. 7 180, (1959).
12. M. Meshii and J. W. Kauffman, Phil. Mag. 5 687, (1960).
13. M. Meshii and J. W. Kauffman, Phil. Mag. 5 939, (1960).
14. J. Silcox and P. B. Hirsch, Phil. Mag. 4 72, (1959).
15. J. P. Tartour, Master's Thesis (1966) UCRL No. 16907.
16. M. J. Yokota and J. Washburn, Phil. Mag. 16 459, (1967).

RECOMMENDATIONS FOR FUTURE RESEARCH

A) A number of parameters could not be controlled and varied systematically using the electron microscope technique employed for observations of dislocation-stacking fault tetrahedra interactions as described earlier. These parameters however can be studied by

1) stress-strain tests and
2) creep tests

on single crystal wire specimens.

Among the parameters that can be investigated are

1) temperature
2) strain rate
3) stress
4) concentration and size of stacking fault tetrahedra
5) density of dislocations

As was shown in Fig. 1, Part I, the concentration and size of stacking fault tetrahedra can be varied by alterations in the quenching and aging treatments. The density of moving dislocations can be varied somewhat by prestraining the specimen by different amounts before the quenching and aging treatments.

B) The tetrahedron collapsed process has been calculated by Jøssang and Hirth (1966) to occur with an activation energy on the order of 30 eV. The transmission electron microscope observations of the present study suggest that collapse occurs much more easily. This view is supported by previous annealing studies on bulk specimens where the measured activation energy was on the order of 5 eV. A number of causes may be responsible for this discrepancy. Three sources of particular importance are

1) impurities effects

2) internal stress concentrations effects

and 3) the approximations made in the calculations of Jøssang and Hirth.

The effect of impurities could be studied if the annealing process could be measured in specimens where controlled amounts of impurities such as Cu, Ag were added. The effect of stress on the collapse process can be studied through bulk annealing studies (e.g. by electrical resistivity) where an uniaxial stress can be applied to the specimen during annealing. In the above cases, extrapolation of the results to zero impurity content and zero stress should make possible the determination of the activation energy for tetrahedron collapse in the absence of these extraneous effects.

Of extreme importance in the elastic calculations of the self energy of stacking fault tetrahedra is the value given the core radius and energy of the Shockley partial and stair rod dislocations. The core radius of stair rod dislocations could be determined in specimens containing stacking fault tetrahedra by field ion microscopy. Gold whiskers containing a central screw dislocation could be used as a FIM specimen to examine the core of the perfect or extended screw dislocation.

C) The annealing behavior of stacking fault loops in gold differs from that observed for loops in aluminum in several ways. The stacking fault energy is thought to be responsible in large part for these differences e.g., $\gamma_{Au} = 40\pm10$ ergs/cm^2 $\gamma_{Al} = 150\pm30$ ergs/cm^2. A study of the influence of the stacking fault energy on the annealing behavior of loops can be made in a system such as nickel-cobalt where the addition of

40 at.% Co reduces the stacking fault energy of Ni by over 200 ergs/cm^2. By varying the solute content, a series of alloys can be prepared which differ primarily in its stacking fault energy. Stacking fault loops formed in these alloys by quenching and aging can then be used to study the effect of stacking fault energy on the climb behavior of these loops.

ACKNOWLEDGMENTS

The author is deeply grateful to Professor Jack Washburn for his encouragement and advice throughout this investigation. Thanks are due also to Professors J. E. Dorn and H. S. Johnston for their helpful discussions of the work.

This work was carried out under the auspices of the United States Atomic Energy Commission through the Inorganic Materials Research Division of the Lawrence Radiation Laboratory.

This report was prepared as an account of Government sponsored work. Neither the United States, nor the Commission, nor any person acting on behalf of the Commission:

A. Makes any warranty or representation, expressed or implied, with respect to the accuracy, completeness, or usefulness of the information contained in this report, or that the use of any information, apparatus, method, or process disclosed in this report may not infringe privately owned rights; or

B. Assumes any liabilities with respect to the use of, or for damages resulting from the use of any information, apparatus, method, or process disclosed in this report.

As used in the above, "person acting on behalf of the Commission" includes any employee or contractor of the Commission, or employee of such contractor, to the extent that such employee or contractor of the Commission, or employee of such contractor prepares, disseminates, or provides access to, any information pursuant to his employment or contract with the Commission, or his employment with such contractor.